WINDOWING EFFECTS AND ADAPTIVE CHANGE POINT DETECTION OF DYNAMIC FUNCTIONAL CONNECTIVITY IN THE BRAIN

A Thesis
Presented to
The Academic Faculty

by

Sadia Shakil

In Partial Fulfillment
of the Requirements for the Degree
Doctor of Philosophy in the
School of Electrical and Computer Engineering

Georgia Institute of Technology
May 2016

WINDOWING EFFECTS AND ADAPTIVE CHANGE POINT DETECTION OF DYNAMIC FUNCTIONAL CONNECTIVITY IN THE BRAIN

Approved by:

Professor Chin-Hui Lee, Advisor
School of Electrical and Computer Engineering
Georgia Institute of Technology

Professor Xiaoping Hu
School of Biomedical Engineering
Georgia Institute of Technology and Emory University School of Medicine

Associate Professor Shella Keilholz, Co-advisor
School of Biomedical Engineering
Georgia Institute of Technology and Emory University School of Medicine

Professor Ghassan AlRegib
School of Electrical and Computer Engineering
Georgia Institute of Technology

Professor Mark Clements
School of Electrical and Computer Engineering
Georgia Institute of Technology

Assistant Professor Omar T Inan
School of Electrical and Computer Engineering
Georgia Institute of Technology

Date Approved: 29 March 2016

Dedicated to my parents , Shakil Ahmad and Shahida Shakil, whose unconditional love and prayers led to every success in my life.

ACKNOWLEDGEMENTS

During my almost five and a half years of Ph.D., I was inspired and positively influenced by so many people that it is impossible for me to thank all of them individually. However, I would like to express my gratitude to some of them.

First of all I would like to thank my advisor, Dr. Chin-Hui Lee, and co-advisor, Dr. Shella Keilholz. They were the best advisors I could ever wish for. With their diversified backgrounds and different methods of advisement, they enriched my expertise in various fields that helped me complete my research successfully. They were my mentors throughout this time and helped me with more than just research.

I would also like to convey my gratitude to my dissertation committee members: Dr. Mark Clements, Dr. Xiaoping Hu, Dr. Ghassan AlRegib, and Dr. Omer Inan for being so cooperative and helpful. Their advice after the dissertation proposal provided me with valuable ideas for the completion of the remaining work. The courses I took with Dr. Clements and Dr. AlRegib aided me a lot in formulation of my research. I would also like to thank Dr. Mark Davenport, Dr. Justin Romberg, and Dr. Biing-Hwang Juang for permitting me to attend their classes. I believe their courses aided me in shaping the ideas for my research.

Next, I would like to thank my lab members both at Georgia Tech and Emory. I was lucky to have two labs filled with awesome people. I would like to especially mention here a few names: Ilseo Kim, Aleem Mushtaq, You-Chi Chang, IFan Chen, Garth Thompson, Jashua Grooms, Jacob Billings, Wen-Ju Pan, Waqas Majeed, Maysam Nezafati, and Anzar Abbas. These are the people I bothered the most with my questions and other issues, and they were always there to assist me.

I had been very lucky in finding good friends during my Ph.D. I would specially

like to thank Bushra, Sarwat, Unazia, Sana, Ruma, Temi, and Bhuvana for always being there for me. My roommates were not only my dear friends but were my family away from the family. Shahana was there to guide and encourage me when I started my Ph.D. Ifrah handled my mid Ph.D. phase with its ups and downs. Marzia and Ayesha were constant support for my last years of struggle, frustrations, failures, and successes. I believe all of them share some of the best and worst moments of my Ph.D. life.

I would also like to thank Patricia Dixon and Raquel Plaskett for helping me with administrative matters at the ECE office. Steven Marzec from Emory technical department was just awesome in handling my laptop and desktop issues. Brian Diffley, from my Ph.D. funding agency, Fulbright, had been very supportive throughout my program.

Last but not least, I would like to thank my family for always being there for me. I lost my father almost a month after my arrival in USA, but I still give the credit of my success to him and my mother, more than even myself. He was a source of positivity, inspiration, and optimism for me throughout my life. My Ph.D. was more of his dream than mine. He was always there to encourage me for goals that seemed even beyond my dreams to me. My mother is a constant source of strength with her encouragement to work harder for my goals. My siblings, Jasia, Adnan, Kiran, and Hassaan were there for me despite the distance of thousands of miles separating us. They believed in me more than I believed in myself. In addition to them, their kids were a source of joy to me and my sister-in-law Marium was there whenever I needed her. The continuous support, encouragement, and love from my family were major contributions to the successful completion of my Ph.D.

TABLE OF CONTENTS

LIST OF TABLES

LIST OF FIGURES

SUMMARY

Evidence of networks in the resting-brain reflecting the spontaneous brain activity is perhaps the most significant discovery to understand intrinsic brain functionality. Moreover, subsequent detection of dynamics in these networks can be milestone in differentiating the normal and disordered brain functions. However, capturing the correct dynamics is a challenging task since no 'ground truths' are present for comparison of the results. The change points of these networks can be different for different subjects even during normal brain functions. Even for the same subject and session, dynamics can be different at the start and end of the session based on the fatigue level of the subject scanned.

Despite the absence of ground truths, studies have analyzed these dynamics using the existing methods and some of them have developed new algorithms too. One of the most commonly used method for this purpose is sliding window correlation. However, the result of the sliding window correlation is dependent on many parameters and without the ground truth there is no way of validating the results. In addition, most of the new algorithms are complicated, computationally expensive, and/or focus on just one aspect on these dynamics.

This study applies the algorithms and concepts from signal processing, image processing, video processing, information theory, and machine learning to analyze the results of the sliding window correlation and develops a novel algorithm to detect change points of these networks adaptively. The findings in this study are divided into three parts: 1) Analyzing the extent of variability in well-defined networks of rodents and humans with sliding window correlation applying concepts from information theory and machine learning domains. 2) Analyzing the performance of sliding window

correlation using simulated networks as ground truths for best parameters selection, and exploring its dependence on multiple frequency components of the correlating signals by processing the signals in time and Fourier domains. 3) Development of a novel algorithm based on image similarity measures from image and video processing that may be employed to identify change points of these networks adaptively.

The findings of this study are beneficial to the field of neuro dynamics from various aspects. They provide a new application of Kullback-Leibler divergence from information theory domain to find specific regions with variable states of functional connectivity. The results of this study also provide a novel application of t-Distributed Stochastic Neighbor Embedding, from machine learning domain, to visualize the high dimensional results of the sliding window correlation in low dimension. One major contribution of this study is the detailed analysis of the sliding window correlation itself using simulated networks and exploring its frequency dependencies. Two detailed studies in this direction provide major guidelines for future studies to move the focus from sliding window correlation results to raw resting-state networks. This point is further enhanced by the development of a novel change point detection algorithm that utilizes the raw resting-state data. This algorithm demonstrates the need to inspect scanned images visually and relate the concepts from image and video processing to capture their dynamics. In short, the results presented in this study use ideas from various domains for the processing of neural signals. The application of algorithms and ideas from these domains is a significant enrichment to the field of neuro dynamics.

CHAPTER I

INTRODUCTION

Understanding the human brain's intrinsic functionality has been one of the major targets of studies in neuro science and engineering. Rapid increase in the number of neurological disorders has made this comprehension an urgent issue. It is believed that the comprehension of brain's basic functionality would help in identification of the neurological disorders and their early cure. One of the most commonly used method to scan brain functions is 'functional magnetic resonance imaging (fMRI)'. fMRI is a non-invasive technique of brain scan. In early studies using fMRI, the subjects were asked to perform some tasks during the scan session. Afterwards, the interactions between various regions of the brain, forming functional networks, were studied. However, patients with neurological disorders are not expected to follow task instructions, which made scanning their brain a challenging issue. Recent discovery of functional networks in the resting brain (when is subject is not performing any explicit task and is just thinking), similar to the task-based networks, is a landmark for the study of brain functions since it does not require the subject to perform any explicit task. As a result, it is possible to scan patients with neurological disorders who cannot follow any explicit task instructions. These networks called 'functional connectivity (FC)' networks change configurations or 'states' within few seconds, and the changes in a normal brain are different from a brain with some neurological disorders. So the key to understanding the intrinsic brain functionality may be in comprehension of these dynamics. However, understanding these dynamics is a big challenge since there are no 'ground truths (GT)' for timings of these changes, even in normal brain functions. Even for a normal brain the change points of these networks depend on

age, sex, and vigilance levels of the subjects scanned. Despite this lack of GT, studies have used existing methods of capturing the changes in FC networks and a few have developed new methods for this purpose. One of the most widely used method for capturing these dynamics is 'sliding window correlation (SWC)'. However, the results of the SWC are dependent on many parameters, and different studies use different sets of parameters. In the absence of GT there is no way of validating these results. Furthermore, the new algorithms to capture these dynamics are very few, and they are computationally extensive and/or focus on one specific aspect of these dynamics.

The main purpose of this study is to evaluate the performance of the SWC as a suitable dynamic analysis method and to develop a simple algorithm for change point detection of FC networks adaptively from raw rsfMRI scans. For performance evaluation of the SWC, we formulated simulated networks (SNs) from real resting-brain data and used these SNs as GTs. As for adaptive change point detection we utilized the fact that the change in the FC networks is associated with changes is the visual aspects of the rsfMRI scans.

This study applies the algorithms and concepts from signal processing, image processing, video processing, information theory, and machine learning to analyze the results of the sliding window correlation and develops a novel algorithm to detect change points of these networks adaptively. The findings in this study are divided into three parts: 1) Analyzing the extent of variability in well-defined networks of rodents and humans with sliding window correlation applying concepts from information theory and machine learning domains. 2) Analyzing the performance of sliding window correlation using simulated networks as ground truths for best parameters selection, and exploring its dependence on multiple frequency components of the correlating signals by processing the signals in time and Fourier domains. 3) Development of a novel algorithm based on image similarity measures from image and video processing that may be employed to identify change points of these networks adaptively.

In this chapter first the SWC and its limitations would be presented, followed by the state-of-the-art dynamic FC analysis methods. Afterwards, major contributions of this study would be presented. And finally the thesis organization would be given.

1.1 Sliding Window Correlation

In digital signal processing, sliding window is extensively used for short term analysis in which a signal of interest is analyzed after dividing it in overlapping windowed segments. The choice of window length influences the properties of the outcomes. In SWC, the analysis is extended by exploring the relationship of two signals of interest with computation of their correlation coefficient for a certain window length, then the computation is repeated after shifting (sliding) the window by some amount and the process is repeated till the end of correlating signals. This process results in series of correlation coefficients varying as a function of the window length and the shift. The smallest window size is governed by the smallest frequency component of the correlating signals [53] but the selection of best window size is challenging. Similarly, the choice of window shift is also dependent on the desired results with smaller window shifts capturing more transients at the expense of the computational cost. The SWC is the most commonly used method of dynamic study in many fields such as finance, medical, network analysis, and weather trends etc., yet it has many pitfalls that can complicate the interpretation of the end results.

1.1.1 Sliding Window Correlation for Dynamic Functional Connectivity

For dynamic FC (dFC) also, the sliding window correlation (SWC) is the most widely used method of capturing changes. It computes specific region-based dynamics in a seed-based (seeds are specific regions of the brain picked on the basis of their contribution to one or more FC networks) analysis [36, 42, 103] or network-based dynamics by correlating the time series associated with the independent components of FC networks [2, 43, 87]. The issue becomes more complicated when the goal is

to find the change point of network consisting of more than two signals changing relationship at unknown random points, as is the case with dFC networks. For such networks one window length may not be optimum for capturing the dynamics and it may need to be adaptive, but this adaptive selection is possible only if the network change points can be identified.

1.1.2 Limitations of Sliding Window Correlation Analysis

In dFC studies, the SWC is used to compute pairwise correlation of all regions comprising a network using different window sizes [42, 32, 103, 37]. The range of window lengths used in various studies range from 8 to 240 seconds [14, 43, 42, 2, 45, 103], and the shift ranges from one repetition time (TR) or sample rate to 50% of the window length [15, 42, 45]. Most of the studies report large variability in the results for smaller windows and vice versa. As a result, smaller windows are thought to capture short-lived variations of the dynamics. However, studies have shown that for short windows some of these variations may be due to spurious fluctuations arising as a result of the method itself [53, 33], rather than short-lived dynamics of FC. Some of the variabilities captured in any window may be due to the presence of just one amplitude change, acting as an outlier [83, 55]. After computation of SWC, most of the studies report the state transitions based on just one window [2, 43]. The number of states identified is again depend upon the amount of variability captured in the results, based on window size and other parameters. The absence of GTs make it extremely difficult to validate the results of these analysis, and there is no way of knowing if the variabilities detected in the results are due to dynamics of the network or limitations of the method itself.

1.2 State-of-the-art Dynamic Analysis Methods

Some of the recent studies reported the observation of dFC from the raw rsfMRI data [62, 61, 57, 56, 72]. In [62, 61], the presence of quasi-periodic patterns (QPPs) is

reported. The QPPs were first discovered in rats by observing the change in resting-state networks with naked eyes [62]. Afterwards, they were observed in humans and an algorithm was developed to extract them [61]. In QPPs the transition between networks takes places within a span of few seconds. Co-activation patterns were reported in [57, 56]. Co-activation patterns [57, 56] approach states that the spontaneous activity in the brain maybe dominated by brief instances of activations and deactivations. The co-activation patterns in [57] were identified by averaging a few frames around the point of co-activation. Similar observation is made for spontaneous blood-oxygen-level-dependent (BOLD) events [72]. These studies present new algorithms based on transitions and/or spontaneous activations observed in raw rsfMRI scans. However, the methods developed in them are focused on extracting their discoveries only (QPPs in [61] and co-activation patterns in [57]). Some other studies [19, 55, 83, 38] also introduced new methods of dFC analysis but none of them focus on the extraction of just the change points from the dFC networks, regardless of its source (e.g. QPPs or co-activation patterns).

1.3 Major Contributions of the Study

Based on the extensive use of the SWC as a prevalent dynamic analysis method, there was a need to evaluate its performance to explore if any combination of its parameters may provide an optimum way to capture dynamics of randomly changing functional connectivity (FC) networks in the absence of any GTs. There was also a need for an algorithm to detect the network change points adaptively. After detection of these points, adaptive windows of appropriate lengths can be used between any two such points to successfully capture the dynamics of FC networks. This study focused on these two major aspects of the dFC analysis. According to the author's knowledge, it is the first time well-characterized evaluation of the SWC is performed, and an algorithm is developed that may identify the change points of the dFC adaptively.

This major contributions of this study are given below:

1. Variable extent of the functional connectivity (FC) networks in rodents and humans is explored in Chapter 3.

2. Performance of the sliding window correlation (SWC) is evaluated by forming SNs from real resting-state data in Chapter 4.

3. Frequency dependencies of the window in the sliding window correlation (SWC) is studied by analyzing the influence of multiple frequencies in correlating signals in Chapter 5.

4. A novel adaptive change point algorithm is presented in Chapter 6.

The first part of the Chapter 3 (published in [81]) explored the spatial variability in the FC of well-known networks in rodents. In this part we introduced a novel application of Kullback-Leibler (KL) divergence, form information theory, to identify the regions with discrete states of FC. Identification of these regions in any network would reduce the computations of subsequent dynamic analysis and the computational cost associated with whole brain dFC analysis. In the second portion of this chapter we applied well-known dimensionality reduction technique, t-Distributed Stochastic Neighbor Embedding (t-SNE), from machine learning domain, for visualization of high dimensional SWC results in low dimension. We used four different windows to compute the SWC of all node pairs in resting-state networks. Low dimensional visualization of the results provided a novel way to capture and compare the state variability from small to large windows. The study in this chapter identified the fact that the extent of variability captured by the SWC is dependent on the size of the window emphasizing the need to evaluate the performance of the method itself. This led us to the next part of our study presented in Chapters 4 and 5.

In the second part of the study (Chapters 4 and 5), we evaluated the performance of the SWC from two angles. In Chapter 4 (published in [80]), we formed SNs from

real resting-state data to investigate the presence of best combination of different window parameters. We had control over the state change points of these SNs so we used them as the GTs for our analysis. In Chapter 5 (published in [79], extended invited version submitted to special issue of IEEE BIBM 2015 BMC Systems Biology), we explored the influence of frequency components on window lengths by analyzing the correlating signals in time and Fourier domains. The analysis used in this part of the study used data from FC networks (for formation of SNs) or simple sinusoids (for frequency based analysis), but these results would befnefit any other field of study that utilizes the SWC.

Last part of our study in Chapter 6 focused on development of an algorithm for adaptive change point detection in the dFC networks. We believe that once these change points are identified dynamic relationship between various regions can be computed in between them by using sliding window of variable lengths or any other appropriate method. Our algorithm is based on the concepts of stochastic sign change (SSC) and sum of absolute difference (SAD) similarity measures used in image and video processing algorithms respectively. This algorithm is simple and computationally very inexpensive with a computational complexity of O(n), where n is the number of nodes in a network. This algorithm was able to identify some probable points of changes in resting-state networks. However, in the absence of any ground truth it is not easy to identify if these changes were due to network changes or were false positives. In future, some statistical measures may be developed to test for the significance of these changes. The algorithm can also be tested on groups of healthy controls and patients to explore if it can differentiate between change points detected in them.

1.4 Thesis Organization

The rest of the thesis is organized as follows: In Chapter 2, background for the need of this study is discussed. In Chapter 3, variability of the dFC is explored in well-characterized FC networks of rodents and humans. In Chapter 4, we evaluated the performance of the SWC by forming SNs from real resting-state data as GTs. In Chapter 5, we explored the relationship between the frequency components and the window length of the SWC in time and frequency. In Chapter 6, new algorithm for adaptive change point detection of the dFC is presented. Chapter 7 contains all findings, limitations of the study and future work. Chapter 8 (Appendix A) contains the detailed mathematical derivations of the results presented in Chapter 6.

CHAPTER II

BACKGROUND

The functional connectivity (FC) in the resting brain results in resting-state networks (RSNs) that are dynamic and change configurations randomly based on many parameters. The FC dynamics of these RSNs have a neural basis in humans as well as in animals and are linked with neurological disorders. The comprehension of these dynamics is important but challenging in the absence of ground truths (GTs) for the comparison of results. In this study we focus on exploring the selection of best parameters for the most popular dynamic functional connectivity (dFC) analysis method of the sliding window correlation (SWC) and develop a new method for adaptive detection of change points in dFC networks. In this section we will briefly review the previous research efforts relevant to these topics: Functional connectivity (FC) networks, dynamic FC (dFC), and analysis techniques for dFC.

2.1 Functional Connectivity (FC) Networks

In the rsfMRI the activity of any brain region is measured by changes in its blood oxygen level using blood-oxygen-level-dependent (BOLD) contrast [67]. The resultant spontaneous low-frequency fluctuations (LFFs) in BOLD signal reflect neural synchronicity between brain regions [8]. Two or more such regions are functionally connected if they have highly correlated activity [6] forming FC networks or RSNs that are present in humans [21, 27] and animals [59, 71]. The FC of these networks is considered a true measure of underlying neural activity in humans, since loss of resting inter-hemispheric FC is observed after complete section of the corpus callosum, which is a broad band of nerve fibers joining the two hemispheres of the brain [39]. Other studies also reported neural basis of these networks in humans [46] and animals

[92, 70, 68, 69, 85]. These RSNs show that the brain may be involved in continuous information processing and cognition even in relaxed state [6, 17] and are linked to normal and neurotic brain conditions [27, 26]. The RSNs in the brain with some neurological disorder are different from those functioning normally, pointing towards their clinical significance [88, 49, 11]. As a result, rsfMRI has become an important tool for the investigation of spontaneous network activity in the brain, both during normal function and in neurological disorders [6, 89, 88, 96, 11, 3, 74, 107, 104]. Studies have also identified resting-state FC networks that typically involve areas known to be anatomically connected [66, 86].

The most fundamental RSN is the default mode network (DMN) consisting of regions active at rest [73, 10], while the opposing network that is active during attention demanding tasks is termed as task positive network (TPN) [23]. These two networks are found if the resting brain of humans is divided into two clusters or RSNs, and increasing the number of clusters/RSNs splits these networks into more sub-networks [48]. Currently ten RSNs are usually reported in human studies [38] as shown in Figure 1. However, the exact number of these networks, and even the standard definition of the 'network' in this context, are still controversial. The identification of these RSNs can be done by using predefined structural regions from a common atlas or template [63], choosing one important region of interest (ROI) of a RSN and finding its significantly correlated nodes/regions in seed-based analysis [7, 17, 97], or clustering functionally connected areas using data-driven methods such as independent component analysis (ICA) [65, 12].

For a long time functional connectivity (FC) of these resting-state networks (RSNs) was considered to be stationary or static for the whole scan length and neural basis of the static FC was found in humans [46, 39] and animals [93, 70, 68, 69, 85]. However, recently the emphasis has moved to dynamic approaches that examine the evolution of network connectivity over time.

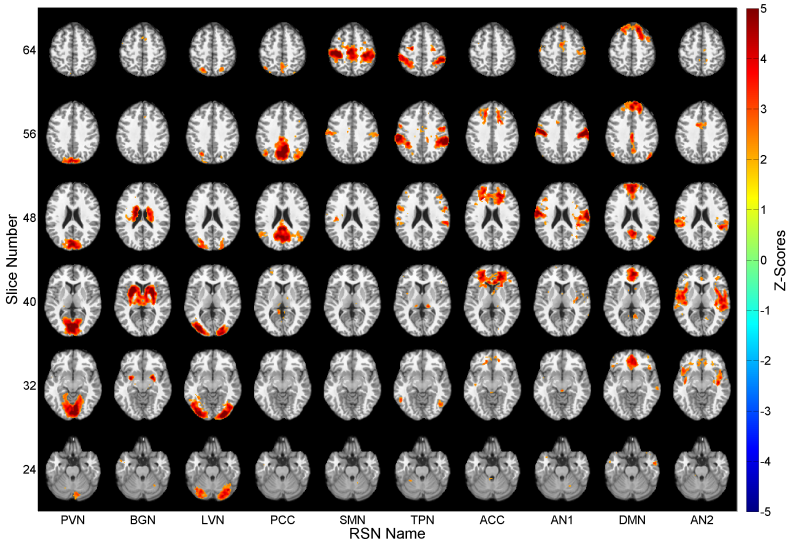

Figure 1: Functionally relevant resting-state networks (courtesy of Joshua K. Grooms). Each network is labeled by an acronym of its commonly used name: primary visual network (PVN), basal ganglia network (BGN), lateral visual network (LVN), posterior cingulate network (PCC), sensorimotor network (SMN), task positive network (TPN), anterior cingulate cortex (ACC), first auditory (AN1), default mode network (DMN), and second auditory (AN2).

2.2 Dynamic Functional Connectivity (dFC)

Several studies have reported that the connectivity dynamics of these networks reveal a number of FC states in the brain, which can be sensitive to changes related to neurological disorders [77, 20, 54, 40]. These dynamics are also linked to changes in human behavior [45, 91, 38, 76].

Recently, it has been proposed that quantifying changes in FC metrics over time may provide greater insight into fundamental properties of brain networks [36]. The FC is found to change due to many reasons, such as task demands [22], learning [1], and sleep [35]. Furthermore, along with between-subject FC variations, within-subject variations are observed in different scans even within the same imaging session [34]. As a consequence, the FC between the regions is not stationary but dynamic and varies substantially over time during a single scan in studies of humans [14, 43, 61] and animals [62, 36, 42]. Some of this variability appears to arise from properties of the signal itself rather than a true relationship with time-varying neural activity [42, 32]. However, recent work by multiple groups showed that at least part of the variability is linked to changes in neural activity [15, 90, 92, 68]. These neural bases of the dynamics are reported in animals [92] and in humans [15]. Furthermore, these dynamics are also linked to changes in human vigilance level [91] and behavior [45, 38, 76].

2.2.1 Dynamic Functional Connectivity (dFC) in Neurological Disorders

Dynamics of the functional connectivity (FC) in normal brain function are different from the ones in neurological disorders [13, 105] and understanding them is of paramount importance for early detection of the onset of neurological disorders and their timely cure. The dynamic analysis of FC can enhance the understanding of normal cognition and alterations that result from brain disorders since the dynamics of these FCs are found to be linked with the neuronal disorders [77, 20, 54, 40]. A comparison of healthy controls and schizophrenia patients showed that on average,

schizophrenia patients change the brain state less frequently than controls, so the disease may be due to patients being stuck in few states [20]. Patients with Alzheimer's disease have altered network connectivity and altered amount of time spent in different states compared to healthy controls [40].

2.2.2 Potential Drivers of Dynamic Functional Connectivity (dFC)

One way to think of spontaneous cognition of the resting brain is as a series of discrete thoughts and events that are thought to be potential drivers of FC network dynamics [41]. A recent study identified single spontaneous events that may be the cause of part of the non-stationary nature of these networks [72]. These spontaneous events encompassed regions of DMN and correlation of fluctuations peaked at the time of these events.

Another study found co-activation patterns based on high signals in a seed region [57, 56]. Some of these co-activations patterns were similar to independent networks identified by ICA [87]. These studies show that at least some of the variations in FC are driven by transient events rather than slow modulations of the vigilance [41]. These findings also suggest the possibility of recurring 'brain states' or common configurations of connectivity that recur over time [41]. Seven such brain states of FC were identified in humans [2] and three in rodents [42]. In humans the most common state was similar to the steady-state connectivity [2].

In addition to patterns of instantaneous activity which may repeat over time in sporadic fashion, evidence of quasi-periodic patterns (QPPs) is found in spontaneous BOLD fluctuations that occur more slowly [41]. The first evidence of these QPPs was reported in rodents [62] followed by their discovery in humans [61]. Similar patterns were reported in another study [29] using a different methodology and in REM sleep [16]. Neurological basis of the QPPs have also been observed [94]. In humans these patterns involved signal propagation and alternation in several areas of DMN and

TPN. This would be expected based on the time scales of cognitive processes and variations in vigilance [14, 43, 36, 42, 2, 61] that is related to the attention or alertness span of a subject.

2.3 Analysis Techniques of Dynamic Functional Connectivity (dFC)

One of the major challenges faced by the blossoming field of rsfMRI network dynamics is determining appropriate analysis algorithms and parameters. Most of the studies to identify the patterns of dFC either estimate pairwise variations of inter-regional covariances or identify changing patterns of covariance at a multivariate level [83]. We will give details of both approaches along with their limitations.

2.3.1 Estimation of Pairwise Dynamic Functional Connectivity (dFC)

The estimation of pairwise dFC variations has been applied to the study of animals [42, 92] and humans [32]. In its simplest and most popular form the pairwise computation studies select two or more ROIs from the brain based on the prior knowledge of their involvement in some FC network [42] or based on their significant stationary correlations with other ROIs [32, 37, 106]. After selecting the ROIs the corresponding time series are extracted and pairwise SWCs of all ROIs are computed using a window of an appropriate length. In the absence of any GT for the underlying FC networks, studies have used a vast range of window lengths ranging from 8 seconds to 240 seconds in humans [91, 14, 32, 15, 43] and animals [42, 37]. The whole brain FC can be estimated using pairwise approach and further analysis is done in a number of ways, such as dynamic graphical representation of the networks for the window length [40], clustering of the resulting networks [81], matrix factorization [52], and applying some data-driven method such as principal component analysis on the resulting networks [51].

2.3.2 Dynamic Functional Connectivity (dFC) Pattern Extraction (Multivariate Analysis)

Multivariate analysis extracts the FC network maps or patterns for the whole brain using various techniques and studies the dynamics of these patterns. In [2] these patterns were extracted using spatial ICA and variability of patterns was analyzed by the SWC analysis of the associated time series. In [87] these independent components were used in temporal ICA to extract temporally-independent modes of FC. In another study, the data-driven method of 'dynamic connectivity regression (DCR)' [19] was used to find the temporal change points in FC. Afterwards, the set of relationships was estimated for data that was between pairs of change points. In order to extract the spatiotemporal dynamics of QPPs in [61], a template consisting of several preprocessed images was selected and sliding correlation of this template with the image series resulted in extraction of quasi-periodic patternss (QPPs). The co-activation patterns in [57] were identified by averaging a few frames around the point of co-activation. Recently, [55] applied 'dynamic conditional correlation (DCC)' model from finance literature to estimate bivariate as well as multivariate FC. This is a two-step process: In the first step, time-varying variances of each time series are estimated and in the second step residuals are used to estimate the dynamic correlations. Another recent study [83] introduced 'multiplicative analytical coupling (MAC)' that computes the temporal difference of all network nodes from adjacent scans and computes a simple moving average of their product at every time point.

2.3.3 Limitations of Dynamic Functional Connectivity (dFC) Analysis

For pairwise analysis, SWC is the most commonly used method but its results are strongly dependent on window length [42, 77, 37] and the ideal value for window length is still unknown. In some studies the comparison of results for various window lengths was reported [42, 32, 103, 37] showing that the shorter windows capture more fluctuations but very short ones (15 seconds) may not have sufficient number

of time points for the correlation to be significant and very long window lengths may over filter some interesting frequencies [32]. However, another study reported that short-time windows (12.3 seconds) between DMN and TPN predicts vigilance task performance [91]. The issue of minimum window length was discussed in [53] and it was concluded that the minimum window length should be the reciprocal of the minimum frequency in the correlating signals for the SWC result to be very close to the actual correlation. This study provides some insight into the minimum window length but the optimal window length selection is still ambiguous [92]. The choice of window length can have significant impact on results [42, 53, 92] but no method of determining the ideal length is known yet, since there are no GTs to analyze for comparison of results.

In addition to issue of GTs for the validation of SWC results, the method itself has some limitations. [42, 103, 37] reported that the SWC results fluctuate largely between negative and positive values (especially for smaller windows) even when the actual correlations are positive. This may be the result of the SWC sensitivity to the change in single value of correlating signals [83, 55]. Spurious fluctuations in SWC results are also reported [53]. A recent study [33] showed that the mere presence of fluctuations in the SWC time series cannot be taken as the evidence of dynamic functional connectivity and that it is important to select an appropriate null hypothesis when performing the dynamic FC analysis.

There are limitations of multivariate analysis methods also. In [2], it was reported that end results were strongly dependent on the window length. The limitation of DCR in [19] is the fact that the distance between change points needs to be adjusted based on a priori knowledge of spacing of changes in the FC. In [61], the algorithm cannot be used to identify isolated events and selection of window length can influence the resulting QPPs obtained. Similarly, DCC in [55] was inefficient with very fast short term state changes and MAC in [83] the results are dependent on the window

size and wrong window size can amplify the noise. The extraction of co-activation patterns [57, 56] is computationally very expensive and may not be feasible for large data sets.

All of these studies point towards a need to evaluate SWC to get parameters for its best performance and to develop a new algorithm for adaptive change point detection in dFC networks. Our study addressed both of these aspects. It focused on analyzing the performance of the SWC and developed a new adaptive change point detection algorithm. The current research is divided into three parts. The first was to use the SWC to study the extent of dynamics in the FC of rodents and humans. The second part evaluated the performance of the SWC as an efficient method for dynamic analysis of FC networks in the absence of any GTs. The third part developed an algorithm for adaptive detection of state change points of FC networks, since SWC was found to perform poorly in detecting these points.

CHAPTER III

VARIABLE EXTENT OF FUNCTIONAL CONNECTIVITY

Previously, most studies of dynamic functional connectivity (dFC) focused on the temporal variation of connectivity between regions, but assumed spatial stationarity of the networks over time [42, 2]. Moreover, studies either reported sliding window correlation (SWC) results for number of different window sizes [42, 103, 37] or state assignment for one window [2, 52]. In this chapter, we explore the variable extent of functional connectivity (FC) in rodents and humans from two different angles.

Since a major amount of our work in this study is related to the SWC analysis so we start with a mathematical formulation of the method itself followed by our study and its results.

3.1 Sliding Window Correlation (SWC)

The mathematical formulation of the SWC would provide more insight of the process itself.

The SWC coefficient of two signals x and y at time point n is given by [53],

$$\rho_{xy}[n] = \frac{c_{xy}[n]}{\sqrt{c_{xx}[n]}\sqrt{c_{yy}[n]}}, \tag{1}$$

in which $c_{xy}[n]$ is the covariance and $\sqrt{c_{xx}[n]}$, $\sqrt{c_{yy}[n]}$ are standard deviations of the two signals. The SWC can be computed by computation of these terms over a window w. The covariance computed over the window w can be given by,

$$c_{xy}[n] = cov(x[n-\Delta, n+\Delta], (y[n-\Delta, n+\Delta]) = \ (\frac{TR}{w}) \sum_{i=n-\Delta}^{i=n+\Delta} (x_i - \overline{x}_n)(y_i - \overline{y}_n) \tag{2}$$

in which $w = (2\Delta + 1)TR$ is the odd window length in seconds, TR is the sampling rate (repetition time) of the scanned images, and $\overline{x}_n$, $\overline{y}_n$ are means of the signals x_i and y_i respectively for the window positioned at n. After evaluation of this mathematical expression, the formula becomes [53],

$$c_{xy}[n] = \underbrace{(TR/w) \sum_{i=n-\Delta}^{i=n+\Delta} x_i y_i}_{\text{I}} - \underbrace{\overline{y}_n \overline{x}_n}_{\text{II}} \tag{3}$$

$\sqrt{c_{xx}[n]}$ and $\sqrt{c_{yy}[n]}$ can also be computed by the formula in Equation (3) .

Sliding the window by m time points would result in shifting the computation of covariance (and correlation) at the point $n + m$ as given below.

$$c_{xy}[n+m] = (TR/w) \sum_{i=n+m-\Delta}^{i=n+m+\Delta} x_i y_i - \overline{y}_{n+m} \overline{x}_{n+m} \tag{4}$$

Choosing a small value of shift m would give large overlap of consecutive windows providing extensive details of relationship changes in the correlating signals and vice versa.

3.2 Spatial Variability of Functional Connectivity in Rodents

The first part of the study presented in this chapter characterize the spatial stability of networks over the course of multiple scans and identify regions that transiently join or leave well-described networks in the rat brain. This study focused on the dFC of the seed ROIs in primary somatosensory cortex (S1) and the caudate putamen (CP). Left and right somatosensory cortex are directly connected via the corpus callosum and exhibit strong connectivity [102, 71, 108]. Left and right CP are not directly connected but still exhibit strong connectivity [102, 108], possibly due to a feedback loop with the cortex. We selected these seed ROIs since earlier studies hinted at the possibility of discrete states of their FC, with S1 and CP occasionally but not always appearing to be correlated with each other [62]. Histograms of the SWC coefficients were then used

to compute KL divergence as an attempt to identify voxels that participate in multiple discrete states of connectivity. Our findings demonstrated significant variability in the spatial extent of the FC networks over time. Multi-modal histograms with high KL divergence provided evidence of discrete states of connectivity in voxels on the periphery of the network, but core voxels typically exhibited unimodal histograms. The work presented in this part is published in [81].

3.2.1 Motivation

Analysis of dFC between all possible regions and/or voxels, using the sliding window correlation (SWC), is complex, computationally expensive, and difficult to interpret. As a result many dFC studies have explored the connectivity between only a few regions of interest (ROIs) in the brain, limiting the spatial extent of the analysis [42, 103, 37]. These studies assumed that the spatial composition of the networks was constant over time [42, 2]. However, it is possible that either (a) the spatial extent of a network or (b) the regions that compose a network vary over time. Examination of this spatial variation of networks over the course of a scan would help in segregation of constant and variable parts of these networks. This segregation can reduce further processing by focusing only on the variable portions of these networks.

In addition to exploring the dynamics of the FC, it is important to establish methodologies that can identify areas with various discrete connectivity states in the correlations, e.g., areas that may be correlated with the seed voxel part of the time and anti-correlated or uncorrelated the rest of the time. In the second part of this study, we introduced a new method to identify these areas by comparing their SWC histograms of the seed region of interests (ROIs) with the standard normal histogram using KL divergence. In particular, these histograms were examined for multi-modal rather than unimodal structure that could indicate discrete states of connectivity between the somatomotor cortex or the caudate putamen with the rest of the voxels

in the brain. These methods are readily translatable to human subjects and may be used to obtain a better understanding of the spatial variability of networks and how it can affect dynamic analysis.

3.2.2 Materials and Methods

All experiments were performed following guidelines set by the Institutional Animal Care and Use Committee (IACUC) of Emory University. Three scans each from four male SpragueDawley rats ($200 - 300$ g) were chosen from data acquired for another study and analyzed in [42, 60]. Animal preparation and preprocessing in described below.

3.2.2.1 Animal Preparation

Each rat was imaged under a subcutaneous infusion of 0.05 mg/kg/hr dexmedetomidine [60]. Approximately eighty minutes after the initial dexmedetomidine bolus, the infusion dosage was increased to 0.15 mg/kg/hr (3x initial infusion rate) for maintaining the anesthetic depth, in accordance with the protocol established in [71]. Heart rate and blood oxygen saturation percentage were recorded with a pulse oximeter placed on the rear left paw. The respiratory rate was measured by using a pressure-sensitive pad placed under the rats chest. Body temperature was monitored with a rectal thermometer and maintained at approximately 37°C (+/- 0.5°C) using an adjustable warm water pad.

3.2.2.2 Image Acquisition and Processing

All images were acquired on a 20 cm horizontal bore 9.4 T Bruker BioSpec magnet interfaced to an AVANCE [11] console, using a 7 cm volume coil for RF transmission and a 2 cm surface coil for signal reception. A FLASH image was acquired in three planes and a single slice was positioned over the primary somatosensory cortex (S1). Each resting state scan was acquired using a single-shot gradient echo EPI sequence

with the following parameters: Repetitions = 1000, TR = 500 msec, TE = 15 msec, total scan time = 8 minutes 20 seconds, slice thickness = 2mm, FOV = 2.56cm x 2.56cm, matrix size = 64 x 64. Approximately ten resting state scans were acquired from a total of seven animals for the original study. For the analysis performed in this work, we used the same three resting-state scans each from the four rats examined in [42]. For the period when the scans were acquired for this analysis, the average heart rate was 300-310 bpm; respiratory rate was 70-80 breaths per minute; oxygenation was 98-99 %; and body temperature was 37-37.5°C. These scans were chosen due to the excellent stability of the animals over the course of multiple scans.

All fMRI data processing and analysis was performed using code written in MATLAB (MathWorks, Natick, MA). The time course from each voxel was linearly detrended, followed by FIR band pass filtering between 0.01 Hz-0.3 Hz based on previous work demonstrating correlation over a wide range of frequencies in the anesthetized rat [59, 62]. Data points were removed from the beginning of each scan to reduce any transient effects of scanner instability, and again after filtering to reduce filter effects, leaving a total of 800 images for each scan. Three scans from each rat were concatenated after motion compensation for further processing. This concatenation was possible since the same slice of each rat was scanned three times. As a result, the scan of each rat consisted of 2400 (3x800) images, which was equivalent to 1200 seconds of scan time.

3.2.2.3 Study Sequence

This study started with the computation of the stationary correlation of seed ROIs in the left primary somatosensory cortex (LS1), the right primary somatosensory cortex (RS1), the left caudate putamen (LCP), and the right caudate putamen (RCP) with rest of the brain. The locations of the seed ROIs were identified by visual comparison with the Paxinos rat brain atlas [101].

After stationary FC analysis, the SWC between each seed ROI and the rest of the brain was calculated to show the variations in the spatial pattern of their FC as a function of time. Averaged SWC was compared to the stationary correlation to observe their similarity and differences. To further explore the spatial variability, SWC maps were thresholded, binarized, and displayed after non-overlapping equal intervals for visual inspection of the changes in spatial connectivity over time. These maps, plotted at every fifty seconds, were clustered using the k-means algorithm, with cluster validation based on Dunn's index [30]. Afterwards, the data was examined for the presence of discrete states by comparing the standard normal histogram with SWC histograms of the seed ROIs by using KL divergence. We hypothesized that the high KL divergence histograms would be bi- or multi-modal indicating the presence of discrete connectivity states. The next sections describe this study sequence and results in detail. The detailed results are for left somatosensory cortex (LS1) and left caudate puteman (LCP) of one rat, selected at random.

3.2.2.4 Voxel Blocks

The main aim of this study was to observe the dynamics of the FC of seed ROIs with all the other areas instead of with a few preselected ROIs using the SWC, which would require very extensive computation even in the relatively small rat brain. Furthermore, single voxel time series has low signal-to-noise ratio (SNR) which is increased by averaging. The number of computations was reduced and SNR was increased by dividing each 2D image into non-overlapping blocks of 3x3 voxels that were used as computational units for this study. The block size of 3x3 voxels was chosen because it is approximately the size of the areas in S1 or CP that exhibited significant bilateral correlation in previous studies [102]. The intensity of a block was the mean of the intensities of voxels in that block, and its intensity for the whole scan length comprised its time series. For rest of the paper, the term 'block' refers to 3x3

blocks of original voxels unless otherwise specified and these blocks are the smallest functional units for this study.

3.2.2.5 Stationary and Averaged Dynamic Functional Connectivity

Pearson correlation coefficients of the time series of all blocks were computed pairwise with each other for the entire scan length to compute stationary correlation and the values ≥ 0.2 *or* ≤ -0.2 were stored in a matrix called "stationary correlation matrix". Next we computed the SWC for a series of 50 second windows (100 TRs) , with each window's starting point one TR ahead of the previous window for both signals. The window size was chosen to reflect the time at which BOLD-LFP (local field potential) correlation reached a stable plateau in [92] and is comparable in length to another rodent study that employed sliding window analysis [42]. Pearson correlation coefficients of the windowed time series of all blocks with each other was computed and saved in matrices called "dynamic correlation matrices", keeping SWC values ≥ 0.2 *or* ≤ -0.2. Figure 2., shows the block diagram for computation of stationary FC, dFC and averaged dFC. The stationary correlation matrix and dynamic correlation matrices represent the stationary and variable inter-connectivity of all blocks in the brain. These matrices could be used to extract and examine the FC of any block with the rest of the brain.

For the rest of the analysis, we extracted all correlations of specific seed blocks with rest of the brain from the stationary correlation matrix and the dynamic correlation matrices to examine their FC with the whole brain. We validated the use of the bigger size (3x3 voxels) of functional blocks by comparing the mean of the absolute value of dynamic correlation matrices with the stationary correlation matrix. For better visualization of stationary FC and average dynamic FC of seed blocks, the corresponding FC maps were plotted.

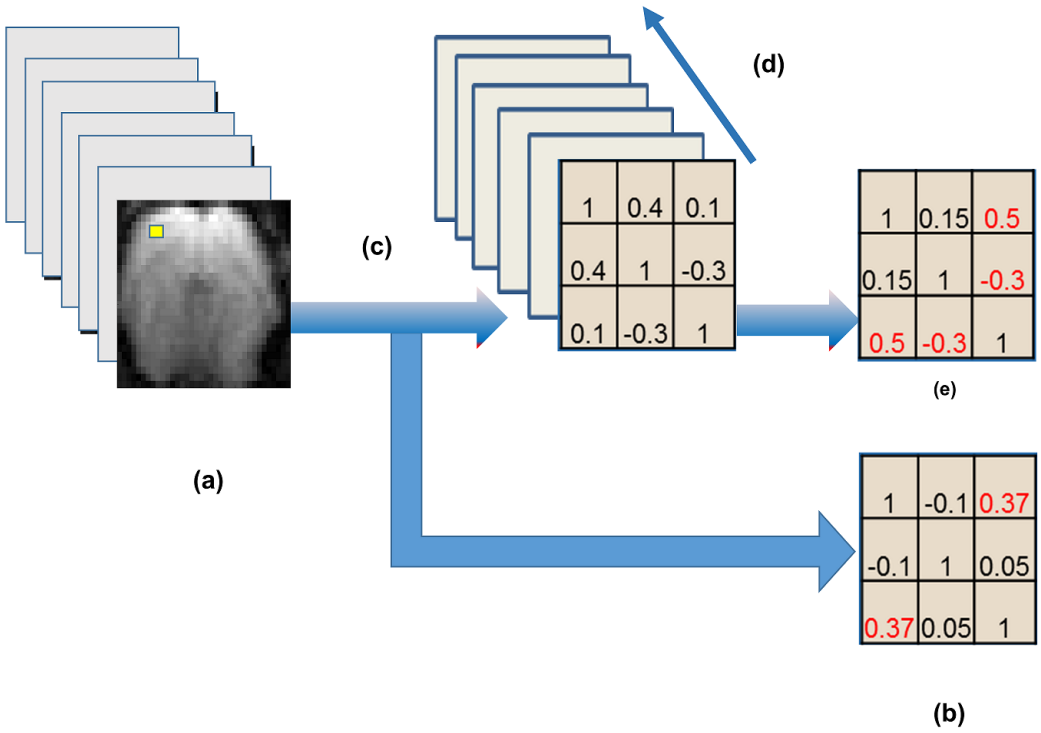

Figure 2: Block diagram for computing stationary and averaged dynamic functional connectivity. (a) Resting state fMRI scans of a rat scanned at 0.5 second TR. The resolution of the scanned images was reduced by combining them in blocks of size 3x3 (shown in yellow). (b) Stationary correlation among all the blocks in the brain. Red entries are for the correlation values above the threshold which was $0.2 \leq |\textit{stationary correlations}| \leq 1$ (c) Sliding window correlations of all blocks with each other. Window size was fifty seconds (100 TRs) and offset was 1 TR. (e) Averaged dynamic functional connectivity. Red entries are for the correlation values above the threshold which was $0.2 \leq |\textit{mean sliding window correlation}| \leq 1$.

3.2.2.6 Persistence of Functional Connectivity

For further analysis of the spatial variability in the FC, the percentage FC of all blocks with the seed blocks was calculated by adding the number of times any block was functionally connected with the seed block from the dynamic correlation matrices and dividing the sum by the total number of dynamic correlation matrices. For example, for a block x that is functionally connected with a seed block m times out of total n dynamic correlation matrices, the percentage FC would be $\frac{m}{n}$*100. This process gave a whole brain percentage FC map of the seed block from which a sub-map containing the voxels that were functionally connected for more than a certain percentage of time could be extracted.

3.2.2.7 Binary Transformation and k-means Clustering

For visual comparison, the non-overlapping dFC maps of seed blocks were captured at intervals of fifty seconds for the whole scan length. Afterwards these FC maps were clustered using k-means to map distinct FC states present over the course of the scan.

Before clustering the dynamic correlation matrices were binarized by replacing SWCs of functionally connected blocks of seed blocks by '1' and others by '0' This binarization was done since our interest in the initial study was just to explore the existence and the extent of variable/non-variable regions of FC and not in the actual values of the variations themselves. These binary correlation matrices were transformed into row vectors, which were used as feature vectors for k-means clustering performed using the kmeans() function in MATLAB (Euclidean distance, random choice of centroids, 1000 iterations, five repetitions). Figure 3. shows the block diagram for the process of clustering the dFC patterns.

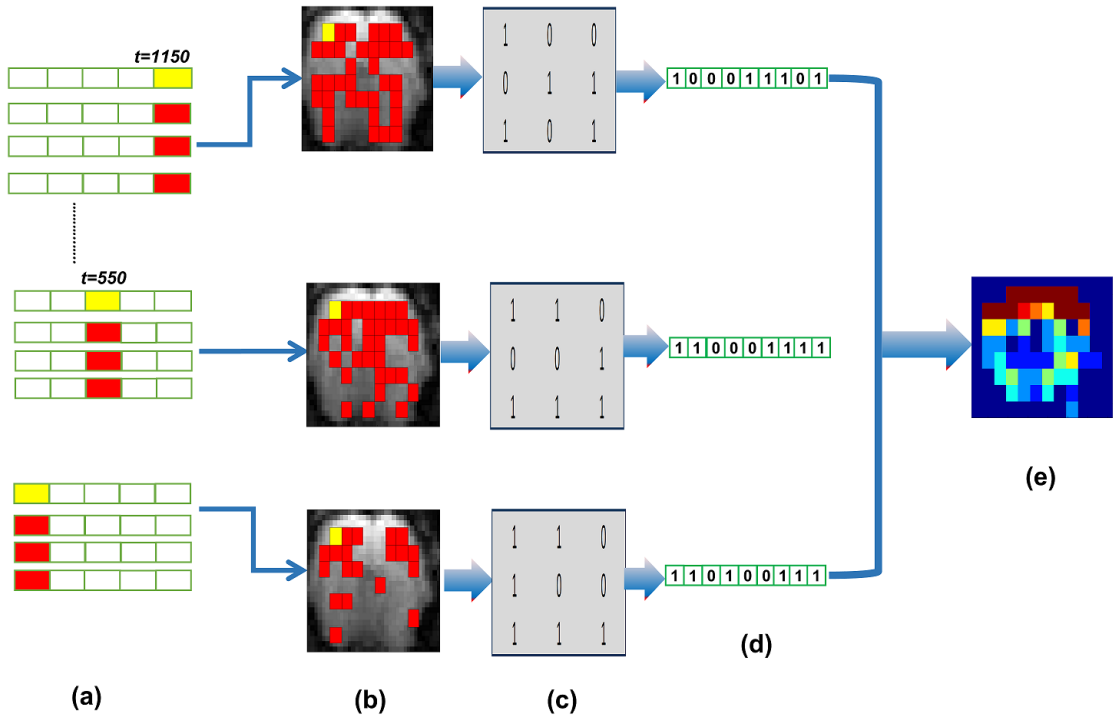

Figure 3: Block diagram of the sequence of operations performed to cluster the dynamic functional connectivity patterns. (a) Time series of seed and other blocks in the brain. Sliding window correlation is performed by taking 50 seconds (100 scans) window of seed block (yellow) and correlating it with same size windows (red) of all other blocks' time series in the whole brain. (b) Dynamic functional connectivity patterns of seed blocks at intervals of 50 seconds. The yellow square indicates the seed block, and red ones are the blocks functionally connected with it. (c) The functional connectivity patterns are binarized and (d) converted into row vectors to be used as feature vectors in k-means algorithm. (e) The resulting cluster patterns indicate how often each block is included in a given cluster.

3.2.2.8 States of Dynamic Functional Connectivity and Clustering Validation

Each of the clusters represented one discrete state of FC for a seed block, and the number of members in a cluster indicated the number of similar dynamic FC maps that were present in that state. K-means is an unsupervised clustering technique and requires some validation to decide the optimum number of clusters, which involves a trade-off between data compression and accuracy of the representation. There are several methods for cluster validation in such situations, including Davies-Bouldin index, Modified Hubert statistic, and Dunn's Index (DI) [30]. DI was used for this study since it aims at the identification of "compact and well separated clusters" by computing the ratio of inter-cluster and intra-cluster distances [30]. Increasing the number of clusters should generally increase DI, but initially DI started to decrease with the increase in number of clusters, so the optimum number of clusters was taken as the one after which DI either increased or became constant. The optimum number of clusters obtained by k-means clustering of the dynamic FC patterns was different for each seed block, based upon the amount of variability in its FC over time.

3.2.2.9 Discrete States of Functional Connectivity using Kullback-Leibler Divergence

It is important to establish methodologies that can identify the areas with various discrete connectivity states in the correlations (e.g., areas that may be correlated with the seed ROI part of the time and anti-correlated or uncorrelated the rest of the time), since their identification would limit the dynamic studies to these areas only reducing the computations to a large extent. In the second part of this study, we introduced a new method to identify these states by comparing SWC probability distributions of the seed ROI with the standard normal probability distribution (null hypothesis [42]) using KL divergence. The KL divergence of discrete probability distribution Q

from P for i values is given by DI_{KL}:

$$DI_{KL}(P \parallel Q) = \sum_i P(i) \log \frac{P(i)}{Q(i)} \tag{5}$$

In particular, these distributions were examined for multi-modal rather than uni-modal structure that could indicate discrete states of connectivity between the seed ROI with the rest of the blocks in the brain. It has previously been shown that the correlation histograms for randomly matched time courses are approximately normal [42] so we hypothesized that probability distributions having high KL divergence from the standard normal distribution may exhibit bimodal or multi-modal behavior, indicating the presence of two or more distinct states of FC. Before the computation of KL divergence, a normalized Fisher Z-transform was applied to all correlation values using the MATLAB function $atanh(r)$, where r is the correlation value. Histograms were converted to probability density functions and the KL divergence between all SWC probability density functions and the standard normal probability density function $N \sim (0, 1)$ was computed. The KL divergence was divided into two groups of low ($\min \leq \ KL\ divergence\ < \frac{max}{2}$) and high ($\frac{max}{2}\ < KL\ divergence\ \leq max$) divergences for each seed. The standard normal histogram was generated in MATLAB using the randn() function.

3.2.3 Results

Substantial variability in the spatial extent of both cortical and subcortical networks was observed, even in the anesthetized rat. However, little evidence of discrete states of connectivity was observed, and it was primarily limited to voxels on the periphery of the S1 network. This suggests that the lack of correlation between SI and CP is not likely to be due to transitions between correlated and uncorrelated states.

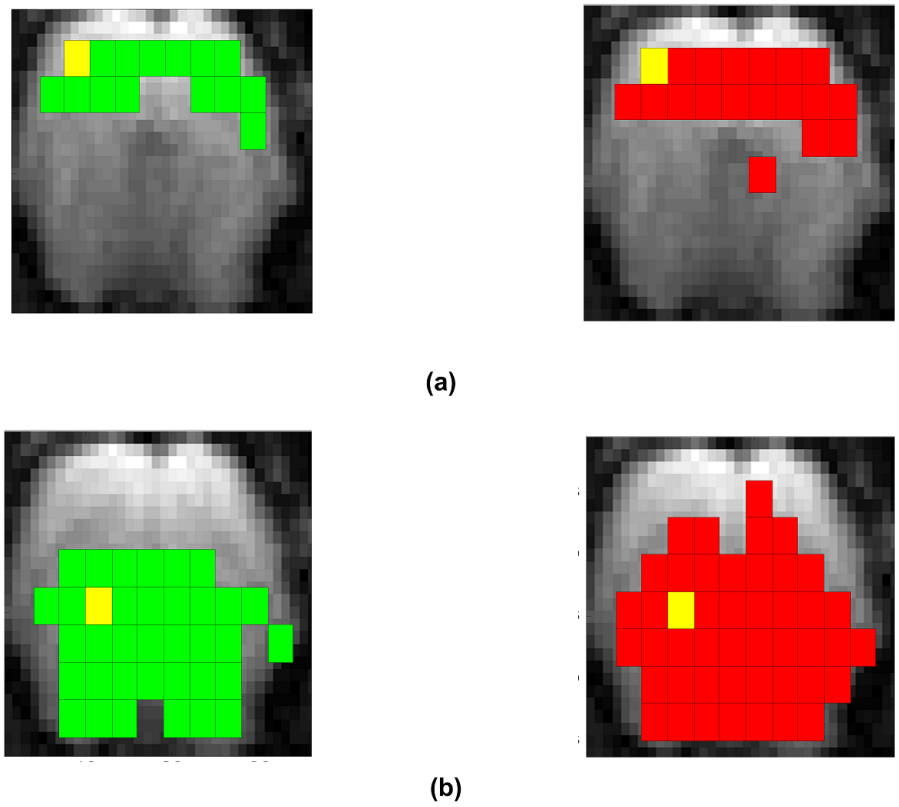

Figure 4: Maps of stationary and averaged dynamic functional connectivity for seed blocks in LS1 and LCP. In each figure, the yellow square indicates the seed block. Green and red squares represent the functionally connected blocks for stationary and mean sliding window correlation respectively in (a) LS1 and (b) LCP.

3.2.3.1 Stationary and Averaged Dynamic Functional Connectivity Comparison

Averaged dFC maps were similar to stationary functional connectivity (FC) maps, as expected. These FC maps for two blocks (LS1, LCP) in one of the rats are shown in Figure 4.

Similar maps were obtained for all the rats. In almost all cases, the maps of averaged FC were bilateral and nearly symmetric, as expected, and were similar to previously observed seed-based correlation maps in steady state or stationary analysis [71]. For all seed blocks in all rats, the averaged dynamic FC patterns always contained the stationary FC patterns as a subset along with additional blocks. In the case of LCP and RCP, averaged dynamic FC covered much of the subcortical

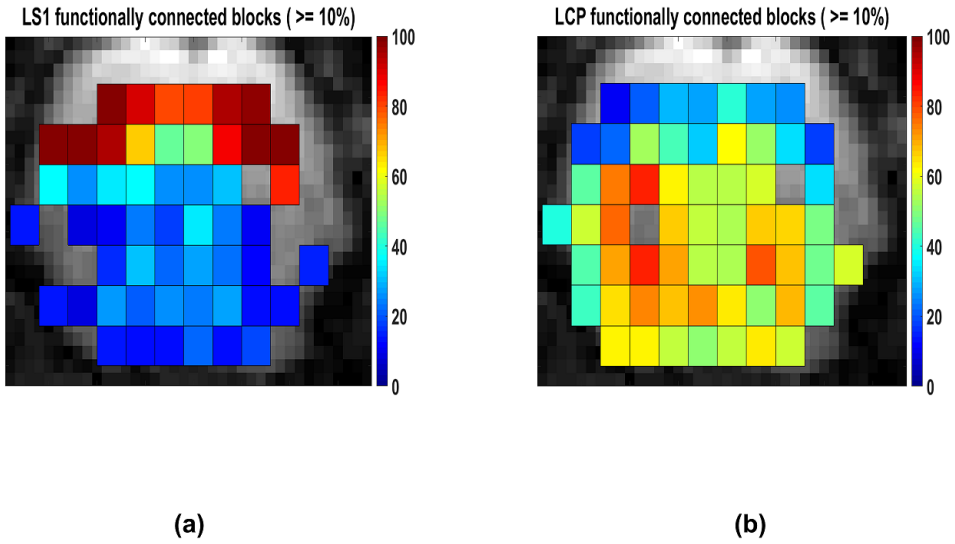

Figure 5: Percentage functional connectivity of the seed blocks in LS1 and LCP of one rat. (a) Blocks functionally connected with the seed LS1 block for $\geq 10\%$ of the times. The largest percentage of the functionally connected blocks is in RS1 region or in the neighborhood of the seed, with the percentage decreasing as the distance of the blocks from the seed increases. A very few blocks are functionally connected with the seed block for more than 90% of the times. Similar observations can be made for LCP in (b).

area. All the seed blocks were functionally connected with their neighboring blocks. Stationary and mean FC maps were similar for all rats, validating the use of a block of 3x3 voxels as the unit for spatial variability analysis.

3.2.3.2 Percentage of Functionally Connected Blocks

The spatial extent of the FC of the seed blocks was variable, as shown by the percentage FC maps of LS1 and LCP of one rat in Figure 5.

Figure 5. (a) shows the blocks that were functionally connected with the seed

block (LS1) for at least 10% of the time. The blocks with the highest percentage of FC (deep red) were concentrated in the left and right S1. The pattern was bilateral and symmetric, similar to the result of stationary FC. The findings for LCP were similar as shown in Figure 5. (b)). An important observation from all of these maps is the presence of high percentage FC blocks in the bilaterally symmetric regions of the seed blocks, with the percentage decreasing gradually as the distance of a block from the seed block increases.

Furthermore, the percentage FC for these blocks were higher for seeds in S1 than the seeds in CP with none of the blocks functionally connected with LCP for more than 90% of the times, and a very few for even more than 80% of the times, which may be due to the fact that left and right S1 are directly connected but left and right CP are not [102, 71, 108].

The mean number of blocks that were functionally connected with each of the four seed blocks for different percentages of time in all four rats are plotted in Figure 6. The mean percentage of the blocks functionally connected with the seed block is almost same for the extreme cases ($\geq 10\%$ *or* $\geq 90\%$), but the decrease in this number is more gradual (almost linear) for CP seed blocks than for the S1 seed blocks, particularly for LS1.

3.2.3.3 Functional connectivity patterns at different times

Figure 3. shows the block diagram of the process starting from the computation of the SWC and ending at clustering of FC patterns at every 50 seconds. Figure 7. shows first four dynamic FC maps (at non-overlapping intervals of 50 seconds) for two blocks (LS1, LCP) in one rat. It can be observed that a portion of the stationary FC containing bilateral areas (RS1 for seed in LS1, and RCP for seed in LCP) is present in all of these plots showing the portion of the FC network that is persistent throughout the scan. These figures clearly illustrate that each cortex was functionally

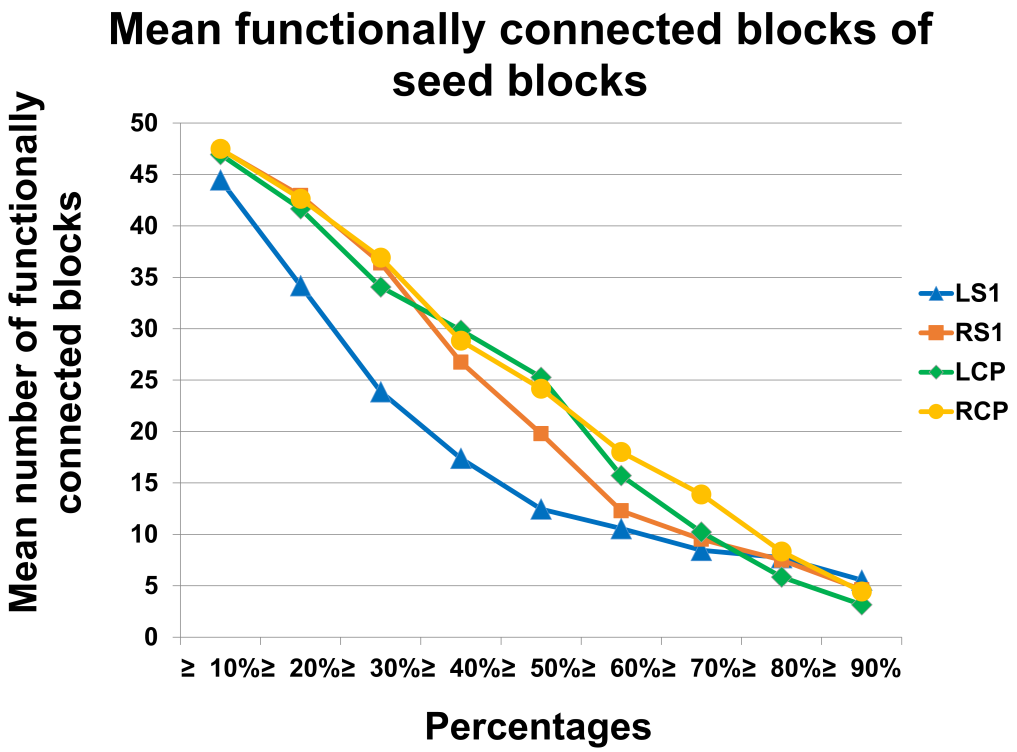

Figure 6: Mean of the functionally connected blocks of the seed block for all the rats. The mean is plotted against various percentages of the functionally connected blocks along the x-axis.

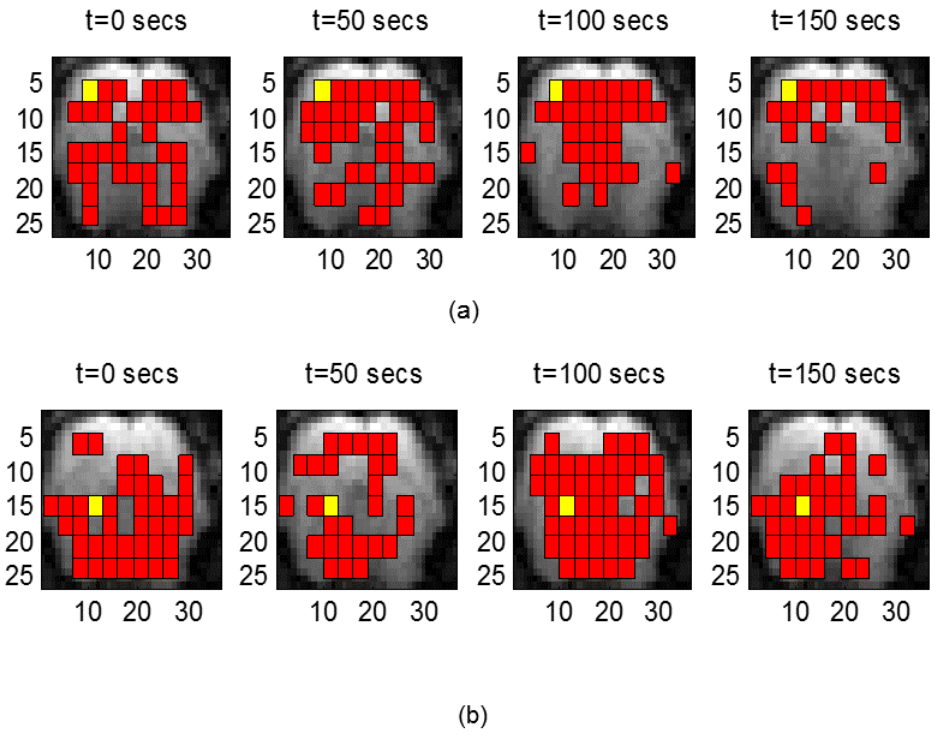

Figure 7: Functional connectivity patterns of seed blocks in (a) LS1 and (b) LCP in one of the four rats. The seed voxels are plotted in yellow color while the other functionally connected blocks are plotted in red. The patterns are plotted at non-overlapping intervals of 50 seconds. The constant and variable portions of connectivity are evident in these functional connectivity patterns.

connected with the corresponding cortex in the other hemisphere at all times, which was expected since steady state or stationary analysis consistently shows bilateral correlation as shown in Figure 4. The spatial extent of the correlation and the degree of correlation between cortical and sub-cortical regions varied. The FC patterns for S1 seeds were mostly localized to cortical regions, though some connectivity in the subcortical regions was also observed. Similarly, FC for seeds in CP was mostly confined to subcortical areas, with connectivity to cortical regions occasionally present. Similar to this rat, in other rats also a part of the dynamic FC was invariant, while the other part varied for all seed blocks.

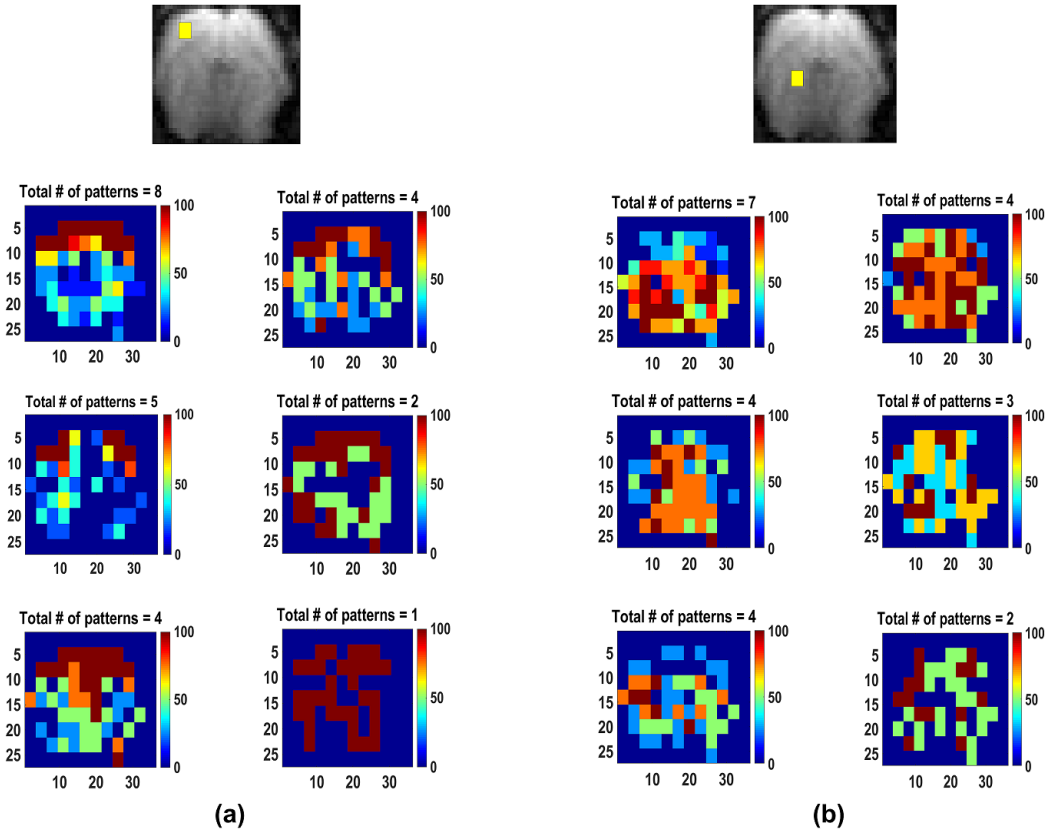

Figure 8: Clustered patterns of dynamic functional connectivity for the seed in (a) LS1 and (b) LCP in one rat.

3.2.3.4 Clustering of Dynamic Functional Connectivity Patterns

Afterwards, these dFC patterns were clustered using k-means to map distinct functional connectivity (FC) states present over the course of the scan. k-means clustering is an unsupervised clustering technique that automatically partitions an n-point data set into k clusters, where $k < n$ [58]. It minimizes the within-cluster sum of squares by the formula given in Equation (6).

$$arg\min_{s} \sum_{i=1}^{k} \sum_{x_j \in s_i} \| x_j - \mu_i \|^2 \tag{6}$$

in which $S = \{S_1, S_2, ..., S_k\}$ is the cluster space of member clusters, μ_i is the mean of the feature vectors in each member S_i, and $x_j = \{x_{j1}, x_{j2}, ..., x_{jn}\}$ are feature vectors of dFC to be clustered.

Figure 8. shows dFC maps in different clusters for the seed block in left somatosensory cortex (LS1) and left caudate putamen (LCP) for one of the rats. The colorbar for each cluster shows the percentage of times a certain block was part of a specific cluster. For example, if the total number of maps or patterns in a cluster were m, then the deep red (100 on the color bar) would show the blocks that were present in the cluster in all of those m maps or patterns giving a percentage of 100. For LS1 (Figure 8. (a)), it can be observed that there is a persistent bilateral, almost symmetric FC pattern that includes RS1. Same trend was observed for LS1 in others rats. There was some varying FC in the subcortical regions also but these variations were not consistent across rats.

Similarly Figure 8. (b) shows that LCP was almost always functionally connected with RCP with bilateral, non-symmetric patterns which extended into subcortical region. The seed blocks (LS1, LCP) were almost always functionally connected with their neighboring blocks. Clustered patterns of dynamic FC for RS1 and RCP seed blocks were similar with largest amount of functional connectivity in LS1 (for RS1) and LCP (for RCP). It was observed in almost all of these cluster distributions that bilateral patterns which were similar to steady state FC patterns, shown in Figure 4, were persistent, indicating that some parts of the brain exhibit correlated activity throughout the scan time.

3.2.3.5 Cluster Validation

Cluster validation was done using DI, since it aims at the identification of 'compact and well separated clusters'[30]. Dunn's index [31], DI_m, for m clusters is given Equation (7).

$$DI_m = \min_{1\leq j\leq m}\left\{\min_{1\leq i\leq m, j\neq i}\left\{\frac{\delta(C_i, C_j)}{\max_{1\leq k\leq m}\Delta_k}\right\}\right\} \tag{7}$$

in which $\delta(C_i, C_j)$ is the inter-cluster Euclidean distance between clusters C_i and C_j, $\Delta_k = d(x, y)$, and $d(x, y)$ is the Euclidean distance between the points x and y in the

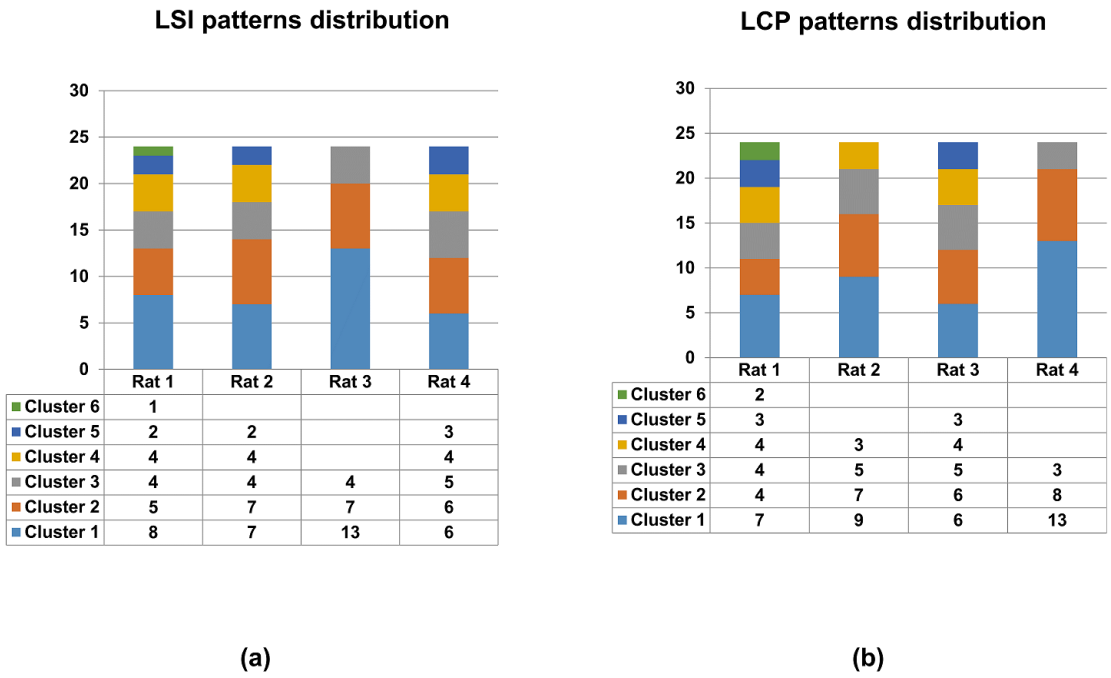

Figure 9: Distribution of patterns in clusters for LS1 (a) and LCP (b), in all rats for the optimum number of clusters based on Dunn's index. 70-75% of the patterns are in three clusters when the total number of clusters is ≥ 5, and 83% of the patterns are in two clusters when total number of clusters is 3, suggesting that patterns are not widely different from each other.

cluster C_i.

Figure 9. shows the distribution of patterns in clusters. The distribution within the clusters was not uniform; rather, most of the patterns were in a few of the clusters. If the optimum number of clusters was greater than five then $70-75\%$ of the patterns fell into three clusters and if optimum number of clusters was less than five more then 80% of the patterns were part of two clusters. The presence of a large number of patterns in only a few of the clusters suggests that even though spatially variable FC exists, the patterns at different times were not vastly different from each other. Similar kind of distribution of patterns was observed for all seeds (LS1, RS1, LCP,

RCP) in all rats.

3.2.3.6 Discrete States of Functional Connectivity

The KL divergence was divided into two groups of low ($\min \leq KL\,divergence < \frac{\max}{2}$) and high ($\frac{\max}{2} \leq KL\,divergence < \max$) divergences for each seed. From Figures 7 and 8 we expected to see fewer discrete states of FC for the blocks that were either adjacent to the seed block or were contralateral to it. In fact, we did observe a trend of low KL divergences (magenta in Figure 10. (a), right)) blocks in these areas for almost 70% of the cases, while the high KL divergence (blue in Figure 10. (a), right) blocks were farther from the seeds. Figure 10. also shows a few unimodal histograms of low KL divergence blocks (b, left) and few bimodal ones of high KL divergence blocks (b, right). Most of low KL divergence histograms were unimodal, with no clear separation of states; however, not all of high KL divergence histograms were bi- or multi-modal.

3.2.4 Discussion

This part of the chapter examined two aspects of dynamic functional connectivity: First, the spatial variability of seed-based networks and second, the possibility of detecting discrete states of connectivity based on the correlation histogram. For the first part of the study, changes in the spatial extent of each network over time were determined using SWC, and clustered into groups using the k-means algorithm. In the next part, we used Kullback-Leibler (KL) divergence to search for multi-modal correlation histograms that could indicate discrete states of FC between a seed block and other blocks. These methods were applied to data from well-characterized somatomotor and caudate putamen networks in the rat.

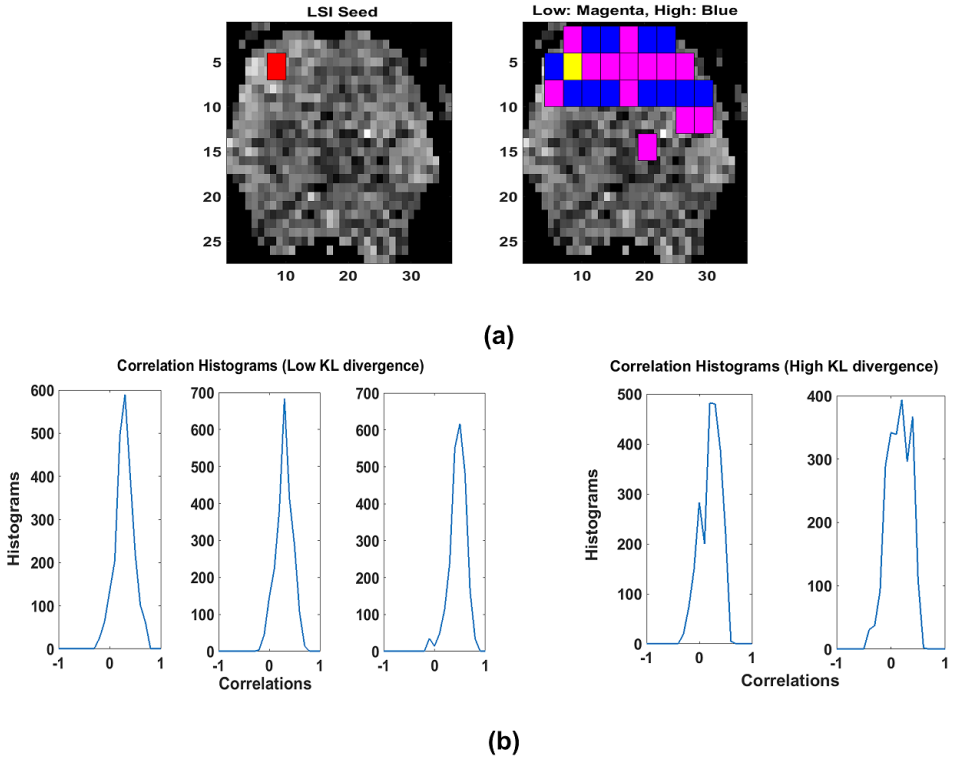

Figure 10: Low(magenta) and high(blue) KL divergence blocks (a, right) of seed in LS1 (a, left, red) along with a few low KL divergence histograms (b, left) and high KL divergence histograms (b, right). High KL divergence are bimodal while low ones are not.

3.2.4.1 Functional Connectivity Maps or Patterns

For this study, first we down-sampled all the scanned images into 3x3 blocks based on the observation that the adjacent pixels are typically correlated due to both the application of the filter on the BOLD signal and the correlation introduced by the imaging sequence. Clearly, dimension reduction could be carried out in a more sophisticated manner (perhaps using an atlas for segmentation) or could be eliminated entirely at the expense of longer processing time, but for the purposes of this exploratory analysis, we felt that the block-based approach should suffice. In order to test the validity of our approach, static or stationary FC was computed first and compared to results of previous studies. Encouragingly, despite this spatial down-sampling, the FC maps exhibit patterns similar to those seen in previous rat work, with strong correlations between LS1, RS1 and LCP, RCP [42].

Comparison of stationary FC and averaged dynamic FC showed that on average the stationary FC portions were consistent throughout the scan time for all seed blocks even when dynamic analysis is used. This is an interesting finding which indicates that at least some portion of the networks observed with steady-state analysis do not vary much over time. Averaging of dynamic FC patterns contained some regions in addition to the static FC regions and these regions changed configurations, which revealed that a portion of dynamic FC was variable and should be explored further for better understanding of FC network dynamics.

3.2.4.2 Time Extent of Spatial Correlation

Variability in the spatial extent of correlation as a function of time was observed for all seed regions. Similar to the spatial variability reported in the DMN in [43], certain blocks in our networks were connected to each seed at a majority of time points, while others exhibit FC at certain times only. The blocks that were always connected were typically located adjacent to the seed or in the homologous area of the contralateral

hemisphere, matching well with the patterns obtained from steady state analysis. The blocks that exhibited more variable connectivity sometimes included areas of CP (for S1) or S1 (for CP seeds). These findings motivated the use of k-means clustering to identify common patterns that characterize the network. We would like to mention here that the variability observed on anatomical edges (e.g.; between gray matter and white matter) may be the result of the noise due to mixing of neural and non-neural tissues during down-sampling but it would not influence our main finding about the presence of spatial variability that was observed in pure gray matter too.

3.2.4.3 K-means Clustering of Patterns

The optimum number of clusters varied from 3 to 6 across rats for all seed regions. Though the extent of variability and number of clusters changed for different rats and for different seed regions, yet most of the patterns fell within a few clusters, suggesting strong similarities in FC at different times. Regardless of the number of clusters, or the number of patterns in a cluster, certain spatial distributions of FC were always present, emphasizing the point that part of the FC is not dynamic, providing a constant network between certain brain areas even during rest. A relatively small number of clusters (3-6) described the data well. This may be affected by a reduced repertoire of states in the anesthetized animal, but the number is similar to that previously used on awake human data [2]. The spatial variability may also have been reduced by the use of anesthesia. Clustering of the patterns identified two important aspects of variability in functional connectivity (FC): (1) the spatial configuration of FC did not change dramatically over time as most patterns were within few clusters (2) A part of the spatial pattern of FC was present at all times points and corresponded to the network observed in steady state analysis.

3.2.4.4 Kullback-Leibler Divergence for Discrete State Identification

Kullback-Leibler (KL) divergence was used to explore presence of discrete FC states between seed blocks and other blocks in the brain. Since randomly-matched time courses gave approximately normal histograms of correlation coefficients, we examined correlation histograms that exhibited high KL divergence from the standard normal distribution for evidence of multiple peaks. We hypothesized that these peaks could indicate discrete states of connectivity that were visited over the course of the scan. If such peaks could be detected, the KL divergence could be used to identify areas with the most variable connectivity and further FC analysis could be restricted to those areas only. For high KL divergence blocks, there were some bimodal and even multi-modal distributions in the somatosensory cortex network, but few multi-modal distributions were observed for the caudate putamen network. Most of the low KL divergence distributions were Gaussian-like and unimodal, pointing towards the view that the connectivity patterns did not alternate between discrete states. This is in agreement with the clustering analysis, which finds that the variability in spatial extent of connectivity was primarily confined to peripheral areas joining or leaving the network. No transient anti-correlation was observed.

3.2.5 Limitations and Future Directions

The use of an anesthetized animal model in this study is both a limitation and a benefit. Some of the variability in human subjects has been attributed to fluctuating levels of wakefulness [64], which is not present in the stable anesthetized animal. On the other hand, the variability due to cognitive processes that many studies are interested in detecting is also absent in the anesthetized animal. Nevertheless, sliding window BOLD correlation has been linked to changes in correlation in simultaneously-acquired band-limited power in the theta, high beta and gamma frequencies in the

anesthetized rat [92], indicating that perhaps the most basic sources of network dynamics can be explored in this animal model. Anesthesia affects both the neural activity and the vasculature and makes it difficult to compare results to human studies. However, the use of animal models enables the acquisition of simultaneous MRI and electrical recording [68]. Part of the motivation for performing this original analysis in the rat is that future studies that combine imaging and recording in both cortical and subcortical sites can determine if the variation in the spatial extent of the networks is due to changing neural coordination or merely fluctuations due to noise.

The analysis algorithm also has limitations. We chose to use k-means with Euclidean distance as the clustering measure, but k-means is not stable in the sense that it can converge to local centroids instead of global ones. Future studies could compare other clustering techniques. Other metrics like city block or mahalanobis distance measures or Davies-Bouldin (DB) index and Modified Hubert statistic may offer better and more compact clustering. Changes in correlation strength were not examined in this study, as the data was thresholded and binarized to simplify further analysis, but variations in the strength of correlation are a complementary aspect of dynamic FC that should be examined in future studies.

Some probability distribution matching measures other than KL divergence can also be applied in future. In particular, we anticipate that the identification of correlation coefficient histograms that exhibit multi-modal behavior may prove key to identifying areas involved in discrete brain states, a process that could greatly reduce the number of comparisons and time for computational analysis in data-driven exploratory studies.

Overall, this study suggests that sliding window analysis observed steady state or stationary networks of S1 and CP, and discovered that these networks are present at all time in resting brain of rodent. Observation of the connectivity patterns revealed

that a part of functional connectivity was persistently present at all times, while there were changes in remaining connectivity. Clustering of FC patterns is a promising approach to characterize spatial variability in functional networks.

3.2.6 Conclusion

The spatial variability extent of the FC in rodents was successfully captured in this part of the study. Using four networks from four rats we established the fact that the change in individual networks over time was not very large. We also discovered that the part of FC captured with stationary correlation analysis was almost always present in these networks. Using KL divergence, we established a new method to identify the variable parts of the networks only. Once these regions are identified, further analysis can focus only on them, ignoring the constant part of the FC. These results were obtained on anesthetized rats but are readily translatable in humans also. The results reported are for the SWC analysis using a window of size 100 TRs (50 sec) which was based on previous dFC studies [92, 42]. However, we performed the analysis on the windows of different lengths (50 TRs and 200 TRs) also and found that the variability of SWC results were more for 50 TRs window and less for 200 TRs window compared with 100 TRs window. As a result, the optimum number of clusters was also different. Our next aim was to perform the extent of variability analysis on the human brain data also that is done by using another approach and explained in the Section 3.3.

3.3 Low Dimensional Visualization of Sliding Window Correlation in Humans using t-SNE

The next aim of our study was to capture the extent of variability in the functional connectivity (FC) of humans. We used an approach different from rodents for this study since another recent study [43] already reported the spatial variability in humans using a similar approach, and reported results similar to our rodent analysis.

The dynamic functional connectivity (dFC) studies using the sliding window correlation (SWC) reported that the extent of variability changes with the change in the size of the window [42, 103, 37]. After the SWC, studies use k-means to cluster SWC results revealing the states of dFC [2, 52]. Since the extent of variability in SWC results changes with the window size so the number of states and their transitions would also change. The second part of this chapter applied dimensionality reduction technique t-SNE [98, 99] to capture the state variations of SWC results for different window sizes. t-SNE is a well-known dimensionality reduction technique from machine learning and is used in different domains [4, 47] but this is the first time it is used for visual comparison of SWC results in dFC networks. We reduced the dimensionality of the SWC results to three. Visual inspection of these plots in low dimension clearly identified fast transitions of states for smaller windows and vice versa.

3.3.1 Motivation

A number of dFC studies using the SWC performed the analysis on different window sizes [42, 103, 37]. These studies either report the comparison of pairwise correlations with all the window sizes [42, 103, 37] or they cluster the results for a specific window size using k-means and report the number of states found [2, 52]. These two approaches are complementary as one gives the pairwise SWC for all window sizes and other provides the state distribution for one specific window. Based on the larger variability for smaller windows and smaller variability for larger windows in pairwise SWC [42, 103, 37], it can be hypothesized that the number of states and state transitions for a network would be more for the smaller windows and vice versa. There is a need to compare these state transitions similar to the comparison of pairwise SWC for different windows. However, no study has done this analysis yet. In this part of the study, we used a new approach by applying dimensionality reduction

algorithm, t-SNE [98, 99] to visualize these results in low dimensions and to compare state changes of human dFC networks as a function of window length.

3.3.2 Methods and Materials

3.3.2.1 Data Collection

Data from an earlier study [91] was used for this study. The data was collected from 17 healthy subjects (8 females, 18 to 26 years). All 17 individuals underwent high temporal resolution fMRI while performing a psychomotor vigilance task (PVT). In this task participants fixated on a centrally presented black dot subtending 0.28 of visual angle on a gray background. When the dot changed to navy blue, participants pressed a button with their right index finger as quickly as possible. If participants failed to respond in 9 s, the dot returned to black. Each block lasted 8 min and the dot changed color between three and five times. Change onset was random for each participant (the delay time between onsets as an integer number of milliseconds randomly chosen from a range of 10,000 ms to 480,000 ms without replacement). Four fMRI runs of PVT performance were collected from each individual. Two fMRI resting-state runs were collected from each individual. In resting-state runs, individuals were told to lie quietly. In resting-state runs individuals fixated on the black dot, but it never changed to navy blue. Task-based and resting-state functional images were acquired with four horizontal slices at a TR of 300 msec. Standard preprocessing steps (slice time correction, motion correction, image segmentation, normalization, and registration) were performed followed by filtering (FIR, 0.01-0.08 Hz).

3.3.2.2 Data Preprocessing

The preprocessing was done in Statistical Parametric Mapping 8 (SPM8) using the marsbar region of interest (ROI) plug-in: T1 images were segmented into gray matter, white matter, and cerebrospinal fluid maps. The left precuneus ROI from the AAL Structural ROI library [95] was reverse normalized [14] from the MNI brain

template to the individual T1 images. Individual T1 images were spatially cropped and registered to same-individual EPI images and this transformation was applied to all segments and left precuneus ROI as well. Reverse normalization allowed analysis to be performed in individual space rather than normalized space. This was necessary because individual EPI images did not cover the whole brain and had decreased signal-to-noise ratio due to the short TR used in this study [91].

EPI data were first slice-time corrected and then motion corrected through registration to a mean of all EPI images using Analysis of Functional NeuroImages (AFNI). From AFNI the maximum total movement in each direction (X, Y, and Z) was recorded; 100 TR (30 s) were removed from the beginning of EPI and motion data to eliminate stabilization effects. EPI data were blurred with a spatial Gaussian with sigma of 2 x 2 x 1 voxels and size of 3 x 3 x 1 voxels. A finite impulse response filter was used with a length of 150 TR (45 s) and a pass band of 0.01 to 0.08 Hz. As behavioral onset times were recorded in milliseconds from the start of the functional imaging run in raw data, they were corrected for the removed TRs and the phase shift resulting from the filter. Each voxel within EPI data was quadratically de-trended [61] and divided by one standard deviation, resulting in unit variance. Mean signals were calculated for whole-brain and white matter and these signals, in addition to filtered and cropped motion parameter signals, were regressed from EPI data. Final EPI data were again set to zero mean and unit variance for each voxel. This produced a normalized BOLD signal [91].

3.3.2.3 Network Extraction

The vigilance task selected for this study contained both resting-state and task-based networks. The purpose of the study in this part was to observe how the size of the window would influence the state transition of the SWC results by visual inspection of the results in low-dimensional space. For this purpose we observed the changes

in DMN in resting-state scans. We selected left precuneus as the seed [91] for this purpose and computed the stationary correlation of the seed with all the voxels in gray matter. Based on the findings on [91] 10% highest correlated voxels of the seed (1,639 voxels) in gray matter were taken as DMN.

3.3.2.4 Sliding Window Correlation

Each subject had two resting-state scans that were concatenated before computation of the SWC. After extracting the DMN, (1639 highest correlated voxels of the seed in the gray matter) we performed the pairwise SWC of the seed in left precuneus with all the voxels in the DMN. The windows of sizes 41, 82, 164, and 333 TRs (12.5, 25, 50, and 100 secs) were used. The largest and smallest window sizes corresponded to the lower (0.01 Hz) and higher (0.08 Hz) cutoffs of the bandpass filter, and the other two were multiples of the smallest window size. The largest window size was based on the findings of [53] about the minimum window size to be at least $\frac{1}{f_{min}}$ to avoid spurious fluctuations, in which f_{min} is the minimum frequency of correlating signals. The smallest window size was based on the findings of [91]. The SWC of the seed region of interest (ROIs) with all the other voxels in default mode network (DMN) was computed for all of these windows. As a result we had a correlation map or image for every window. The number of these maps was dependent on the window size, with more maps for smaller windows and vice versa. Afterwards, we converted each correlation map into a row vector, computed pairwise stationary correlation between all pairs, and fed the resulting correlation matrix to t-SNE as similarity matrix. If we had n SWC maps for a specific window then this similarity matrix would be of size n x n. The dimensionality was reduced from n to three, in which n was the actual dimension of the SWC time courses (number of correlation images or maps) and was different for different windows.

3.3.2.5 Dimensionality Reduction using t-SNE

t-SNE is a technique to visualize high-dimensional data by allocating a location to each high-dimensional data point in two or three-dimensional space [98, 99]. It is an unsupervised dimension reduction technique. In the high-dimensional space, it converts the distances between the points into probabilities using Gaussian distribution. The pairwise similarity p_{ij} between two points x_i and x_j in high-dimensional space is given by:

$$p_{ij} = \frac{exp(-\|x_i - x_j\|^2/2\sigma^2)}{\sum_{k \neq l} exp(-\|x_k - x_l\|^2/2\sigma^2)} \tag{8}$$

In the low-dimensional space, it uses Student t-distribution with one degree of freedom. The pairwise similarity q_{ij} between two points y_i and y_j in low-dimensional space is given by:

$$q_{ij} = \frac{(1 + \|y_i - y_j\|^2)^{-1}}{\sum_{k \neq l} (1 + \|y_k - y_l\|^2)^{-1}} \tag{9}$$

If the map points y_i and y_j correctly model the similarity between the high-dimensional data points x_i and x_j, then the joint probabilities would be equal. t-SNE minimizes the single KL divergence between the joint probability distribution, P, in the high-dimensional space and joint probability distribution, Q, in the low-dimensional space by using a gradient descent method on the cost function given by:

$$C = \sum_i KL(P_i \| Q_i) = \sum_i \sum_j p_{j|i} \log \frac{p_{j|i}}{q_{j|i}} \tag{10}$$

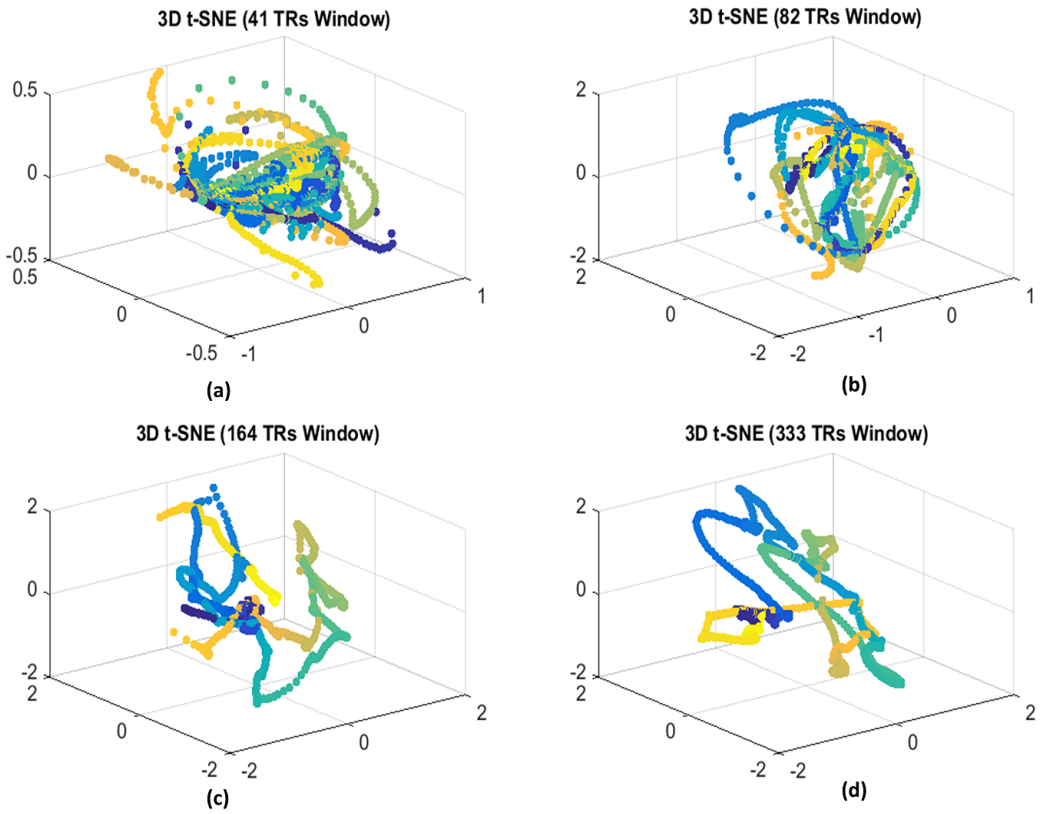

Figure 11: 3D-tSNE plots of state transitions captured by sliding window correlation for (a) 41 TRs, (b) 82 TRs, (c) 164 TRs, and (d) 333 TRs. The color map used is parula in which the starting time points are displayed in blue, followed by green, and then yellow. The smaller windows have intertwined trajectories that transition to smoother ones as the window size increases.

3.3.3 Results

The 3D visualization of t-SNE results illustrated different patterns of state change for different window sizes.

Figure 11. shows these images for all window sizes for one subject. The color map used is parula in which the color of the starting time point is dark blue, which changes to the green and then to the yellow as the time progresses. The colors are more concentrated around a point for smaller windows compared to larger ones.

The plots of smallest (41 TRs) and largest (333 TRs) windows from another angle are shown in (Figure 12.). Jumps in the plot are seen for 41TRs windows in (a)

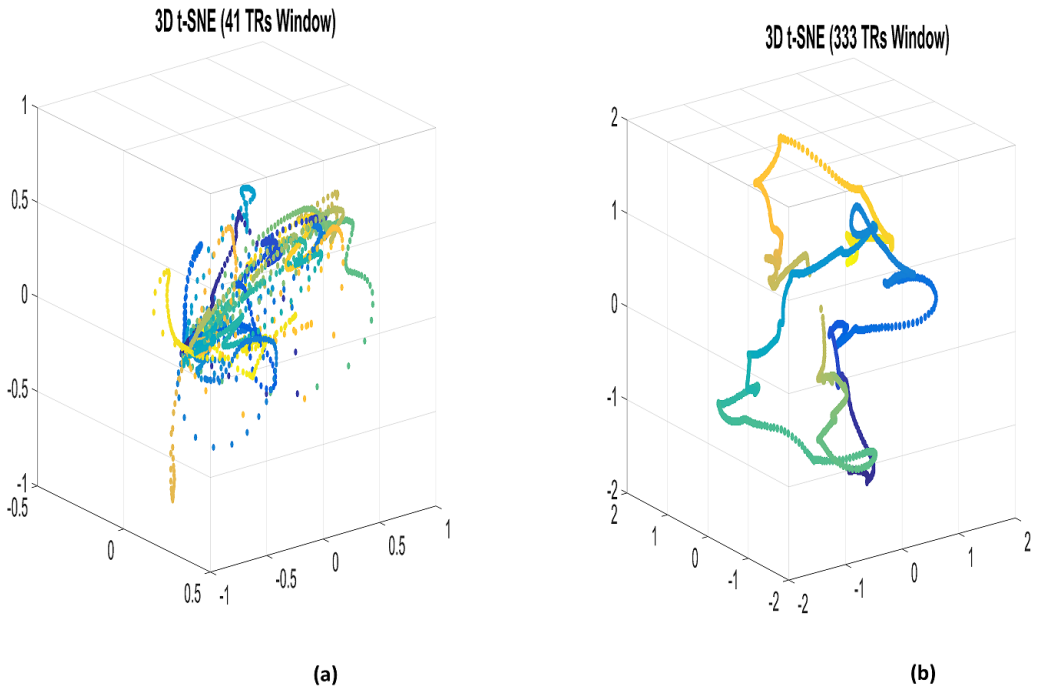

Figure 12: Short-lived state transitions are captured by smallest window (41 TRs) on left while the longer ones are captured by largest window (333 TRs) on right.

compared to smoother trajectories for 333 TRs window in (b). We performed the analysis on five subjects and similar results were observed in all cases.

3.3.4 Discussion

t-SNE reliably preserved the structure of state transitions from higher to lower dimension by capturing short-lived state for small windows and longer one for large windows. It can be observed from the Figure 11. that the brain states are more concentrated or closer for shorter windows as compared to longer ones. Figure 12. shows that the smallest window captures the short-lived states of the network, as shown by very large number of jumps, while the largest window has smooth state transitions capturing the longer states.

3.3.5 Limitations and Future Directions

t-SNE is an unsupervised method of dimensionality reduction. It provided us with 3D visualization of the state transitions for different windows. We concluded from these plots that the states changed frequently for smaller windows with time. We gathered the idea from the visualization that the state changes are frequent for smaller windows, but in the absence of GTs there is no way of finding the number of the times this transition was to the same state. Furthermore, in the absence of any ground truth (GT), there is no way of knowing the number of states captured for different window lengths.

In this study we applied the method on DMN captured from resting-state data, however, we believe that in future technique can be applied simultaneously on number of different networks to compare the possible transitions between different networks. In addition, the studies may identify the number of states in SWC results of different windows by using some clustering algorithm, and then apply t-SNE to compare the transitions to/from same state.

3.3.6 Conclusion

Application of dimensionality reduction technique, t-SNE, provided a novel way of visualizing the state transitions of the FC networks for different window lengths. To the best of author's knowledge this is the first time the comparison of state transitions for various window lengths is done visually. The results clearly illustrated the dependence of state transitions on the length of the window. The two studies in this chapter identified the need to evaluate the performance of the SWC that led us to do the performance evaluation of the SWC in Chapters 4 and 5.

CHAPTER IV

EVALUATION OF SLIDING WINDOW CORRELATION PERFORMANCE FOR CHARACTERIZING DYNAMIC FUNCTIONAL CONNECTIVITY AND BRAIN STATES

Our initial analysis of the dynamic functional connectivity (dFC) using the sliding window correlation (SWC) (Chapter 3) identified the impact of window size on the results, both in rodents and humans. The window size and other SWC parameters are not standardized since there is no "gold standard" for comparison. As a result, evaluating the performance of the SWC in typical resting-state data is challenging. The study in this chapter (published in [80]) used simulated networks (SNs) with known transitions to examine the effects of parameters such as window length, window offset, noise, and filtering on the SWC performance. The SWC time course was calculated for all node pairs of each SN and then clustered using the k-means algorithm to determine how resulting brain states match known configurations and transitions in the SNs. The outcomes showed that the detection of state transitions and durations in the SWC is most strongly influenced by the window length and offset, followed by noise and filtering parameters. Overall, the SWC gave poor estimates of correlation for each brain state. Clustering based on the SWC time course did not reliably reflect the underlying state transitions unless the window length was comparable to the state duration, highlighting the need for new adaptive window analysis techniques.

4.1 Motivation

The SWC is the simplest and most commonly used method for dynamic FC analysis and most of the dFC studies use it at some point [78, 14, 43, 32, 15, 36, 42, 91, 103].

Despite the popularity of the SWC, results are strongly dependent on window length [77, 36, 42, 103] and the ideal values for this and other parameters for the dFC analysis remain unknown. A nice but simplified examination of the relationship between the minimum window length and the frequency components of the signals has been presented [53]. Another study used windows of different sizes on resting state and sleep data and reported that short epochs can be used effectively for dFC analysis [103]. However, no study has convincingly identified the best window length for dFC analysis. Furthermore, since these brain networks change states at random times, using the same window over the entire rsfMRI scan may not be the optimum method to capture the true dynamic configurations of these networks. The effect of window length, offset, and other parameters has not been systematically examined in realistic data, and a recent study that looked at the effect of window length on the correlation between the BOLD signal and simultaneously-acquired local field potentials found that the optimal window length is somewhat ambiguous [92].

After the SWC is performed pairwise for the brain areas of interest, clustering is often used to find the number of 'states' that occur over the length of the scan, and the times at which transitions occur [36, 2, 20, 79]. The most commonly used method for clustering SWC results is based on the k-means algorithm [36, 2, 20, 79]. The accuracy of the clustering depends on the clustering algorithm and the ability of the SWC to resolve transitions of interest, emphasizing the need to evaluate the SWC parameters.

The biggest obstacle in identifying the best approach to the SWC and clustering for dFC analysis is that there is no ground truth (GT) in standard rsfMRI data, since the actual network dynamics, number of states, and state transitions are all unknown. This study circumvents this problem by using simulated networks (SNs) with known transition points created from real rsfMRI data. We evaluated the SWC algorithm and the effects of window size, window shift, noise, and filtering on SWC

results, and on the correct identification of state transitions and durations obtained from these results using k-means clustering. As expected, window size and offset had a substantial impact on the accuracy of the results, followed by the impact of noise and filtering. These findings motivate further work on methods that can dynamically adapt the length of the window during the analysis or the formulation of an algorithm which can more accurately detect the state transition points.

4.2 Material and Methods

4.2.1 Data and Preprocessing

We used rsfMRI scans of nine healthy human subjects (four females, ages: 21-57 years, downloaded from Nathan Klein Institute's Enhanced Rockland dataset of 1000 Functional Connectome Project ($http://www.nitrc.org/projects/fcon_1000/$). The scans were done on SIEMENS MAGNETOM TrioTim syngo MR B17 scanner. The scanning parameters were: TR = 645 msec, voxel size = 3mm isotropic, duration = 10 minutes, TE = 30 msec, Slices = 40, Multi-band accel. Factor = 4, time points = 900. Each scan contained 900 volumes and the intial 10 volumes of each scan were discarded to compensate for transient scanner instability. All preprocessing was done in statistical paramentric mapping (SPM 12, http://www.fil.ion.ucl.ac.uk/spm/. Preprocessing included motion correction, co-registration of the functional images with the anatomical image, segmentation, normalization, and smoothing. Default parameter values from SPM12 were used during preprocessing but smoothing was done using a Gaussian kernel of size 8 and for normalization a voxel size of 3x3x3 was chosen. The images were co-registered to the AAL atlas [95] using nearest neighbor interpolation without any warping. After preprocessing, five functional networks (Dorsal DMN, Ventral DMN, Anterior-salience, Visuospatial, and Sensorimotor) were extracted using the masks from the Stanford's functional imaging in neuropsychiatric disorders (FIND, http://findlab.stanford.edu/home.html) lab [84] for all subjects.

4.2.2 Regions-of-interest (ROIs) Time Series

For each subject, seven, non-overlapping, three-dimensional regions-of-interest (ROIs) consisting of 3x3x3 voxels were chosen from each of the above mentioned five networks (Dorsal DMN, Ventral DMN, Anterior-salience, Visuospatial, and Sensorimotor). Maps of the five functional networks (taken from Supplementary data of [84]) along with the locations of the ROIs selected for the current study (arrows) are given in Figure 13. Each ROI time series was formed by extracting the intensities of the voxels in the ROI and then computing their mean at each time point. These ROIs were used to create SNs as described in the next section. The averaged time series of each ROI was extracted and bandpass filtered (0.016-0.08 Hz, order 20 FIR) before the formation of the SNs.

4.2.3 Sliding Window Correlation of Actual Resting-state Networks

The main goal of this study was to analyze the performance of the SWC with variable parameters using SNs with known timing formed from real rsfMRI data. However, before starting this analysis we computed the pairwise SWC of the time series of the five actual networks (Dorsal DMN, Ventral DMN, Anterior-salience, Visuospatial, and Sensorimotor) using the same window sizes as the ones used for the SNs (discussed in detail in Section 4.2.4). The purpose was to compare the SWC of the actual data with the results of previous studies [42, 37, 103] and to determine how the abrupt intensity changes (outliers) introduced in our SNs due to state transitions (explained in Section 4.2.4) might influence results of the SWC.

4.2.4 Simulated Networks and Sliding Window Correlation

To form a simulated network (SN), sevenregion of interests (ROIs) from one of the above mentioned rsfMRI networks were used. A portion of the time courses for these ROIs was taken and used as the time courses for the seven nodes of the SN until the first state transition point t_1. At t_1, a portion of the time courses from the seven

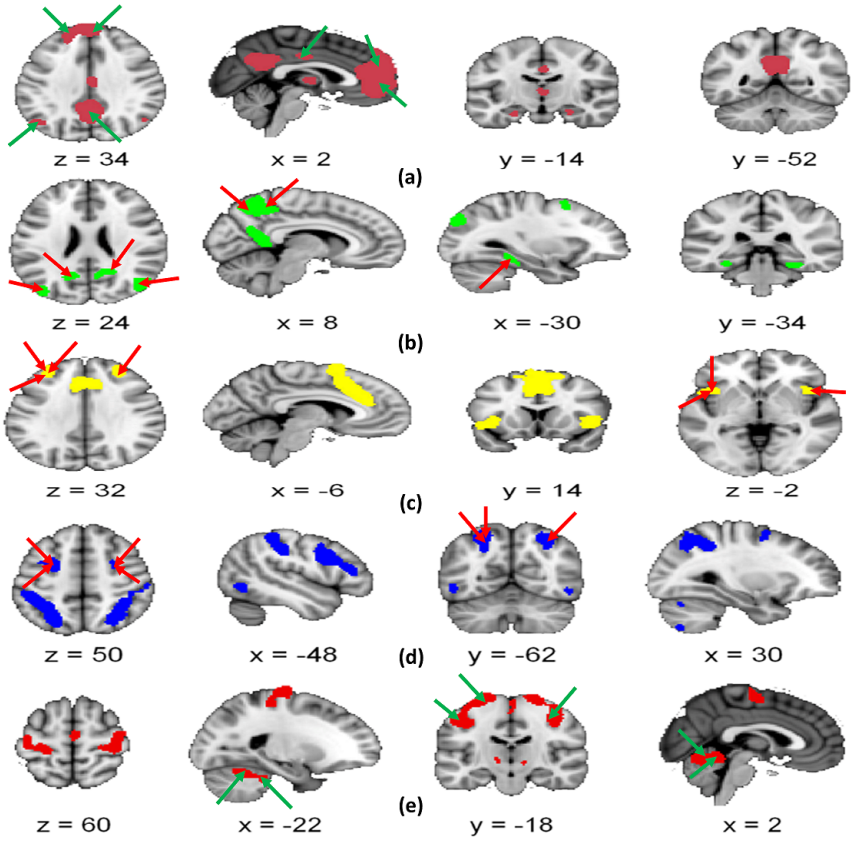

Figure 13: Masks of the functional networks taken from supplementary data of functional imaging in neuropsychiatric disorders (FIND) lab. (a) Dorsal DMN network. (b) Ventral DMN network. (c) Anterior Salience network (d) Visuospatial network (e) Sensorimotor network. The colored regions in any of these networks are the regions-of-interests (ROIs) defined by the FIND lab and their sizes are different. However, in this study the ROIs are defined as non-overlapping 3x3x3 voxels extracted from these bigger ROIs. The ROIs in this study are pointed to by the red and green arrows. The size of the ROIs defined by FIND lab is generally greater than 3x3x3 voxels so more than one non-overlapping ROIs (of size 3x3x3) could be extracted from the same ROIs of the original functional networks.

ROIs of a different network was added to the SN to create a new state lasting from t_1 to t_2. This process was repeated until the desired length of 890 time points was obtained. For example, if we chose the nodes from ventral DMN from t_1 to t_2, then the nodes from t_2 to t_3 were from another network e.g. sensorimotor network of the same subject, and this process continued till we reached the last interval from t_{n-1} to t_n. Formation of the SNs in such a manner incorporated real rsfMRI data but gave us control over the time at which the SNs changed states (switched from one resting-state functional network to another) since we chose the transition times t_1 to t_n. It should be noted here that our SNs were formed from five resting-state networks but some of them had more than five transitions which means the data from the same resting-state network would be taken more than once in formation of these SNs. However, apart from one SN (QPeriodicSN explained later in this section) there is no repetition of data. For example, if the data from ventral DMN is taken for the durations t_{x-1} to t_x and t_{y-1} to t_y (x and y are integers) for a SN then it would be from two entirely different non-overlapping intervals of the ventral DMN. This step insured that no two parts of a SN had exactly the same correlation values between the node pairs (except for QPeriodicSN).

The configuration of a SN between any two consecutive transition points is referred to as one 'state' of that SN since it was formed by data from one FC network (state) of original resting-state scans. All the states of a SN (except QPeriodicSN) have different correlation values between the node pairs but more than one of these states may be from the same resting-state network. By changing the transition points we were able to form five different SNs. Three of these SNs were formed with state transitions at equal intervals (state transition at every 50 TRs for '50SN', at every 100 TRs for '100SN', and at every 200 TRs for '200SN', TR = 645 msec). Real resting-state networks are unlikely to change configurations at equal intervals but the analysis with these SNs allowed us to explore the best choice of the sliding window parameters for

the ideal case of regularly changing networks. However, we also formed two SNs where the state transitions occurred at random intervals to evaluate the performance of the SWC in more realistic scenario. In the first randomly changing network, we used quasi periodicity by repeating three states at random points during the formation of the SN (QPeriodicSN). The second randomly changing network (RandSN) had completely random state change points with state durations from 20 TRs ($\approx$ 13 seconds) to 130 TRs ($\approx$ 84 seconds).The formation of these five SNs allowed us to examine the sensitivity of the SWC to regular states of different lengths, and randomly changing states with or without quasi periodicity. The state durations for the SNs ranged from $\approx$ 13 seconds to $\approx$ 129 seconds, while the window lengths used were $\approx$ 17, 33, 65 and 129 seconds (25 TRs, 50 TRs, 100 TRs, and 200 TRs, TR = 645 msec). All of these window lengths were within the sizes commonly reported in the literature that vary from from 8 to 240 seconds [14, 43, 32, 15, 42, 91, 78, 15, 45, 103]. In their papers [53] and [79] explored the relationship of frequency components in the correlating signals and window length. [53] established the mathematical relationship between the window length and the minimum frequency (f_{min}) of the correlating time series. By using simple sinusoids [53] reported that the minimum window length should at least be equal to $\frac{1}{f_{min}}$ in order to avoid spurious fluctuations arising due to the SWC algorithm itself. Using the same guidelines [79] explored the effect of two frequencies on the the SWC results.

Overall five simulated networks (SN)s were formed from each subject's data: Three with equal duration states and two with randomly changing states. The equal duration SNs had 18 (50SN), 9 (100SN), and 5 (200SN) distinct states of FC. QPeriodicSN had a total of 15 FC states, of which three were repeated at random time points, while RandSN had 10 distinct FC states changing at random times. We computed SWC for all of these SNs for different window lengths and other parameters to determine the best combination of parameters for SWC as a dynamic FC analysis method. Detailed

results from the SNs created from one randomly selected subjects data along with the mean results of all SNs created from all nine subjects are reported in this study.

4.2.5 Ground Truth

State changes in the SNs occurred at times t_1, t_2, t_3., t_{n-1}, and t_n, when ROIs were taken from a different resting-state network. This resulted in a change of pairwise correlations between all of of the nodes in a SN at each transition point. To examine the influence of various sliding window correlation (SWC) parameters on its sensitivity to network transitions, actual correlations between the nodes of the SNs were computed for the durations for the which the state remained the same. The actual correlation of a node pair for any state was correlation coefficient of the node pair time series for the duration of the state. This correlation value was same for the whole state duration and can be replicated. For example, if the correlation coefficient between two time series was 0.5 for the state between t_1 and t_2 then 0.5 would be replicated from t_1 to t_2 for representation purposes.The computation of correlation in this manner is same as the computation of stationary correlation with length of the correlating time series equal to the state duration instead of the whole scan length as in the case of stationary correlation. The mean of the resulting actual correlations of an SN was called the 'ground truth (GT)' for that SN. Because there were n= 7 nodes in each SN, overall there were n(n-1)/2= 21, distinct correlations for each state, and the GT was the mean of these correlations. Figure 14. shows the GT for 100SN, QPeriodicSN, and RandSN. Discontinuities in the Figure 14 are the state change points, which will be referred as 'state transition points' in this chapter, and the duration between two consecutive discontinuities corresponds to one state of the SN. It is also important to note that the GTs are not the actual correlation time series between the node pairs, but are their means plotted to clearly show the state transitions and durations.

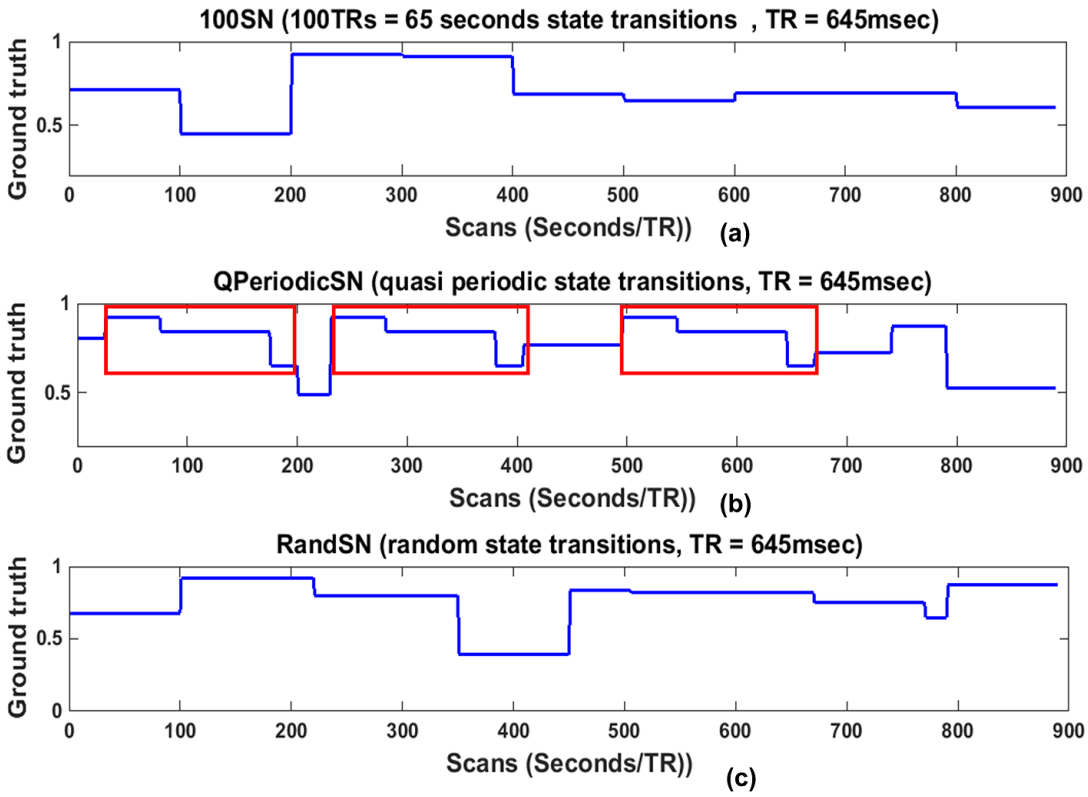

Figure 14: Ground truths (GTs) for (a) 100SN, (b) QPeriodicSN, and (c) RandSN. 100SN has state transitions at every 100 TRs (65 seconds), QPeriodicSN has quasi periodic states (red rectangles) repeated at random times, and RandSN has all the states transitions at random times. Each SN has seven nodes and ground truth for any SN is the mean of actual correlations of all of its node pairs. .

4.2.6 Sliding Window Correlation Parameters

Four parameters were varied to explore their influence on the sensitivity of the SWC and subsequent clustering. For all parameter values, the SWC was calculated pairwise for all nodes of each SN.

1. Window length: [24] reported that resting-state networks exhibit long-term stability and that the similarity of within-subject whole brain connectivity is a function of window duration. In various dynamic FC studies based on the SWC, the window length ranges from 8 to 240 seconds [14, 43, 42, 2]. We examined windows of 25, 50, 100, and 200 TRs ($\approx$ 17, 33, 65 and 129 seconds). All the window sizes were within the limits reported in the literature [14, 43, 42, 2, 45, 103].

2. Signal-to-noise ratio (SNR): The signal-to-noise ratio (SNR) of resting-state functional MRI (rsfMRI)data depends on a number of factors and can include structured noise due to motion or physiological cycles [44, 28, 9]. In order to explicitly examine the influence of random noise on the identification of states using the SWC, additive white Gaussian noise (AWGN) (using awgn() in MATLAB) was added to the time series of each SN at levels of 10 dB and 20 dB. We also examined the effect of reduced SNR by selecting random single voxels from random slices as nodes of our SNs instead of 3x3x3 voxels ROIs.

3. Window offset: Typical window offsets used in previous studies range from 1 to 20 seconds (which covers the range from a single TR step to 50 % of the window length) [15, 42, 45, 81]. The majority of this study used a window offset of one TR (645 msec), but the effects of offsets equal to one-fourth or one-half of the window lengths were also explored.

4. Filtering: Typical rsfMRI studies bandpass filter (0.01-0.08 Hz or 0.01-0.1 Hz) the time series in order to reduce the effects of noise. A recent study [53]

has shown that the frequency components of the signal and the window size interact to impact final SWC results. It showed that the spurious correlations of the SWC results are reduced when the size of the window is greater than $\frac{1}{f_{min}}$ (f_{min} = minimum frequency). We explored this relationship by varying the minimum frequency content of the rsfMRI signal. For this purpose we used highpass filtered (> 0.016 Hz, > 0.05 Hz and > 0.08 Hz) time series to form SNs, corresponding to minimum window lengths of 62.5, 20, and 12.5 seconds respectively.

4.2.7 Clustering

One of the major goals of this study was to determine how well the clustering based on the SWC performs at identifying network state durations and transitions. In previous dynamic FC studies, k-means clustering was used on SWC results to extract states of FC [50, 2, 20, 81]. We also applied k-means clustering to the SWC results to determine whether state transitions and durations were identified correctly. For this purpose, the SWC results were grouped into clusters called 'Cstates' and the results were examined to determine how well the Cstates coincided with the known state transitions and durations shown in the GTs (Figure 14.). In order to evaluate the performance of k-means clustering alone for state identification, we clustered the raw time courses for the seven nodes of each simulated network (SN) in addition to clustering SWC results. Silhouette criteria [75] was used to determine the best number of clusters for each data set. The number of clusters was varied from two to twelve and the overall mean of silhouettes was computed [75]. We selected the number of clusters (raw SNs) and Cstates (SWC results) for each case when this mean became constant or started to decrease. In general, the number of Cstates for all windows and all SNs was less than or equal to the actual number of states in the SN (10 for RandSN, 15 for QPeriodicSN, 18 for 50SN, 9 for 100SN, and 5 for 200SN),

resulting in the assignment of more than one state to the same Cstate. To determine the similarity of states assigned to the same Cstate, the Euclidean distance between them was computed.

4.3 Results

4.3.1 Sliding Window Correlation of Actual ROI Time Series

We computed pairwise SWC of the actual ROI (3x3x3 voxels used in this study) time series of the five functional networks (Dorsal DMN, Ventral DMN, Anterior-salience, Visuospatial, and Sensorimotor) for all windows. Figure 15. shows the results of the pairwise SWC along with the stationary correlations (black horizontal lines). The node pairs were selected at random from three of the five networks (Dorsal DMN, Ventral DMN, and Sensorimotor Network).

It can be observed that for all cases the SWC varies around the actual correlation but the extent of variability is largest for the smallest window (25 TRs, red in (a)) and decreases as the window size increases towards right. All the plots show a similar trend and are in accordance with the results reported in [42, 103].

4.3.2 Effects of window length

Four different window sizes (25, 50, 100, and 200 TRs, or 17, 33, 65 and 129 seconds respectively) were employed to determine the effect of window length on the sensitivity to actual correlations, state transitions, and state durations in the SNs. For this portion of the study, the window offset was kept constant at one repetition time (TR) (645 msecs), the window shape was rectangular, and all time courses were bandpass filtered (0.016-0.08 Hz). The SWC for all pairs of nodes for all SNs exhibited variability over time. Greater variability was observed when shorter windows were used, in accordance with previous studies [42, 103, 37]. Figure 16. shows the actual correlations (black lines) and the SWC for one node pair in 100SN (row 1), QPeriodicSN (row 2), and RandSN (row 3) for all window lengths.

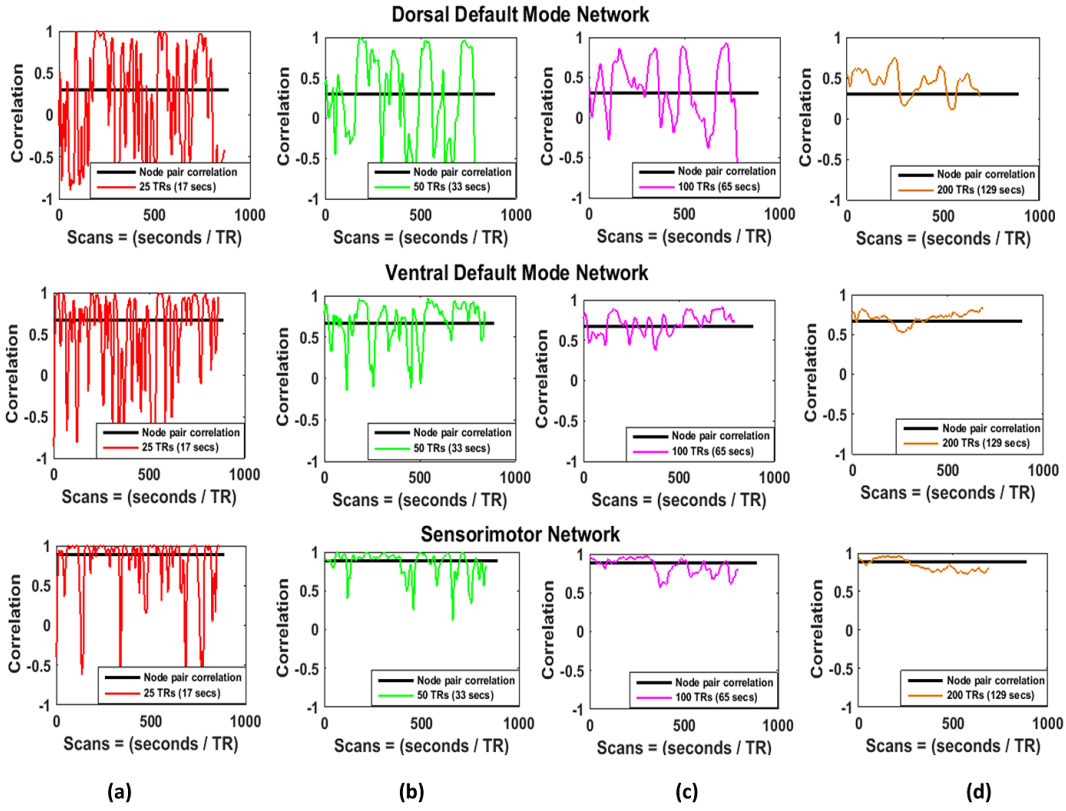

Figure 15: Stationary and sliding window correlations of three node pairs (selected at random) from three different real resting-state networks. Stationary correlations of the node pairs are shown by black horizontal lines. The size of the window increases from left to right. The SWC fluctuates around the stationary correlation and these fluctuations are largest for smallest window (a) and decrease as the window size increases towards the right.

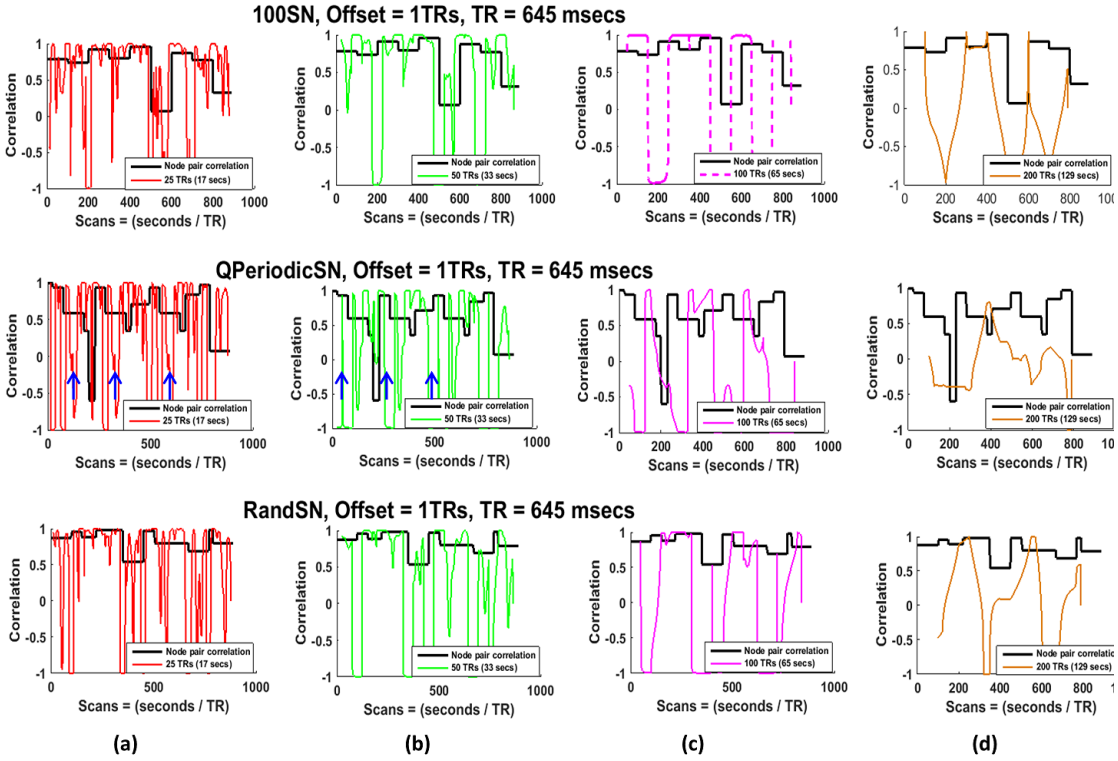

Figure 16: Actual correlations and SWCs for one node pair in 100SN (row 1), QPeriodicSN (row 2), and RandSN (row 3). The SWC is plotted for windows of 25 TRs, 50 TRs, 100 TRs, and 200 TRs ($\approx$ 17, 33, 65 and 129 seconds). The window offset is one TR and filtered (0.016-0.08Hz) time series are used. The actual correlation between the node pair is plotted in black. Smaller windows (red, green) result in more variable correlation time series. The large amount of variability indicates smaller windows could capture short-lived correlations but some of these variations may be due to the spurious fluctuations introduced due to the small size of the window. Smaller windows are also able to capture the quasi periodic pattern of QPeriodicSN indicated by the blue arrows but this pattern is lost with increasing window size. The transitions in the SWC results occur at an interval of 65 seconds (100 TRs) for 100SN when the state duration and window size are same (pink dashed) which shows that SWC is good in identifying the transition of states when window size and state duration are well matched.

A few observations can be made:

1. None of the sliding window correlation (SWC) time courses accurately capture the different states of correlation for the SNs. The amount of variability in the SWC time course is typically higher than the variation across different states of correlation. Large changes in the SWC sometimes correspond to transitions between states due to the abrupt changes that occur at the transition points, but often exist in the absence of state transitions (especially in smaller windows). SWC results vary widely between -1 and 1 for almost all windows, though these variations are more rapid for smaller windows (red and green) compared to larger ones (pink and brown).

2. Smaller window sizes can capture short-lived variations in correlation more accurately than longer windows, as can be seen from the rapidly fluctuating plots of the 25 TRs window (red) and 50 TRs window (green), as compared to the longer windows (pink and brown). However, a portion of these fluctuations may arise since smaller windows also create more high-amplitude variations and spurious fluctuations [53, 79] that do not correspond to state transitions.

3. For the SNs with state transitions at equal intervals, the SWC is sensitive to the state transitions if the window size is equal to the state duration, although the actual correlation values are not always captured. 100SN is shown as an example in Figure 16 (row 1, (c)) and similar results were obtained for 50SN and 200SN. These results show the inability of the SWC to deal with abrupt amplitude changes (outliers) in the intensity levels of correlating signals [55].

4. For QPeriodicSN a quasi periodic pattern was observed in the SWC results for smaller windows (blue arrows in Figure 16., row 2 (a) and (b)) but this pattern was lost for larger windows.

5. For the simulated network (SN) with randomly changing state transitions (Figure 16, row 3), no window size consistently identifies transitions at the state change points.

Stationary correlation between the actual and SWC of all node pairs for all windows was also computed. The SWC was not strongly correlated with the actual correlation since there were large changes due to sharp state change points, however, the smaller windows gave better correlation values regardless of the SN, as shown in Figure 17. This may be because smaller windows capture dynamics of correlation at smaller scales compared to larger windows. A better reflection of the actual correlation was also obtained for long-lasting states (200SN).

4.3.2.1 Dependence of State Identification on Window Length

We clustered the actual (raw) SNs in five Cstates based on Silhouette criteria to determine whether the k-means algorithm would be able to identify the state transitions and durations in the raw data. The results of this clustering for 100SN, QPeriodicSN, and RandSN are given in Figure 18. The blue lines in the plots show the ground truths (GTs) of the SNs with state transition points at the discontinuities. Circular colored markers on these lines indicate the Cstate in which the SN resides at that particular time. If all circles between two state transition points are in the same color, then the SN remained in one Cstate during that time. A change of marker color at a state transition point indicates correct detection of the state transition. Good state transition and duration identification implies that the color should change at the state transition points but should remain the same between any two adjacent state transition points. It can be observed from the figure that k-means perfectly identified the state transitions and durations for the raw SNs. The repeated states of QPeriodicSN (red rectangles) are assigned to the same Cstates, as expected.

To examine how the window length impacts the identification of *brain states*, the

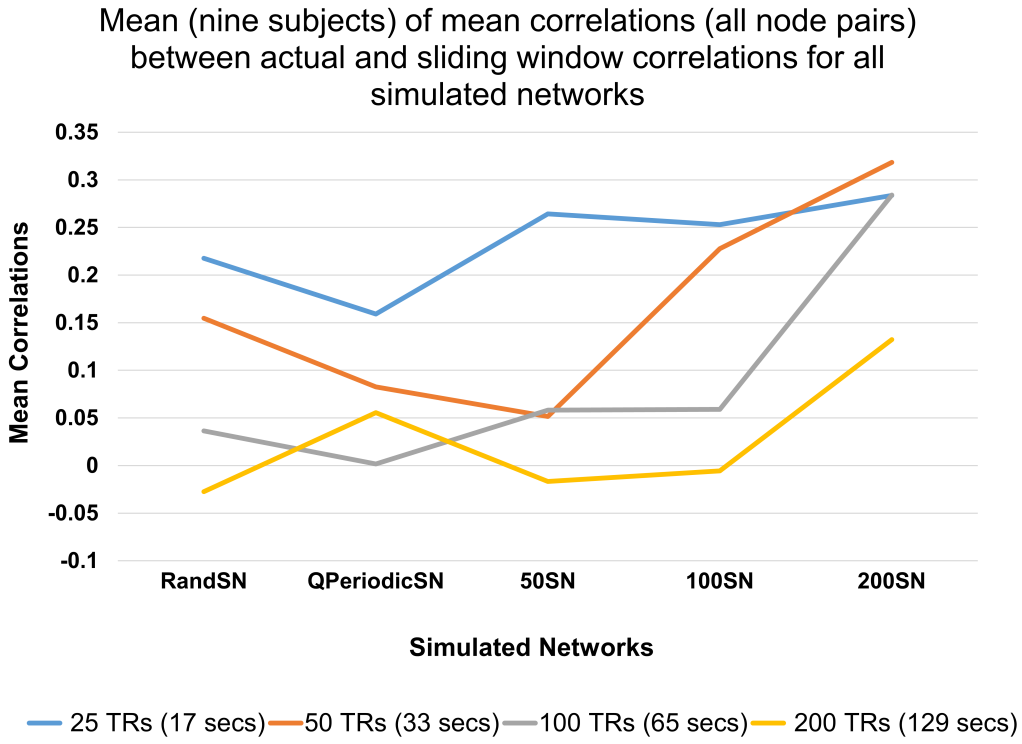

Figure 17: Mean (of mean correlations of all node pairs) over all subjects. The overall mean is not very high because the SWC is very sensitive to abrupt transitions between the states. However, smaller windows give SWC results that are more similar to the actual correlation values compared to larger windows.

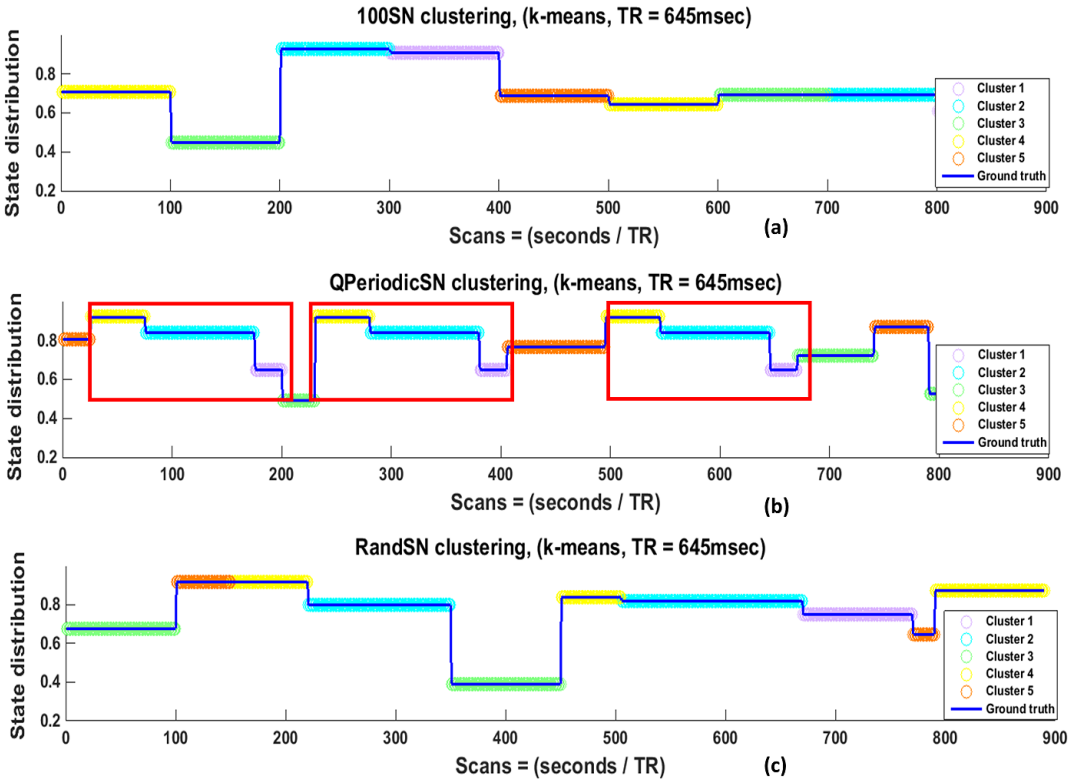

Figure 18: Clustering of raw SNs (100SN in (a), QPeriodicSN in (b), and RandSN in (c)) using k-means. The best number of clusters was identified using Silhouette criteria. Discontinuities in the blue lines indicate state transition points, while the colors of the overlaid circles represent the Cstate at each time point that was assigned by the clustering algorithm (k-means). When the circles between two adjacent state transition points remain the same color, it indicates that the state is correctly identified to be in single Cstate and a color change at state transition points indicates that the state transitions are correctly identified. The division of the raw signals gives perfect state transitions and state durations. The repeated states of QPeriodicSN (red rectangles) are assigned to the same Cstates, as expected.

SWC results were divided into clusters (Cstates) using the k-means algorithm. Figures 19-21 show the clustering results for different SNs and different window lengths.

For 100SN, it can be seen in Figure 19 (a) that the Cstate changes at almost every discontinuity, indicating that a state transition has been correctly identified even when the window size is only about one-fourth of the state duration. Similar findings were observed for windows of 50 TRs and 100 TRs ((b) and (c)). These results show that the state transitions can be correctly identified when the window size is proportional to the state duration (one-fourth, one-half, or equal) for the SNs that change state at equal intervals. However, especially for shorter windows, it is common for a single actual state to be assigned to multiple Cstates, artificially increasing the number of observed transitions. Similar observations were made for all SNs in all the subjects.

In 100SN the changes in Cstate consistently occurred at known state transitions for all window lengths, but Cstates changed between true transitions for window lengths that were smaller than the state duration (25 and 50 TRs in Figure 19.). The time period of a state duration is assigned to more than one Cstate (typically two for the 50 TR window and three or more for the 25 TR window), while for the 100 TR window it is typically assigned to a single Cstate. These findings were similar for other regular networks and indicate the failure of the SWC to correctly identify the state for the whole of its duration if the window size is not at least as long as the state duration interval. Reducing the window size to one-half of the state duration resulted in each state typically being divided into two Cstates, as can be seen from Figure 19 (b). Similar results can be observed for 50SN and 200SN for the same subject in Supplementary figures 14 and 15 respectively. These observations were consistent across all window sizes and in all the regulary changing simulated networks (SNs) of all the subjects.The number of correct state transitions and state duration assignments for all SNs were assessed by computing the mean for all subjects in Tables 1 and 2. These results are explained further in the next section.

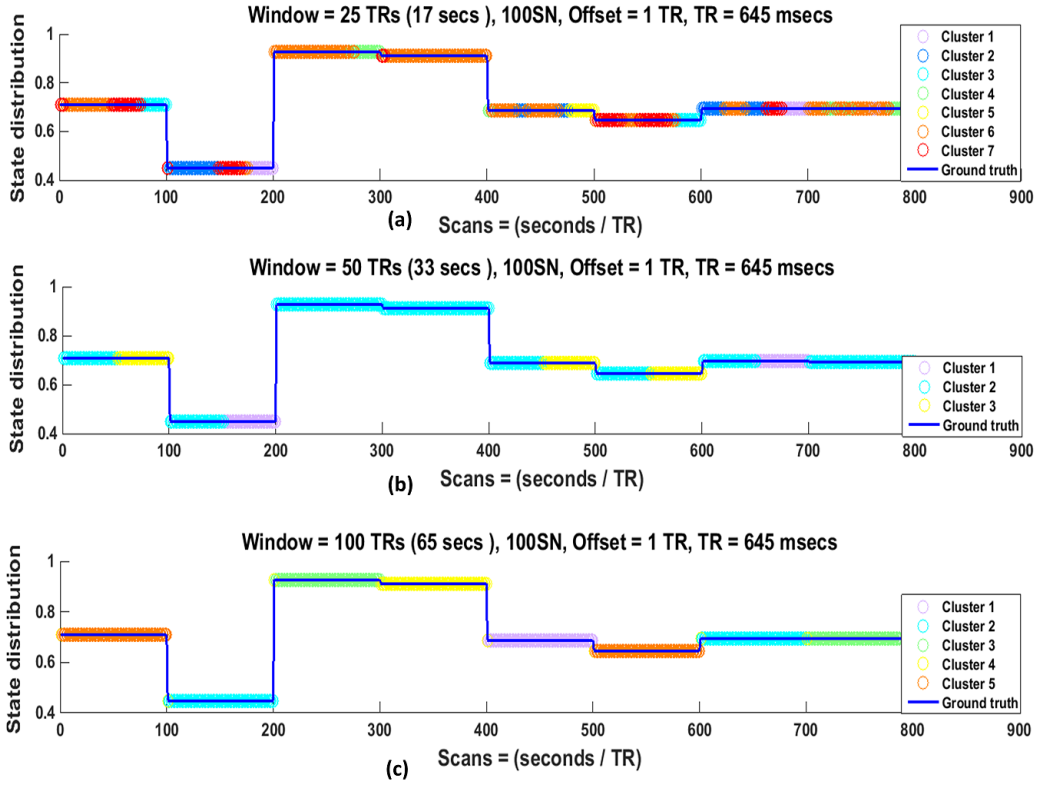

Figure 19: State distribution of SWC results for 100SN for one subject. (a) State distribution for a 25 TR window (seven clusters or Cstates). Here state transitions are identified accurately but the number of transitions is much greater than the number of actual state transitions. State durations are not identified correctly in this case. (b) State distribution for a 50 TR window (three clusters or Cstates). Here state transitions are identified accurately but again the number of transitions is greater than the actual number of state transitions. State durations are not identified correctly, with most actual states split evenly into two Cstates. (c) State distribution when the window size is equal to the state duration of 100 TRs. The state transitions are correctly identified as seen by the change of color at the discontinuities. Furthermore, the state durations are also identified reliably as shown by consistent assignment of each actual state to a single Cstate.

Since real resting-state networks in the brain would not be expected to exhibit regularly spaced state transitions, we also explored the effect of window size on state transitions and state durations in QPeriodicSN and RandSN. QPeriodicSN was formed based on the identification of quasi periodic patterns of FC networks in rats and humans [61]. [61] reported that the same patterns of FC dynamics occur at random times during the scan. We presented similar quasi periodicity by repeating three states (shown by red rectangles in Figure 14) at random times in QPeriodicSN. Figure 20 shows the state distribution of QPeriodicSN for 25 TRs, 50 TRs, and 100 TRs windows.

It can be observed from the color changes at the state transition points that the 25 TRs window was able to identify state transitions better than the larger windows (50 TRs and 100 TRs). Smaller windows (25 TRs and 50 TRs) also identified the quasi periodicity of the SN as shown by almost identical Cstates assignments inside green dotted rectangles. However, most of the actual states were assigned to multiple Cstates for all windows, indicating that the state durations are not correctly identified. An interesting observation is that it appears that the state durations are dominated more by the size of the window than by the actual transitions of the SN, as can be seen by the width of the black rectangles that are almost equal to window sizes.

Figure 21 illustrates the state distribution of the sliding window correlation (SWC) results of RandSN for 25 TRs, 50 TRs, and 100 TRs windows. The results shown here are similar to the results of QPeriodicSN, in which each state is assigned to more than one Cstate, and state assignment is dominated by the window size, especially for smaller windows (25 TRs and 50 TRs). Figures 8 and 9 clearly identify the inefficiency of the SWC in recognizing the state transitions and durations for randomly changing networks.

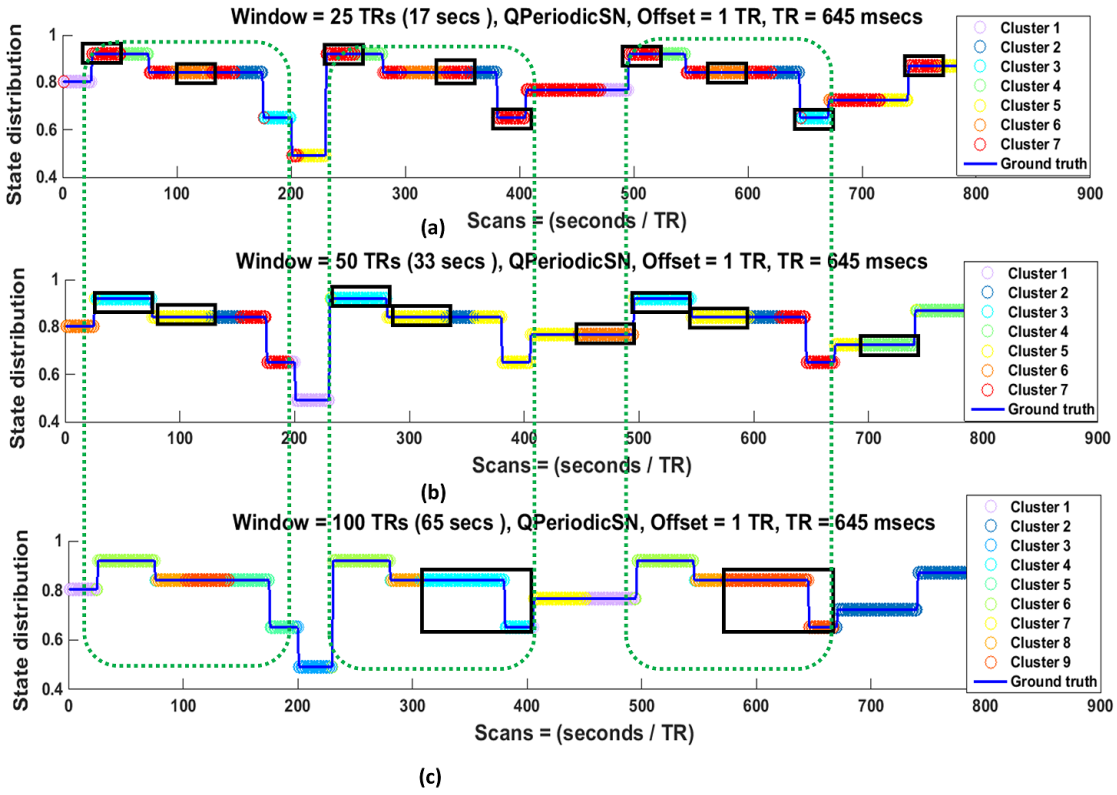

Figure 20: State distribution of QPeriodicSN for 25 TRs (a), 50 TRs (b), and 100 TRs (c) windows. The 25TRs window is able to capture the state transitions accurately than the larger windows in (a) but the number of overall state transitions in this case is also larger than for the 50TRs or 100TRs windows in (b) and (c). The quasi periodic pattern of the SN is identified in 25 TRs and 50 TRs windows as shown by the same color distributions inside the green dotted rectangles. Furthermore, the state identification is dominated by the size of the window since most of the state durations are almost equal to the window size as shown by black rectangles.

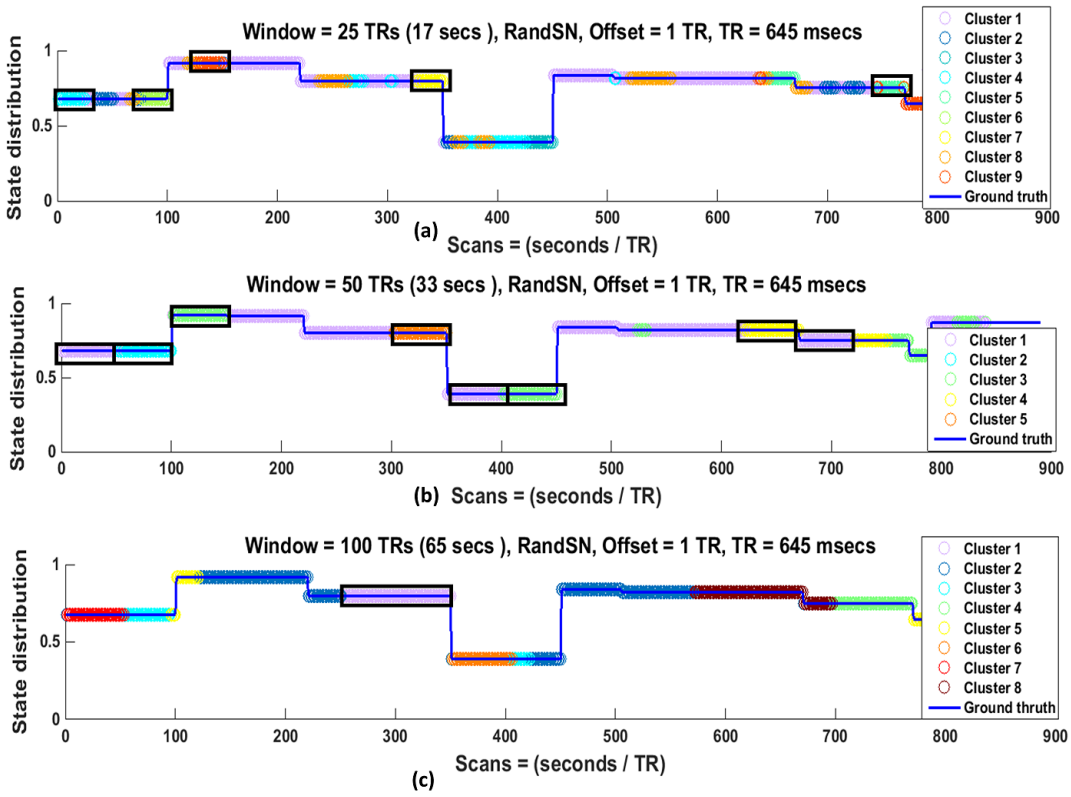

Figure 21: State distribution of RandSN for 25TRs (a), 50TRs (b), and 100 TRs (c) windows. None of the window correctly identifies the state transitions and durations. For smaller windows ((a) and (b)), identified state durations are mostly equal to the size of the window.

4.3.2.2 Correct State Duration and Transition Identification

Clustering based on the SWC performed well for identifying state transitions and durations for certain combinations of SNs and window sizes but not for other combinations. In order to quantitatively analyze the SWC results, mean percentages of full state identifications and number of correct state transitions for each SN and each window size were calculated for all nine subjects. The Cstate transitions were defined by a change of cluster assignment at any time, and the identification was said to be correct if the change occurred at a state transition point. For example, if there are total 'm' state transitions in a SN and 'n' of these are coinciding with the Cstate transitions then the correct transition percentage would be ($\frac{n}{m}$*100).

A state was defined as fully identified if it remained in the same Cstate for more than 98% of its duration. Because the number of Cstates was less than or equal to number of states in the SNs (15 for QPeriodicSN, 10 for RandSN, 18 for 50SN, 9 for 100SN, and 5 for 200SN), even in the case of successful full state identification, more than one of the states would be assigned to same Cstate. To examine how well the Cstates reflected the underlying patterns of correlation, the distance between the states assigned to a single Cstate was calculated and compared across Cstates. The mean percentages of full state identification and the mean percentages of closest states assigned to the same Cstate are given in Table 1. As expected from figures 19-21, poor full state identification was achieved with small window sizes. For a 25 TRs window the percentage of full state durations assigned to the same Cstates varied from 0% to 21%. This is not surprising given the large amount of variability observed in the SWC obtained with short windows. States were identified well ($>$ 99%) when the SN had transitions at equal intervals, and the window size was equal to the interval between transitions. The mean percentages of the closest states assigned to a Cstate was also high for 100SN and 200SN, but not for 50SN (50 TRs window) though the mean percentage of full state identification was high (99%) for this case too. This

low percentage may be due to sensitivity of the window to small correlation changes and presence of spurious fluctuations.

Table 1: Mean percentages of full state identifications for all SNs along with the mean percentages of the closest states that are assigned to the same cluster (Cstate, given in parentheses) for all nine subjects. For a specific window size, the maximum full state identification occurs for the SN with state durations equal to that window size (50 TRs window for 50SN, 100 TRs window for 100SN, and 200 TRs window for 200SN), shown in red. None of the windows provided good full state identification for the QPeriodicSN and RandSN. The number of actual states (15 for QPeriodicSN, 10 for RandSN, 18 for 50SN, 9 for 100SN, and 5 for 200SN) was greater than the number of Cstates (mean varying between three and seven), which means that in the case of full state identifications, more than one state would be assigned to the same Cstate. The numbers in the parenthesis next to the full state identification percentages show how many of the states, which were closest to each other, are assigned to a single Cstate.

Mean percentages of full state identification (mean percentages of closest states) for nine subjects for filtered (0.016-0.08 Hz) simulated networks.)					
Window size	RandSN	QPeriodicSN	50SN	100SN	200SN
25 TRs (17 seconds)	21 (97)	9 (94)	13 (58)	11 (40.7)	0 (0)
50 TRs (33 seconds)	50 (64)	58 (97)	99 (55)	21 (56)	25 (56)
100 TRs (65 seconds)	30 (50)	50 (75)	42 (66)	100 (85)	15 (44)
200 TRs (129 seconds)	69 (59)	65 (55)	44 (73)	39 (82)	(100) (97)

Table 1 gives the total number of state transitions along with the mean percentages of correct state transitions with respect to both the total detected state transitions and the actual state transitions (in the parenthesis) for all windows sizes and SNs. The total number of transitions was dependent on the window size as well as the actual number of states in a SN. QPeriodicSN and 50SN had largest number of state transitions (17 and 14) , and in general all the windows showed the largest number of transitions for these SNs (shown in red), but the largest (44) of them occurred for smallest window of 25 TRs. For any SN, the 25 TRs window captured the highest number of state transitions, some of which may be due to spurious fluctuations. The correct state transition percentages with respect to total and actual state transitions were maximum for a SN ((59,86) for 50SN, (57,86) for 100SN, and (48,72) for 200SN)

Table 2: Total state transitions along with the mean percentages of correct state transitions (with respect to total detected state transitions and actual state transitions given in the parentheses) are shown for all window sizes and SNs. The total number of transitions is dependent on the window size as well as the actual number of states in a SN. QPeriodicSN and 50SN have the most state transitions (14 and 17) and all the windows show the maximum number of transitions for these SNs but the largest of them occurs for smallest window of 25 TRs (row 3, column 3 and 4). Mean percentages of correct state transitions with respect to the total and actual state transitions are largest for an equal interval SN when the window size is equal to the state durations (red entries).

Mean percentages of full state identification (mean percentages of closest states) for nine subjects for filtered (0.016-0.08 Hz) simulated networks.)					
Window size	RandSN	QPeriodicSN	50SN	100SN	200SN
25 TRs (17 seconds)	39 (16, 68)	39 (32, 90)	44 (28, 73)	33 (19, 81)	42 (6, 64)
50 TRs (33 seconds)	15 (37, 63)	25 (40, 70)	25 (59, 86)	13(45, 74)	9.6 (27, 64)
100 TRs (65 seconds)	13 (17, 25)	18 (27, 33)	15 (12, 10)	12 (57, 86)	5.8 (44, 64)
200 TRs (129 seconds)	4.3 (15, 7)	7.1 (3, 2)	10 (0, 0)	6.8 (8, 6.9)	6 (48, 72)

when the window size was equal to the state duration in regularly changing SNs, as shown by green entries. These percentages were reasonably high when the window size was smaller than or equal to the state duration but dropped when window size became larger than the state duration. For both QPeriodicSN and RandSN, in the absence of any regularity, correct identification was observed for smaller windows and decreased with the increase in the length of the window. However, these percentages were higher for QPeriodicSN as a result of quasi-periodic patterns.

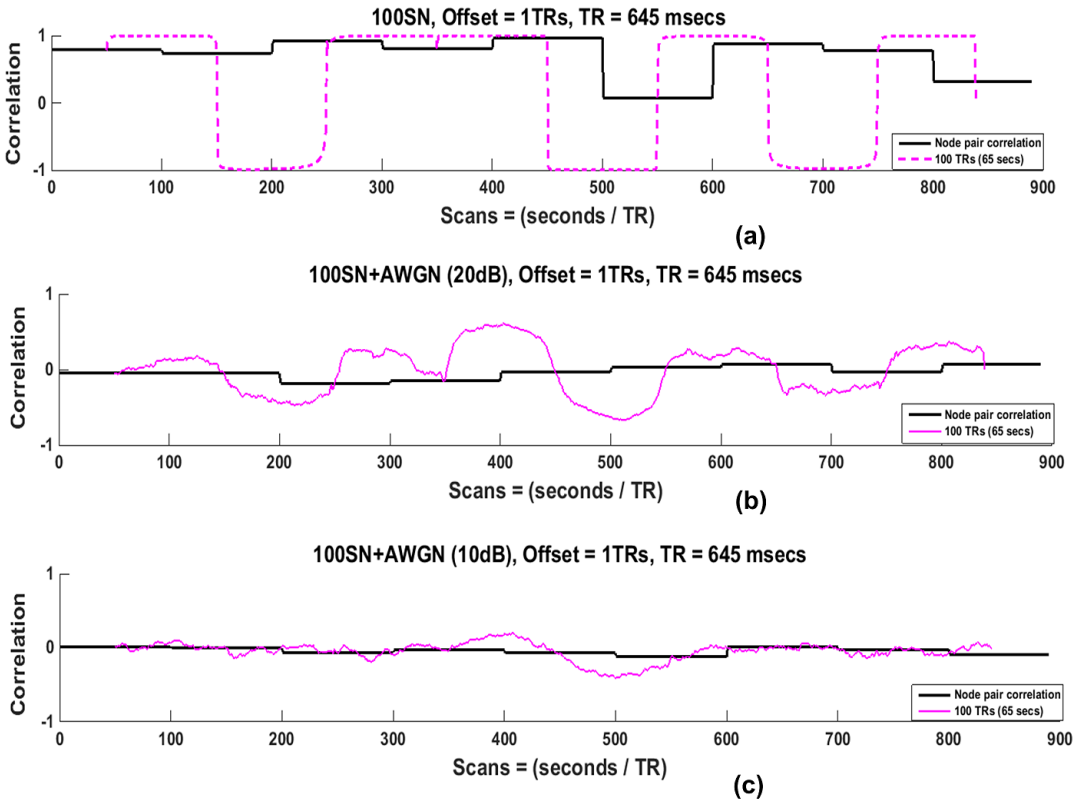

Figure 22: Actual correlation and SWC of one node pair (100SN for 100 TRs window) after addition of additive white Gaussian noise (AWGN) with an SNR of 20dB (b) and 10dB (c). Noise reduces the sharp transitions of the SWC results seen in (a). The identification of transition points becomes more difficult for small SNR (c) compared with large SNR (b).

4.3.3 Effects of Signal-to-noise Ratio (SNR)

Various types and levels of noise are present in actual resting-state scans. Filtering the data minimizes some of the noise sources but cannot eliminate them completely. In order to examine the influence of noise, we added random AWGN at levels of 10dB and 20dB to all SNs before performing the SWC. The SWC results of one node pair in 100SN for the 100 TRs window are shown in Figure 22. since this combination of state and window length performed best for the noise-free case. The addition of noise reduced the sharp state transitions of the SWC results. Smaller SNR (c) reduced the sharpness more than the larger SNR (b).

4.3.4 Effects of Window Offset

Up to this point all of the results were shown for a window offset of one TR (645 msec). Since some previous studies have used larger offsets [14, 15, 103, 45], we also explored the effect of larger offsets on the SWC and the resulting Cstates. When the 100 TRs window is applied to 100SN but with a window offset of one-fourth (25 TRs) or one-half (50 TRs) the window length, an additional transition occurring at approximately 25 TRs (50 TRs) after the transition at the state change point is introduced into the SWC time course as shown in Figure 23. (blue oval marker shows one of these additional transitions in each plot).

4.3.5 Effects of Filtering

A recent study showed that the SWC for two sinusoids approaches the steady state value only if the window size $\geq \frac{1}{f_{min}}$, where f_{min} is the minimum frequency of the correlating time series [53]. To determine if matching the lowest frequency in the time course of the signals to the window size impacts the calculation of the SWC and corresponding clustering in more complex data, we performed the same analysis on the SNs created using highpass filtered (> 0.016 Hz, > 0.05 Hz, and > 0.08 Hz) time series. Based on the findings of [53], windows of size greater than or equal to 62.5 secs (for $f_{min} = 0.016$ Hz), 20 secs (for $f_{min} = 0.05$ Hz), and 12.5 secs (for $f_{min} = 0.08$ Hz) would result in the SWC approaching the steady state values for our highpass filtered SNs. The SWC between the node pairs were computed and compared with the actual correlations for these highpass filtered SNs. The results for one node pair for 100SN are given in Figure 24.

We observed decrease in the SWC values for almost all of our windows when f_{min} was 0.08 Hz (row 3), but this reduction was more noticeable for larger windows and did not follow the steady state correlations shown by black lines. Furthermore, increasing the highpass cutoff also resulted in the loss of sharp transitions at the

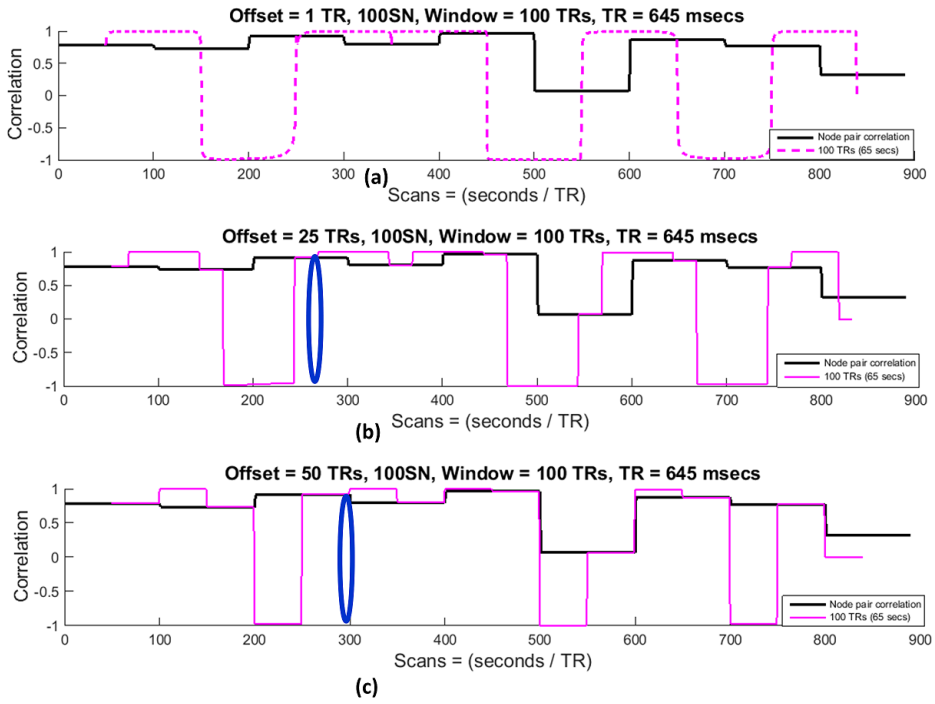

Figure 23: Effect of increasing the window offset (shift) on the SWC results. Each plot shows the real correlation between one node pair (black) and sliding window correlation for the same node pair (pink). (a) The SWC for the 100SN for 100 TRs window has transitions at the state transition points for an offset of one TR. (b) Increasing the offset to one-fourth the window length (25 TRs) resulted in the additional transitions along with the actual transitions after a time equal to the offset (blue oval illustrates one such transition). (c) Increasing the offset to one-half the window length (50 TRs) resulted in the additional transitions along with the actual transitions after a time equal to the offset (blue oval illustrates one such transition).

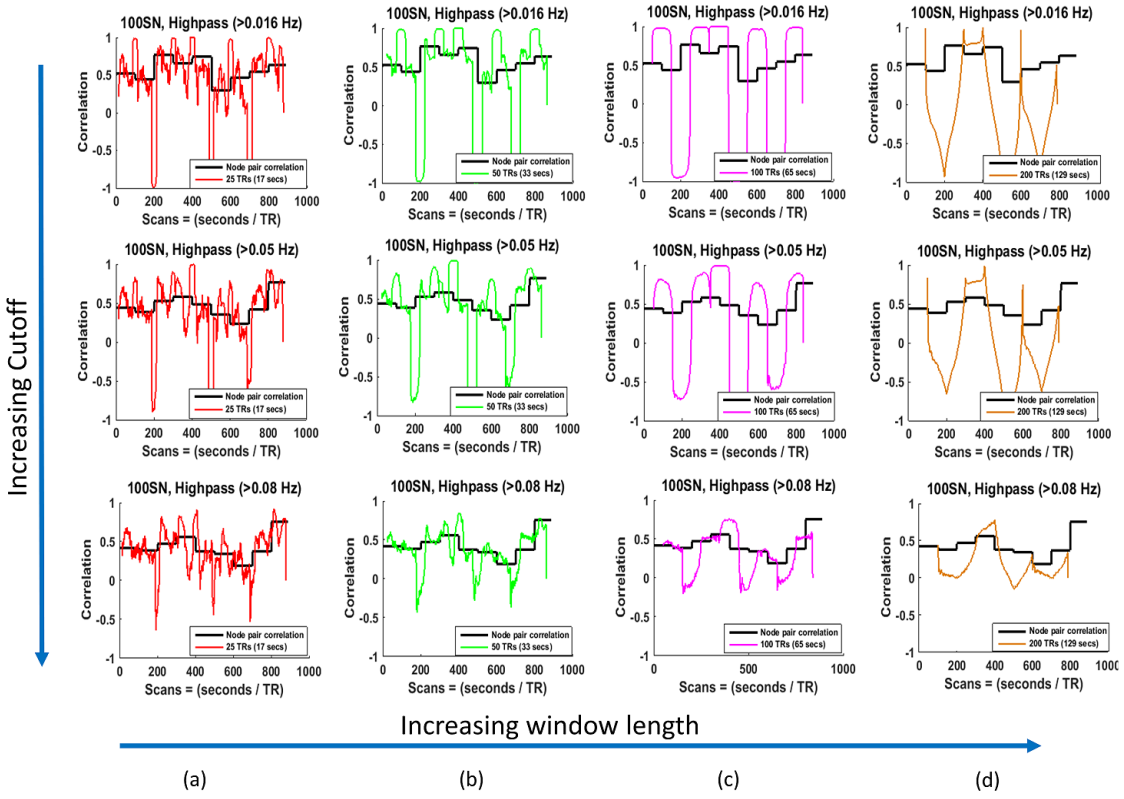

Figure 24: Actual and SWCs of one node pair for 100SN for different highpass cutoffs. The cutoffs are increasing along the rows, while the window sizes are increasing along the columns. (a) Results for 25 TRs (17 secs) window. The window size is larger than minimum window size ($\frac{1}{f_{min}} = 12.5$ sec) to suppress the spurious correlations for row 3 only. Not much difference in the sliding window correlation (SWC) values are observed from first two rows for the same window size. (b) Results for 50 TRs (33 secs) window. The window size is larger than minimum window size ($\frac{1}{f_{min}} = 20$ sec, and 12.5 sec) to suppress the spurious correlations for row 2, and 3. Significant reduction in the SWC values are observed for cutoff > 0.08 Hz. (c) and (d) follow the same trend as (b) for windows of sizes 100 TRs (65 sec), and 200 TRs (129 sec) respectively. In (c) the sharp transitions observe for a cutoff of > 0.01 and > 0.05 Hz (rows 2 and 3) are not present for cutoff > 0.08 Hz (row 3).

state change point even when the window size was same as the state duration, which can be observed in row 3 (c). Since most of the power in the low frequency BOLD fluctuations lie in the very low frequencies (< 0.1 Hz), the filters with higher cutoffs discard much of the information. Similar results were observed in all the subjects.

4.4 Discussion

Dynamic analysis of resting state functional connectivity (FC) holds the potential to provide new insights into the organization and interplay of network activity in the brain. Already it has been shown that dynamic analysis can improve sensitivity to changes that occur in psychiatric disorders [77, 20, 54, 40]. One of the major challenges in furthering the field of dynamic FC is a lack of gold standards that can be used to evaluate how well analysis techniques reflect the actual network interactions in a system where the timing, duration, and composition of states are all unknown.

Previous studies have taken two approaches to the problem, either linking network dynamics to measurable behavioral outputs [45, 91] or tying them to simultaneous measures of electrical activity made with other modalities [15, 90, 92, 68]. These studies impart confidence that dynamic analysis methods reflect at least some of the underlying neural dynamics. However, they do not readily adapt to a systematic investigation of analysis techniques and parameters.

The SWC is one of the simplest and most widely used approaches to dynamic functional analysis, and is sometimes followed by clustering to identify common states of correlation patterns throughout the brain [2, 81]. Most dynamic functional connectivity studies use SWC but the method's performance depends on the choice of parameters like window length, offset etc. In this study, we formed simulated networks (SNs) from real rsfMRI data in order to obtain SWC results similar to those of real FC networks but with controlled state transition times.

Two recent studies [83, 33] analyzed the performance of the SWC for dynamic

analysis and identified shortcomings of the method. [33] reported that the mere presence of fluctuations in the SWC time series cannot be taken as the evidence of dynamic functional connectivity and that it is important to select an appropriate null hypothesis when performing the dynamic FC analysis and [83] compared their proposed method with the SWC. Our approach complements these studies since similar to [83], we observed a significant influence of a change in signal amplitude on the SWC results for all windows (Figure 16). We also observed spurious fluctuations in the results of the SWC for actual rsfMRI networks (Figure 15) and for the SNs (Figure 16), supporting the findings of [33] that the mere presence of fluctuations in the SWC results cannot be taken as evidence of dynamic FC. These similarities in the results validate the use of our SNs for evaluating the impact of parameter choice on the performance of SWC.

The effects of different parameter choices for the SWC and clustering were examined using these model networks. While the SNs were created using data from actual resting state networks, several implicit assumptions may affect their similarity to actual networks in the brain:

1. All nodes were assumed to be connected at all times. The SNs were spatially invariant, meaning that nodes did not join or leave the network at any time.

2. Abrupt transitions occurred between consecutive states. In practice, the characteristics of state transitions in the brain are not known, but it is likely that smoother transitions over the course of seconds occur alongside or instead of abrupt transitions.

3. The average duration of a real brain state is not known. For our study it was modeled as 13 to 129 seconds, ranging from time scales on the order of a cohesive thought to more long-term changes (in vigilance, for example) that occur on the scale of minutes. It is likely that these time scales are expressed simultaneously

in the actual brain. These assumptions are excellent targets for future extensions of this work and more complex model networks may prove more realistic for examining the accuracy of dynamic analysis techniques. Nevertheless, this simple model provides some guidance about the impact of parameter choice on the SWC.

4.4.1 Sharp transitions

Despite the fact that the data in our SNs was from rsfMRI scans, our SNs had sharp state transitions as shown in Figure 14, which is different from the gradual changes expected in real resting-state networks. These sharp state transitions were due to abrupt changes in the signal intensities at the state transition points [55] that acted as outliers, specially for smaller windows (25 TRs, 50 TRs) in which the averaging in the SWC includes a smaller number of points. Although the transitions in our SNs may not reflect the actual state transitions of rsfMRI networks, they clearly identify the important issue of SWC's very high sensitivity to even one large short-lived intensity change [83, 55]. Similar to the results of actual rsfMRI networks (Figure 15.) and previous studies [42, 103] the SWC fluctuated between negative and positive values even when the actual correlation was positive for the SNs. Furthermore, similar to [103] we observed that despite of the large variations for smaller windows, the pattern and timings of these correlation variations were same. For example, in Figure 16., the '-1' correlations appear almost at the same points for all the windows, though other lesser variabilities are smoothed out by an increase in the size of the window, as expected. However, our results differ from those of [103] in the sense that the correlations vary between extreme values of '-1' and '1' regardless of the actual correlation values between two state transition points. A closer inspection of these results show that these variations are mostly accompanied by abrupt signal changes at state transition points. Once the SWC value changed at the state transition point,

it remained the same in most of the cases till the next abrupt signal change (at the next state transition point) especially for longer windows (pink and brown). This may be because the data between two consecutive state transition points was from same resting-state networks so would not have any abrupt changes in signal. For smaller windows (red and green) the window size was less than $\frac{1}{f_{min}}$ which may have introduced spurious fluctuations [53]. These results emphasized the vulnerability of the SWC as an efficient and effective dynamic analysis method for FC. While sharp transitions are troublesome for SWC, the same sharp transitions in our SNs in some sense provided a "best case scenario" for clustering, with distinct boundaries between states that resulted in efficient clustering performance by k-means, with perfect identification of state transitions and durations in the raw SNs.

4.4.2 Window length

As expected, window length had a substantial effect on the amount of variability captured by the SWC and was the single most important determinant of the overall accuracy of the technique. Smaller windows (17 and 33 seconds) had more variability in the SWC results regardless of the SN. Some of these fluctuations maybe the result of spurious fluctuations arising from the SWC algorithm itself based on the findings of a recent study[53]. In this study it was reported that the minimum window length to avoid the spurious fluctuations arising due to the SWC itself should be at least equal to $\frac{1}{f_{min}}$, where f_{min} is the minimum frequency in the simple correlating signal. In our study the f_{min} is 0.016 Hz that corresponds to a minimum window length of 62.5 seconds and window lengths less than this (17 and 33 seconds) would give rise to spurious fluctuations. Regardless of window length, we found the overall correspondence between the actual correlation and the SWC to be rather poor. sliding window correlation (SWC) results were more divergent from the actual correlation values at the time of state transitions illustrating that even a single outlier or abrupt change

can have significant influence on the SWC output [55]. This effect was more pronounced for smaller windows, since the averaging of SWC includes a smaller number of samples, and a large change in the value of even one sample would greatly influence the averaging. Furthermore, smaller windows would introduce spurious fluctuations also [53]. Window sizes that were well matched to the duration of the states provided fairly good sensitivity to state transitions but still gave poor estimates of the actual correlation values. Perhaps because of the sensitivity to transitions, clustering after the SWC provided surprisingly good state identification for window lengths well matched to state durations, despite the poor estimation of correlation values. To some degree, the clustering was able to salvage information from the relatively poor accuracy of the SWC time courses. However, this was only true for certain situations where window lengths aligned well with state durations. It was also noted that in some situations, the duration of Cstates appears to be dominated by the window length rather than by the actual underlying state durations. Surprisingly, the clustering of raw SNs resulted in perfect state transition and duration identifications, giving far better performance than when SWC was used. These ideal results may be due to the sharp state transitions of our SNs which would provide distinct grouping to the clustering algorithm. However, these results also suggest that the application of the SWC is in general detrimental to the identification of brain states, and that clustering based on raw data provides a cleaner estimate of the patterns of underlying activity. If windowing methods are used, the results of these simulations highlight the need for development of adaptive techniques to maximize sensitivity to states of different durations.

4.4.3 Signal-to-noise ratio (SNR)

Additive white Gaussian noise (AWGN) deteriorated the results of both SWC and k-means clustering since it reduced the identification of sharp state transitions. This

AWGN (20dB and 10dB SNRs) was added to the whole length of time series in SNs, and this resulted in less sharp state transitions which influenced the state assignments of the SWC results even for best case scenarios (50SN with 50TRs, 100SN with 100 TRs windows, and 200SN with 200 TRs window). The noise that we added was random, but actual noise is rsfMRI often arises from physiological sources (heart beat at $\approx$ 1 Hz, respiration at $\approx$ 0.3 Hz) and head motion [44, 28, 9, 5] and is spatially structured. These types of noise may introduce structured deterioration in the SWC results.

4.4.4 Window offset

An offset of a single TR proved best for detecting both state changes and durations. Increasing the window offset reduced the sensitivity of the SWC towards the correlation changes, as well as its ability to detect state transitions and durations. The larger the offset, the worse the results became. A closer inspection of the results showed that this deterioration may be due to shifts in the SWC results due to uncertainty in the times which best reflect the average in the window, and to the introduction of new transitions at intervals equal to the offset. To some extent, this may be related to the sharp transitions between networks used for this study and could well be mitigated for networks with more gradual transitions.

4.4.5 Time domain Filtering

Typical rsfMRI scans use a bandpass filter to minimize contributions from noise (typically 0.01-0.1Hz or 0.01-0.08 Hz). Following the findings of [53], we applied highpass filters with different frequency cutoffs to the data. We observed that the highpass filtered SNs provide results similar to bandpass filtered networks when the highpass cutoff was same as the that of the bandpass lower cutoff. As we increased the highpass cutoff to higher values (>0.05 Hz and > 0.08 Hz) magnitudes of the SWC results for windows larger than $\frac{1}{f_{min}}$ were reduced, but the ability of the SWC to follow

actual correlation values did not improve though the sharp state transitions of the SWC results were lost. This suggests that in our model, other sources of variability dominate the signal rather than the instability introduced by a mismatch in frequency and window length. One reason for the differences observed from [53] may be that in our case, correlations were computed for the duration of the states, rather than for the whole scan time, making the sample length shorter. In some sense, the finding that the inclusion of lower frequencies does not greatly impact the performance of the SWC is encouraging. The combined requirements of highpass filtering to match the window length and low pass filtering to limit contributions from noise would place rather stringent limits on the range of windows that could be used to examine the SWC dynamics. The unfortunate corollary of this finding is that since the inclusion of lower frequencies does not greatly impact the SWC, the highpass filter does not appreciably improve the SWC performance, leaving it far from ideal as an analysis technique.

4.4.6 Considerations for future SWC studies

The SWC gives a mediocre estimation of the actual underlying correlation even in the best of circumstances for our SNs, as shown in Figure 16. However, with appropriate window lengths it could detect transition points fairly well, at least in networks with abrupt or sharp transitions. Clustering based on these window lengths resulted in reasonably accurate state identification. The results from our model suggest that the use of a window length equal to or longer than the expected state duration will provide the most accurate state characterizations. This requirement will of course need to be balanced with the necessity of using windows short enough to provide an estimation of changes over time. Shorter windows also identified greater proportions of actual transitions between states, though this is counterweighted by the number of false transitions that occurred. An offset of a single TR and a rectangular window

provided the most accurate results, although this may be due in part to the abrupt changes in the model network. Finally, the results of the SWC applied to QPeriodicSN and RandSN (arguably the most realistic models for the types of transitions expected in rsfMRI) highlight the way that window size impacts the resulting states. A large proportion of the states identified were approximately equal in length to the sliding window, regardless of the length of the actual state duration. This may be an important point to consider during the interpretation of the SWC-based clustering on real rsfMRI data. A surprising and novel aspect of this study was perfect state transition and duration identification obtained using k-means clustering on the raw SN signal. These ideal results may be partly due to abrupt transitions of our SNs and will require further examination. However, they suggest that researchers may wish to consider using clustering-based approaches on the raw signal to identify the states of FC, rather than the SWC time courses whenever possible.

4.4.7 Limitations and Future Directions

This study evaluated the performance of the SWC as a suitable method for capturing network dynamics with rsfMRI. After examining the effects of various parameters on the dynamic analysis results of the SWC, we observed that no set of parameters were suitable for optimum performance of the SWC under conditions that are likely to exist in the human brain (e.g., random lengths of state durations). Windows that matched the intervals at which brain states changed provided the most accurate information, but this situation is unlikely to be found in rsfMRI.

The clear outcome of this study is the need to develop algorithms that can adaptively detect state transitions of different durations. This is a clear target for future research and may be addressed by the use of multiscale approaches (e.g., wavelet-based analysis) that can simultaneously examine multiple time scales. An ideal analysis method would identify each state based on quantitative relationships between

areas, along with transition points between states. The challenge of identifying an optimum number of brain states is another target for future efforts.

Any algorithm that aims to address these issues will need to be tested against modeled network dynamics, but even the best performance on a model network will not guarantee success in identifying transitions of interest in actual resting-state functional MRI (rsfMRI) data. Validation with multimodal data and behavioral outputs will be necessary to conclusively establish a link between the output of the algorithm and activity within the brain. Despite the large amount of work remaining, dynamic rsfMRI has the potential to have a profound impact on our understanding of the brain.

4.5 Conclusion

We used SNs from real resting-state networks and concluded that in the absence of GTs, the SWC is not an efficient method of capturing the dynamics of these networks. It could capture the correlation and state changes reliably under certain conditions that are very unlikely to prevail in real resting-state networks. The results from this chapter analyzed the performance of the SWC comprehensively, and will be excellent guidelines for future studies intending to use the SWC, even in the domains other than brain networks. These results led us to develop a new algorithm to adaptively detect the change point of these networks from raw data, rather than focusing on the results of the SWC as discussed in Chapter 6.

CHAPTER V

FREQUENCY DEPENDENCIES OF SLIDING WINDOW CORRELATION

The blood-oxygen-level-dependent (BOLD) fMRI data contains many source of spatially structured noise arising from physiological sources (heart beat at ≈ 1 Hz, respiration at ≈ 0.3 Hz) and head motion [5, 44, 9, 28]. The functional connectivity (FC) between two regions in the brain is derived form the correlation of their MRI signal fluctiations [5]. These correlations may arise due to head motion and/or physiological processes such as cardiac pulsation (1 Hz) and respiration (0.3 hz). However, correlated signal fluctuations in the BOLD resting-state functional MRI (rsfMRI) occur at low temporal frequencies (< 0.1 Hz) [7, 18]. So, influence of the structured noise is reduced during the preprocessing by filtering (heart and respiration) and regression (motion parameters) without affecting the low frequency BOLD signal. The frequency range to eliminate the cardiac and respiration noises is varied in different studies which may influence results of the sliding window correlation (SWC). The study in this chapter focuses on this aspect of the SWC analysis. The study presented in this chapter has been published partially in [79]. An invited extended version of the study is submitted for publication in the special issue of IEEE BIBM 2015 BMC Systems Biology.

5.1 Motivation

The dynamic FC studies are performed on the bandpass filtered data (0.01-0.08 or 0.01-0.1 Hz) and the frequency range of the correlating signals may influence the SWC parameters. Despite the popularity of the SWC method, the selection of the

best window size is still a challenging issue. So far the only guidance seems to have come from a recent study [53] that identified the best minimum window length for simplified signals containing only a single-frequency component. The study can be a milestone for deciding minimum window size in the SWC analysis. However, the study ignored the fact that the actual rsfMRI signals contain more than one frequency component and their combination may affect the final result. Since the frequency range in different studies differ based on the cutoffs of the filter used, there is a need to explore the influence of more than one frequency on the window length and SWC results. In this chapter we extended the approach used in [53] to signals with two frequency components separated by a phase lag only. Afterwards, we explored the influence of multiple frequency components. We started the analysis with a study of sliding window covariance, and extended it to the SWC by normalization. The effect of non-stationarity is also explored by using modulating signals with low frequency components. Similar to [53], the analysis is done in two steps: First a time domain analysis on stationary signals and then a frequency domain analysis on non-stationary signals.

5.2 Stationary Signals

5.2.1 Two Frequencies

We started our analysis with two stationary deterministic signals x_i and y_i given by

$$x_i = A_1 \cos(2\pi f_1 iTR) + A_2 \cos(2\pi f_2 iTR) \tag{11}$$

$$y_i = A_1 \cos(2\pi f_1 iTR + \theta) + A_2 \cos(2\pi f_2 iTR + \theta) \tag{12}$$

in which f_1, f_2 ($f_2 > f_1$) are the frequencies of two sinusoids with amplitudes A_1, A_2 respectively and θ is the phase lag between the two signals, which is taken to be the same for both the frequency components for simplification of computations. Since rsfMRI signals are bandpass filtered before any SWC analysis, we can assume these two frequencies to be the bandpass cutoffs with $f_{min} = f_1$, $f_{max} = f_2$, and $f_{max} > f_{min}$.

The covariance of these two signals over the window w can be computed using the Equation 3 and is given by,

$$c_{xy}[n] = \frac{(A_1^2 + A_2^2)}{2}\cos(\theta) + (\frac{1}{4\pi w})(C) - (\frac{A_1 A_2}{4(\pi w)^2})(D) \tag{13}$$

in which (C) and (D) are terms dependent on the window length w and their detailed derivation can be seen from Appendix A in Chapter 8.

5.2.1.1 Infinite Window Length

Stationary covariance over the entire signal length would be obtained from Equation 13 when $w \to +\infty$ [53], and the value of the stationary covariance is given by:

$$\lim_{w \to +\infty} c_{xy}[n] = \frac{(A_1^2 + A_2^2)}{2}\cos(\theta) \tag{14}$$

5.2.1.2 Finite Window Length

We can observe that the spurious fluctuations are introduced from second and third terms in Equation 13 for a finite window length and the covariance over the window w approaches the stationary covariance when these terms are zero.

i.e., $(C) = 0$ *and* $(D) = 0$.

Solving from Appendix A in Chapter 8.

$$\begin{aligned} &\frac{\sin(2\pi f_j w)}{\alpha_j f_j} = 0 \Rightarrow f_j = \frac{n_j}{w}, \\ &\textit{in which } \alpha_j \ = \ \textit{constant}, \ n_j = 0, 1, 2....., j = 1:4 \end{aligned} \tag{15}$$

From the above equation we get the ratio:

$$\frac{f_2}{f_1} = \frac{n_2}{n_1} \tag{16}$$

since $f_2 > f_1 \Rightarrow n_2 > n_1$.

Since rsfMRI signals are bandpass filtered before any SWC analysis, we can assume these two frequencies to be the bandpass cutoffs with $f_{min} = f_1$, $f_{max} = f_2$, and $f_{max} > f_{min}$. There are two possibilities for the ratio of f_1 and f_2, discussed below in detail.

1. CASE 1: f_2 is an integer multiple of f_1.

   For this case we have $n_2 = m_1(n_1)$, in which m_1 is an integer. As a result we have $f_2 = m_1(f_1)$, $f_3 = f_2 + f_1 = (m_1 + 1)f_1 = (m_2)f_1$, and $f_4 = f_2 - f_1 = (m_1 - 1)f_1 = (m_3)f_1$, in which m_2 and m_3 are also integers. Putting all of these values in Equations 49 and 52 would result in second and third terms of Equation 13 to be zero if w is an integer multiple of $1/f_1$, which will give sliding window covariance equal to actual stationary covariance at multiples of the $1/f_1$. This result agrees with the result of [53] which reported that sliding window covariance approaches stationary covariance by reducing spurious fluctuations when the window length is greater than $1/f_1$ and is equal to the exact value of the stationary covariance at the integer multiple of $1/f_1$.

2. CASE 2: f_2 is not an integer multiple of f_1.

   For this case we have $n_2 = l_1(n_1)$, in which l_1 is an not an integer. As a result we have $f_2 = l_1(f_1)$, $f_3 = f_2 + f_1 = (l_1 + 1)f_1 = (l_2)f_1$, and $f_4 = f_2 - f_1 = (l_1 - 1)f_1 = (l_3)f_1$, in which l_2 and l_3 are also not integers. Putting all of these values in Equations 49 and 52 would result in non-zero second and third terms of 13 even when w is equal to $1/f_1$, since the arguments of the 'sin' would not be an integer multiple of π. It will result in zero values only when w is such that it cancels out the products of $l_1(f_1)$, $l_2(f_1)$, and $l_3(f_1)$ at the same time giving all the angles to be an integer multiple of π.

   This results from CASE 1 and 2 above show that the ratio of both frequencies in the correlating signals influence the tendency of sliding window covariance

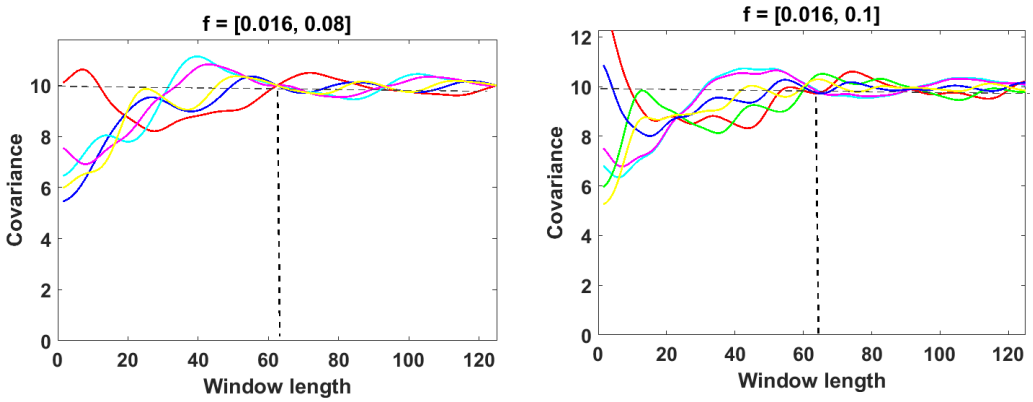

Figure 25: Covariance of stationary deterministic signals with two frequency components. (a) when the minimum (smaller) frequency is an integer multiple of maximum (larger) frequency and (b) when it is not an integer multiple.

to approach the stationary covariance.

Figure 25. shows the results of sliding window covariance when the higher frequency f_2 is an integer multiple of the lower frequency f_1 in (a) and when it is not an integer multiple in (b) for various n in Equation 13. The lower frequency in both the cases is 0.016 Hz, which would result in minimum window length w ($= \frac{1}{f_1}$) to be 62.5 seconds as shown by dashed vertical black lines in both the figures. The amplitudes $A_1 = 4$, $A_2 = 2$, and θ =0, resulting in stationary covariance of 10 (black dashed horizontal lines). It can be observed from these figures that even though the spurious fluctuations diminish in general for every n when the window length is above $\frac{1}{f_1}$, the exact stationary covariance value is approached at this window length only when the higher frequency is an integer multiple of the lower frequency.

5.2.2 Multiple Frequencies

Since the correlating signals are bandpass filtered (normally from 0.01-0.08 Hz or 0.01-0.1 Hz), there are more than two frequency components present in them starting from $f_{min}(0.01Hz)$ and ending at $f_{max}(0.08\ or\ 0.1Hz)$. In order to observe the influence of more than two frequencies, we extended our frequency based analysis to correlating

signals with multiple frequency components. Let x_i and y_i be two correlating signals having m distinct frequencies and corresponding amplitudes, and differing in phase only. Also suppose these frequencies lie between f_{min} and f_{max} such that $f_{min} = f_1 < f_2 < ... < f_m = f_{max}$. we further assumed the phase lag θ between all frequency components to be same for simplification of the computations and to observe the influence of frequencies only.

$$\begin{aligned} x_i &= \sum_{j=1}^{m} A_j cos(2\pi f_j iTR) \\ y_i &= \sum_{j=1}^{m} A_j cos(2\pi f_j iTR + \theta) \end{aligned} \tag{17}$$

Using Equation (3), the covariance of these two signals would be given by (See Appendix A (Chapter 8) for details):

$$c_{xy}[n] = \sum_{j=1}^{m} \frac{A_j^2}{2} \cos(\theta) + (\frac{1}{8\pi w})(E) + (\frac{1}{2\pi w f_{k+l}})(F) + (\frac{1}{4\pi w f_{k-l}})(G) - (\frac{1}{4\pi^2 w^2})(H) \tag{18}$$

In which (E), (F), (G), and (H) involve the terms with $sin(n\pi f_x w)$, in which f_x is some frequency and w is the window length.

5.2.2.1 Infinite Window Length

Stationary covariance over the entire signal length would be obtained from Equation 18 when $w \to +\infty$ [53], and the value of the stationary covariance is

$$\lim_{w \to +\infty} c_{xy}[n] = \sum_{j=1}^{m} \frac{A_j^2}{2} \cos(\theta) \tag{19}$$

5.2.2.2 Finite Window Length

The spurious fluctuations would be introduced from last four terms in Equation 18 that depend on the window length and the covariance over the finite window w approaches the stationary covariance when these terms are zero *i.e.*, (E), (F), (G), *and* $(H) =$

0.

Solving from Appendix A in Chapter 8.

$$
\begin{aligned}
&E = 0 \Rightarrow \sum_{j=1}^{m} \frac{A_j^2}{f_j} \cos(4\pi f_j nTR + \theta) \sin(2\pi w f_j) \Rightarrow \sin(2\pi w f_j) = 0 \\
&\Rightarrow f_j = \frac{n_j}{w},\ in\ which\ n_j = 0, 1, 2....., j = 1, 2, ..., m \\
&Similarly\ F = 0 \Rightarrow \sin(\pi w f_{k+l}) = 0 \Rightarrow f_{k+l} = \frac{n_{k+l}}{w}, \\
&Similarly\ G = 0 \Rightarrow \sin(\pi w f_{k-l}) = 0 \Rightarrow f_{k-l} = \frac{n_{k+l}}{w}, \\
&Similarly\ H = 0 \Rightarrow \sin(\pi w f_k) = 0\ or\ \sin(\pi w f_l) = 0 \Rightarrow f_k = \frac{n_k}{w}, f_l = \frac{n_l}{w} \\
&in\ which\ f_{k+l} = f_k + f_l\ ,\ f_{k-l} = f_k - f_l
\end{aligned}
\tag{20}
$$

in which n_k and n_l are integers and $k \neq$ l.

Solving the above equations we get:

$$
\frac{f_k}{f_l} = \frac{n_{k+l} + n_{k-l}}{n_{k+l} - n_{k-l}},\ k > l \tag{21}
$$

since $f_k > f_l\ when\ k \neq\ l \Rightarrow (n_{k+l} + n_{k-l}) > (n_{k+l} - n_{k-l})$. In Equation 21 the numerator would always be greater than denominator so the fraction would always be greater than 1. So $f_k > f_l$.

We will explore the influence of more than two frequency components in the correlating signals with the help of an example below.

Example:

Let $f_1,\ f_2,\ f_3$ be three frequencies present in the correlating signals in which $f_1 <\ f_2 <\ f_3$. Then the frequency ratios greater than '1' would be:

$\frac{f_3}{f_1} = n_{31},\ \frac{f_3}{f_2} = n_{32},\ \frac{f_2}{f_1} = n_{21},$ in which $n_{31}, n_{32},\ and\ n_{21}$ are all greater than '1'.

From the above ratios, we have: $f_3 = n_{21} f_1$ and $f_2 = \frac{n_{31}}{n_{32}} f_1 = n_{3132} f_1$, in which $n_{3132} = \frac{n_{31}}{n_{32}}$, and $\frac{n_{31}}{n_{32}}$ is greater than '1'.

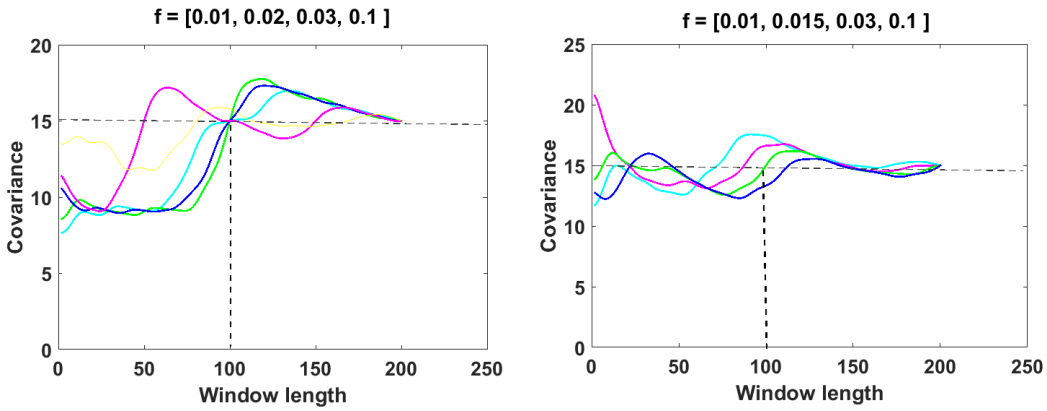

Figure 26: Covariance of stationary deterministic signals with multiple frequency components (a) when all the higher frequencies are integer multiples (harmonics) of the smallest frequency and when (b) they are not multiples.

The above results show that all the frequencies will be a multiple of the minimum frequency f_1.

1. CASE 1: f_k is an integer multiple of f_1 where k = 2,3.

   In this case $f_2 = m_1(f_1)$, $f_3 = m_2(f_1)$ in which m_1 and m_2 are integers. From Equations 56 and 60, we can see that the terms with sums and differences of the three frequencies f_1, f_2, f_3 are also present. All of these would be sums and differences of integers so they will also be integers. Putting these values in Equations 56 and 60 would result in all terms equal to zero if w is an integer multiple of $1/f_1$, which will give sliding window covariance equal to actual stationary covariance at multiples of the $1/f_1$. This result agrees with the result of [53] which reported that sliding window covariance approaches stationary covariance by reducing spurious fluctuations when the window length is greater than $1/f_1$ and is equal to the exact value of the stationary covariance at the integer multiple of $1/f_1$.

2. CASE 2: f_k is an not an integer multiple of f_1 where k = 2,3.

   Similar to the case of two frequency components in Subsection 5.2.1, the terms

containing w would not be zero in this case unless the product of all frequencies and their multiples are an integer multiple of window length w.

The above results show can be generalized to show that the SWC would be able to estimate the actual correlation for a window of length $\frac{1}{f_{min}}$ only when all the higher frequencies are integer multiples of $\frac{1}{f_{min}}$. Otherwise, the window length w has to cancel out the non-integer multiples of all frequencies, which is a condition that is not expected in exist in realistic scenario. Figure 26. shows the plots for the case when the correlating signals contain four frequency components that are integer multiple of the smallest frequency in (a) and not an integer multiple in (b).

5.3 Non-stationary Signals

5.3.1 Single Modulating Frequency

The actual rsfMRI signals are non-stationary with some modulating signals modifying the frequencies of the stationary signals. So we introduced non-stationarity in the correlating signals by multiplying one of the stationary signals with a modulating waveform [53] $\cos(2\pi f_0 iTR)$, in which $f_0 << f_1$ and $f_0 << f_2$. Since the SWC is used to capture the variability of the correlating signals, so some appropriate window length should be able to capture the non-stationary frequency f_0 only. In this part of the study we tried to find the window length to reject all frequencies other than this modulating frequency. For the sake of computations we will take the phase lag $\theta = 0$. Furthermore, we would do the non-stationary analysis in frequency (Fourier) domain since we are looking for the relationship between the window length and frequency components of the correlating signals, and also because it would show the interactions between the frequency components more clearly [53]. Let us multiply the signal y_i by the modulating signal to introduce non-stationarity

$$
\begin{aligned}
y_i &= (A_1 \cos(2\pi f_1 iTR) + A_2 \cos(2\pi f_2 iTR)) \cos(2\pi f_0 iTR) \\
&= (\frac{1}{A_1}(\cos(2\pi(f_1 + f_0)iTR) + \cos(2\pi(f_1 - f_0)iTR)) \\
&+ \frac{1}{A_2}(\cos(2\pi(f_2 + f_0)iTR) + \cos(2\pi(f_2 - f_0)iTR))
\end{aligned} \tag{22}
$$

Sliding window covariance c_{xy} can be taken as the convolution(*) with rectangular window h in time domain [53]

$$c_{xy} = (xy) * h - (x * h)(y * h) \tag{23}$$

in which

$$h = \begin{cases} \frac{TR}{w} & \text{if } |n| \leq \Delta; \\ 0 & \text{otherwise.} \end{cases}$$

Since convolution in frequency domain is multiplication in time domain and vice versa, the discrete Fourier transform (DFT) of the Equation 23 can be given as

$$C_{xy} = (X * Y)H - (XH) * (YH) \tag{24}$$

The captial letters are DFTs of the signals. In DFT the k^{th} frequency of a signal of length N sampled with period TR is equal to $f_k = \frac{k}{NTR}$. Some of the DFT pairs we used are given below

$$\cos(2\pi k_0 \frac{n}{N}) \overset{\mathcal{F}}{\leftrightarrow} \frac{1}{2}(\delta(k + k_0) + \delta(k - k_0)) \tag{25}$$

$$H[k] \;=\; h \overset{\mathcal{F}}{\leftrightarrow} \; (\frac{TR}{w})\frac{\sin(\pi k w/(NTR))}{\sin(\pi k/(NTR))} \tag{26}$$

Where δ is the Kronecher-delta function ($\delta[k] = 1$ for $k = 0$), and H[k] is the famous Dirichlet kernel, which is a discrete version of the sinc-function.

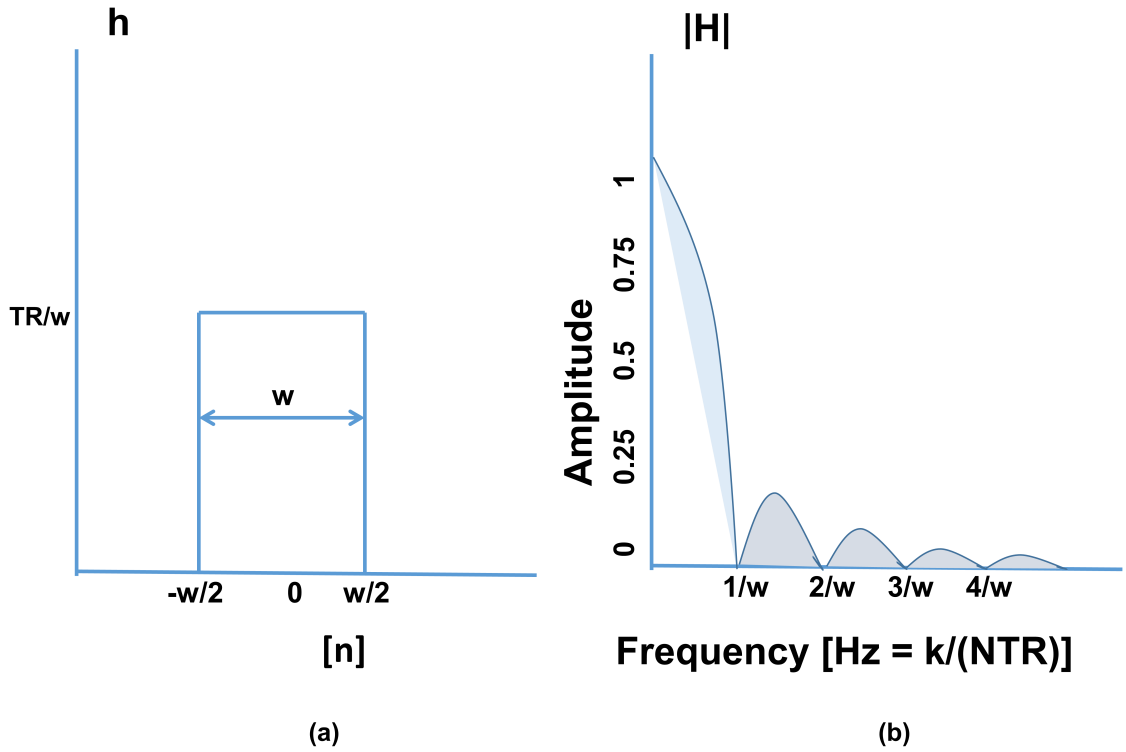

Figure 27: The filter h in time in (a) and it spectrum $|H|$ in frequency in (b). The width of the main lobe is dependent on $1/w$.

Figure 27. shows the filter h in time in (a) and its frequency spectrum $|H|$ in (b). In frequency domain the width of the main lobe is governed by length of the window w. Since the side lobes have very small amplitudes, the application of the filter on any signal would retain the frequencies within the main lobe only.

The DFTs of the signals $x[n]$ and $y[n]$ are given by

$$\begin{aligned} X[k] = \mathcal{F}(x[n]) = \\ \mathcal{F}(A_1 \cos(2\pi f_1 NTR\frac{n}{N}) + A_2 \cos(2\pi f_2 NTR\frac{n}{N})) \\ = \frac{A_1}{2}(\delta(k + f_1 NTR) + \delta(k - f_1 NTR)) \\ + \frac{A_2}{2}(\delta(k + f_2 NTR) + \delta(k - f_2 NTR)) \end{aligned} \tag{27}$$

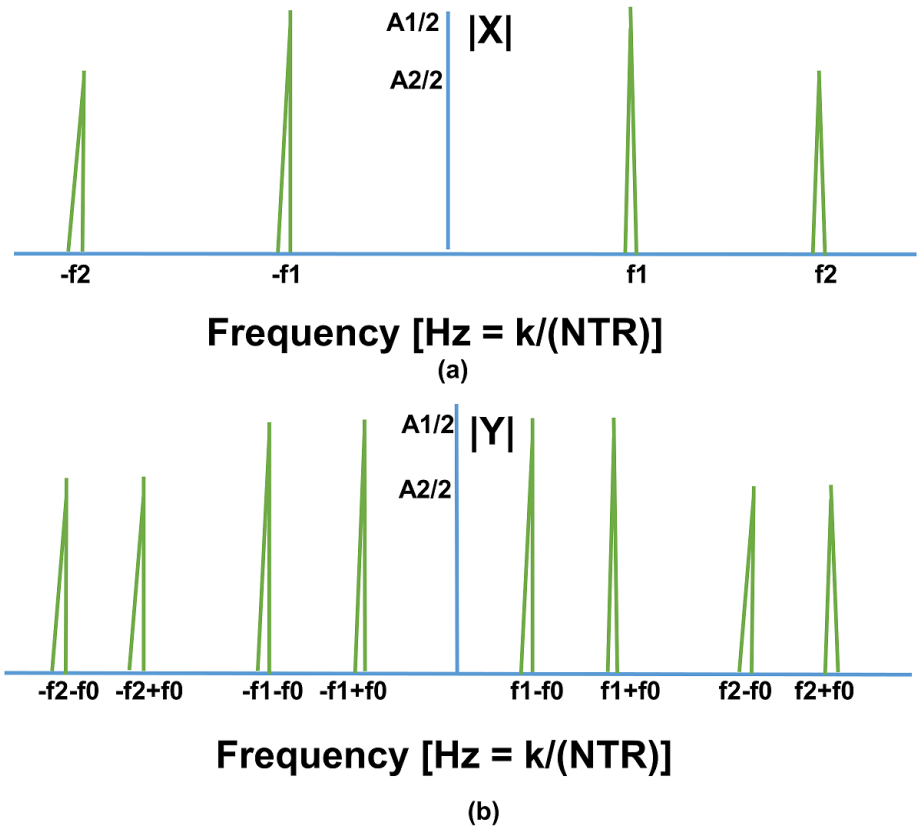

Figure 28: The discrete Fourier transform of (a) $x[n]$ and (b) $y[n]$.

Similarly

$$\begin{aligned} Y[k] = \mathcal{F}(y[n]) = \frac{A_1}{4}(\delta(k + (f_1 + f_0)NTR) \\ + \delta(k - (f_1 + f_0)NTR)) + \frac{A_1}{4}(\delta(k + (f_1 - f_0)NTR) \\ + \delta(k - (f_1 - f_0)NTR)) + \frac{A_2}{4}(\delta(k + (f_2 + f_0)NTR) \\ + \delta(k - (f_2 + f_0)NTR)) + \frac{A_2}{4}(\delta(k + (f_2 - f_0)NTR) \\ + \delta(k - (f_2 - f_0)NTR)) \end{aligned} \tag{28}$$

It can be seen from Figure 28. that the DFT spectrum are symmetric so we can drop the negative axis of the spectrum without any loss of information. Also we assume that $w = \frac{1}{f_{min}}$ in Figure 27., in which f_{min} is the minimum frequency in the correlating signals and $f_2 > f_1 \geq f_{min} > f_0$. Under these assumptions product (XH) would be zero as all of its frequency components are beyond the main lobe of the filter

convolution of (XH) and (YH) would result in almost zero values. So, the Equation 24 would reduce to,

$$C_{xy} = (X * Y)H \tag{29}$$

We compute X*Y by convolving values from Equations 27. and 28. and multiplying the product by H to compute C_{xy}. Since the computation would result in a large number of terms and most of them would either be on negative axis of the spectrum, or outside the main lobe of H. These terms would be dropped after multiplication with H in the final result so here we will present only the terms which would be left at the end. Specifically we are dropping the terms on the negative axis and the ones where $\delta[k]$ is at $2f_1 + f_0,\ 2f_1 - f_0,\ 2f_2 + f_0,\ 2f_2 - f_0,\ f_1 + f_2 + f_0$, and $f_1 + f_2 - f_0$ on the positive axis. We could drop all of these terms since $2f_1,\ 2f_2$, and $f_1 + f_2$ are larger than f_{min}, and f_0, resulting all of these terms falling beyond the main lobe of the filter H. Since the amplitudes of the frequency components, A_1 and A_2 do not influence the behavior of the sliding window covariance so we take $A_1 = A_2 = 1$ to further simplify the computations. The final value of C_{xy} would be:

$$\begin{aligned} C_{xy} = (X * Y)H &= \delta(k - f_0 NTR) \\ &+ \frac{1}{2}\delta(k - ((f_2 - f_1) - f_0)NTR) + \frac{1}{2}\delta(k - ((f_2 - f_1) + f_0)NTR) \end{aligned} \tag{30}$$

1. CASE 1: $f_{min} = f_1$, and $f_2 = m(f_1)$, m < 2.

   Since we started our analysis with the assumption that the two frequencies f_1 and f_2 are the minimum and maximum frequencies of the correlating signals respectively and we concluded from discussion in the previous sections that the spurious fluctuations would be avoided if the window length w is at least $\frac{1}{f_{min}}$, so it is reasonable to take $f_{min} = f_1$, which will give $w = \frac{1}{f_1}$. When m is < 2

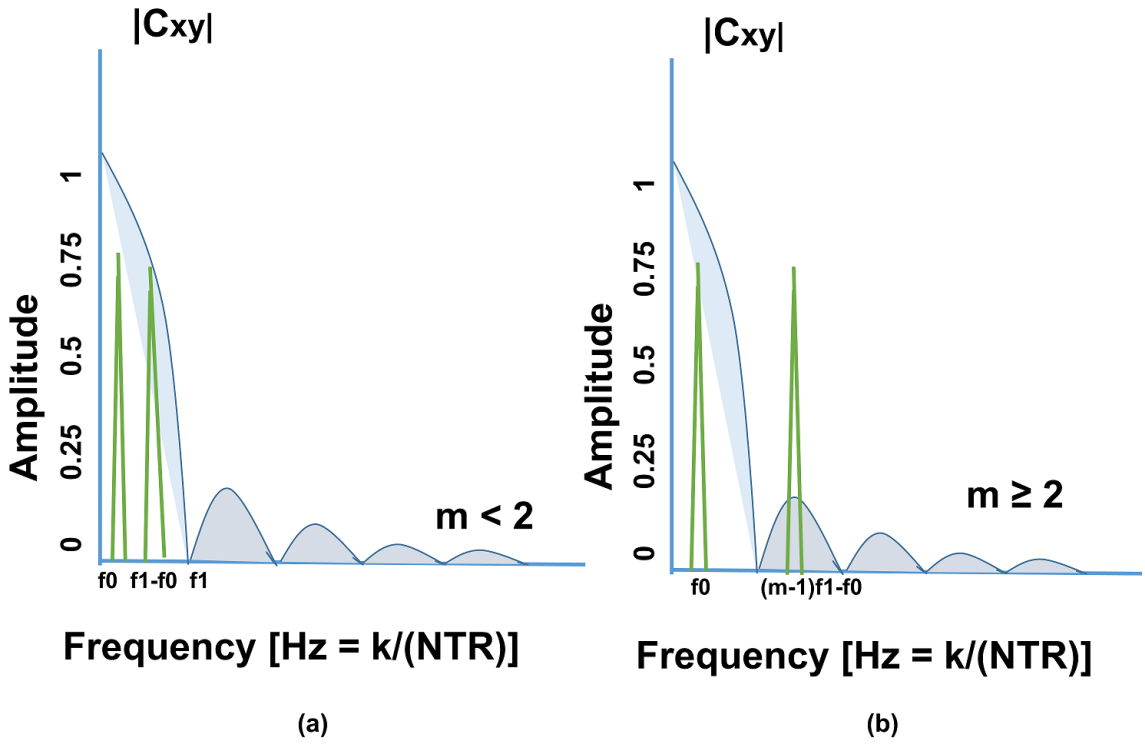

Figure 29: Plots of C_{xy} overalid on plots of $|H|$. Undesirable frequency components at $((m-1)f_1 - f_0)$ and/or $((m-1)f_1 + f_0)$ are extracted if the ratio of f_2 and f_1 is less than or equal to 2.

undesirable frequency components at $((m-1)f_1 - f_0)$ and/or $((m-1)f_1 + f_0)$ would be extracted in addition to the modulating frequency components at f_0 since $((m-1)f_1 - f_0) \leq f_1$ and/or $((m-1)f_1 + f_0) \leq f_1$.

2. CASE 2: $f_{min} = f_1$, and $f_2 = m(f_1)$, m ≥ 2.

   In this case $((m-1)f_1 - f_0) \geq f_1$ and $((m-1)f_1 + f_0) \geq f_1$, so only the modulating frequency components at f_0 would be extracted.

   Figure 29. shows the plots of C_{xy} overlaid on the plots of H when m < 2 in (a) and $m \geq 2$ in (b). For m < 2, the end result contains undesirable frequency components in addition to the modulating frequency at f_0. This results signify the fact that the ratio of the two frequencies should be greater than some specific value for successful extraction of modulation frequency only for the case when only one modulating frequency is involved. Since we do not know the exact nature of non-stationarity in the real rsfMRI signals, we can assume that the modulating frequencies would be more than one which can result in more complicated restrictions on this ratio. Next we explore the influence of two modulating frequencies on the end result.

5.3.2 Two Modulating Frequencies

We increased the non-stationarity of two correlating signals by multiplication of one signal with two modulating signals $\cos(2\pi f_{01} iTR)$ and $\cos(2\pi f_{02}) iTR$, in which $f_2 > f_1 >> f_{01} >> f_{02}$. The non-stationary signal y_i can be given by:

$$
\begin{aligned}
y_i &= \{(A_1\cos(2\pi f_1 iTR) + A_2\cos(2\pi f_2 iTR))\}\cos(2\pi f_{01} iTR)\cos(2\pi f_{02} iTR) \\
&= \frac{1}{2}\{(A_1\cos(2\pi f_1 iTR) + A_2\cos(2\pi f_2 iTR))\}\{\cos(2\pi(f_{01}+f_{02})iTR) \\
&+ \cos(2\pi(f_{01}-f_{02})iTR)) \\
&= \frac{1}{2}\{(A_1\cos(2\pi f_1 iTR) + A_2\cos(2\pi f_2 iTR))\}\{\cos(2\pi(f_{03})iTR) + \cos(2\pi(f_{04})iTR))\} \\
&= \underbrace{\frac{1}{2}\{(A_1\cos(2\pi f_1 iTR) + A_2\cos(2\pi f_2 iTR))\}\cos(2\pi(f_{03})iTR)}_{\text{y1}} \\
&+ \underbrace{\frac{1}{2}\{(A_1\cos(2\pi f_1 iTR) + A_2\cos(2\pi f_2 iTR))\}\cos(2\pi(f_{04})iTR)}_{\text{y2}} \\
&\textit{in which } f_{03} = f_{01} + f_{02} \textit{ and } f_{04} = f_{01} - f_{02}
\end{aligned}
\tag{31}
$$

In this case the modulating frequencies are at $f_{01} + f_{02}$ and $f_{01} - f_{02}$, and the desirable window would be the one that would reject all frequencies other than these two. The covariance can be given by:

$$
\begin{aligned}
C_{xy} &= (X * (Y1 + Y2))H - (XH) * ((Y1 + Y2)H) \\
&\textit{in which } Y1 = \mathcal{F}(y_1) \textit{ and } Y2 = \mathcal{F}(y_2)
\end{aligned}
\tag{32}
$$

X[k] would be the same as for single modulating frequency with frequency components beyond f_1 and f_2 so multiplied by very low magnitude (side lobes) of H. As a result (XH) would be almost zero and convolution with (Y1 + Y2)H would result is almost zero values no matter what the frequencies components of Y1 and Y are. Hence, the covariance would become, a

$$
\begin{aligned}
C_{xy} &= (X * (Y1 + Y2))H \\
&= (X * Y1)H + (X * Y2)H
\end{aligned}
\tag{33}
$$

Proceeding similar to Equation 28, we get,

$$
\begin{aligned}
Y1[k] = \mathcal{F}(y1[n]) = \frac{A_1}{8}(\delta(k + (f_1 + f_{03})NTR) \\
+ \delta(k - (f_1 + f_{03})NTR)) + \frac{A_1}{8}(\delta(k + (f_1 - f_{03})NTR) \\
+ \delta(k - (f_1 - f_{03})NTR)) + \frac{A_2}{8}(\delta(k + (f_2 + f_{03})NTR) \\
+ \delta(k - (f_2 + f_{03})NTR)) + \frac{A_2}{8}(\delta(k + (f_2 - f_{03})NTR) \\
+ \delta(k - (f_2 - f_{03})NTR))
\end{aligned} \tag{34}
$$

Similarly,

$$
\begin{aligned}
Y2[k] = \mathcal{F}(y1[n]) = \frac{A_1}{8}(\delta(k + (f_1 + f_{04})NTR) \\
+ \delta(k - (f_1 + f_{04})NTR)) + \frac{A_1}{8}(\delta(k + (f_1 - f_{04})NTR) \\
+ \delta(k - (f_1 - f_{04})NTR)) + \frac{A_2}{8}(\delta(k + (f_2 + f_{04})NTR) \\
+ \delta(k - (f_2 + f_{04})NTR)) + \frac{A_2}{8}(\delta(k + (f_2 - f_{04})NTR) \\
+ \delta(k - (f_2 - f_{04})NTR))
\end{aligned} \tag{35}
$$

Convolution of X with Y1 would give terms at the negative frequencies (i.e. at $-2(f_1 + f_{03}),\ -2(f_1 - f_{03}),\ -2(f_2 + f_{03}),\ -2(f_1 - f_{03}),\ -(f_1 + f_2 + f_{03}),\ -(f_1 + f_2 - f_{03}),\ -(f_2 - f_1 + f_{03}),\ and\ -(f_1 - f_2 - f_{03})$. All of these negative frequency components can be ignored. Similarly there will be frequency components beyond $f_1 = f_{min}$ (i.e. at $2f_1 + f_{03},\ 2f_1 - f_{03},\ 2f_2 + f_{03},\ 2f_2 - f_{03},\ f_1 + f_2 + f_{03},\ f_1 + f_2 - f_{03}$. Since the filter H cutoff is at f_{min} so these frequency components would also be eliminated after multiplication with H. So after removing these terms the product would become,

$$
\begin{aligned}
(X * Y1)H = \frac{1}{2}\delta(k - f_{03}NTR) \\
+ \frac{1}{4}\delta(k - ((f_2 - f_1) - f_{03})NTR) + \frac{1}{4}\delta(k - ((f_2 - f_1) + f_{03})NTR)
\end{aligned} \tag{36}
$$

Similarly,

$$(X * Y2)H = \frac{1}{2}\delta(k - f_{04}NTR) + \frac{1}{4}\delta(k - ((f_2 - f_1) - f_{04})NTR) + \frac{1}{4}\delta(k - ((f_2 - f_1) + f_{04})NTR) \tag{37}$$

So

$$\begin{aligned} C_{xy} = &\frac{1}{2}\delta(k - f_{03}NTR) + \frac{1}{2}\delta(k - f_{04}NTR) \\ &+ \frac{1}{4}\delta(k - ((f_2 - f_1) - f_{03})NTR) + \frac{1}{4}\delta(k - ((f_2 - f_1) + f_{03})NTR) \\ &+ \frac{1}{4}\delta(k - ((f_2 - f_1) - f_{04})NTR) + \frac{1}{4}\delta(k - ((f_2 - f_1) + f_{04})NTR) \end{aligned} \tag{38}$$

Similar to single modulating frequency case, the components at undesirable frequencies $(f_2 - f_1) + f_{03},\ (f_2 - f_1) - f_{03}, (f_2 - f_1) + f_{04}, and\ (f_2 - f_1) - f_{04}$ would be eliminated if $f_2 = mf_1$, and $m \geq 2$. For both cases of single and two modulating frequencies we explored the case when there were only two frequencies in the correlating signals and discovered that the undesirable frequencies would be avoided if these two frequencies have some specific ratio. Increasing the number of frequencies beyond two may introduce more undesirable frequency components in the results.

5.3.3 Limitations and Future Directions

Our study shows that for the SWC to approach the stationary correlation, the higher frequencies in correlating signals should be an integer multiple of the lowest frequency even for combination of simple sinusoids. Also for the SWC to reject all frequencies other than the modulating frequencies, there should be some specific ratio of the correlating frequencies, even for simple case of two frequencies in the correlating sinusoids. Since the real rsfMRI signals include multiple frequencies, which may not be harmonics of the fundamental frequency, the SWC may not be able to estimate the actual correlations reliably. This work is limited to very simple sinusoids involving

number of frequency components. The real resting-state networks are not expected to contain simple sinusoids so from that perspective these results do not cover realistic possibilities. However, since the SWC is not performing optimally for these simple sinusoids so it is reasonable to presume that it would perform worse for real data. With more complicated signals, future work in this direction may be able to estimate the frequency components of the real resting-state networks and analyze the performance of the SWC on them.

5.4 Conclusion

This study analyzed the impact of frequency components of correlating sinusoids on SWC results. We found that there were spurious fluctuations arising due to the SWC method itself. These fluctuations were reduced significantly if the window length was at least equal to the reciprocal of the minimum frequency in the correlating signal, similar to the result of [53]. However, we also observed that the SWC would approach the exact stationary correlation value at this window length (and at its integer multiples) if the higher frequencies are an integer multiple (harmonics) of the lowest frequency. Another important result of our study showed that if the ratio of the two frequencies was less than a certain value, the SWC would result in extracting undesirable frequency components for non-stationary signals in addition to the desirable modulating frequency components. These are important results since they signify the importance of frequency ratio in deciding the window length instead of just the minimum frequency of the correlating signals.

CHAPTER VI

ADAPTIVE NETWORK CHANGE POINT DETECTION

The presence of QPPs [62, 61], co-activation patterns [57, 56], and spontaneous BOLD events [72] in the rsfMRI indicate that functional connectivity (FC) networks change over time by changes in the intensity levels of their regions. We used this observation to formulate a novel algorithm for adaptive network change point detection of these networks. Once these change points are detected the connectivity between any two such points can be computed by using adaptive window in the sliding window correlation (SWC) or by any other appropriate measure. In this chapter we will present the algorithm followed by the results of its application on simulated and real networks.

6.1 Motivation

Our findings in the previous chapters clearly showed the inadequacy of the SWC as an efficient method for the study of dynamics in FC networks. These findings emphasized the need to developed new algorithms to detect the change points of these networks adaptively. We developed such an algorithm by focusing on the findings of some recent studies [62, 61, 57, 56, 72] about the presence of QPPs, co-activations patterns and spontaneous BOLD events. In QPPs [62, 61], the transition from one network (e.g. DMN) to another (e.g. TPN) takes place within a span of few seconds (20 seconds between DMN and TPN). This transition is observable even by naked eye by looking at the gradual change in the intensity levels of the regions involved [62]. Mostly the transition from one network to another takes place by the simultaneous sign changes in the intensities of various regions from negative to positive and vice versa. Co-activation patterns [57, 56] approach states that the spontaneous activity in the brain maybe dominated by brief instances of activations and deactivations.

This again involves simultaneous sign changes of the participating regions. Similar observation is made for spontaneous BOLD events [72]. These findings indicate that the dynamics of the FC networks are accompanied by simultaneous changes in the intensities of regions in scanned images at different time points. As a consequence, we were motivated to use some image similarity measures to capture these dynamics.

6.2 Algorithm

Our novel adaptive change point detection algorithm is based on concepts of two similarity measures: statistical sign change (SSC) and sum of absolute differences (SAD). In SSC the intensity difference of two images is computed and the change in the signs of the difference is the measure of similarity between the two images [25, 82]. The SSC measure is frequently used in medical image registration [25, 82]. The SAD measure is used in many algorithms for motion detection [100]. In SAD pixels within a square neighborhood of target image are subtracted from the ones in reference image and then the sum of the absolute difference is computed within the square window. If the left and right images exactly match, the resultant sum would be zero.

We hypothesized (based on results of [62, 61, 57, 56, 72]) that in FC networks the change in state or network configuration takes place as a result of change in the signs of the intensities (positive to negative and vice versa) of images at adjacent time points. So, if we compute the difference between the sign changes of adjacent normalized images, and then compute sum of absolute values of these differences then this sum would be largest at the point of maximum sign change. This maximum sign change would reflect the maximum change in the network state or configuration and would give the location of the largest state change. So extracting a number of largest sums of absolute differences would provide the locations of state changes.

We started by representing each scanned image as one column vector of a matrix.

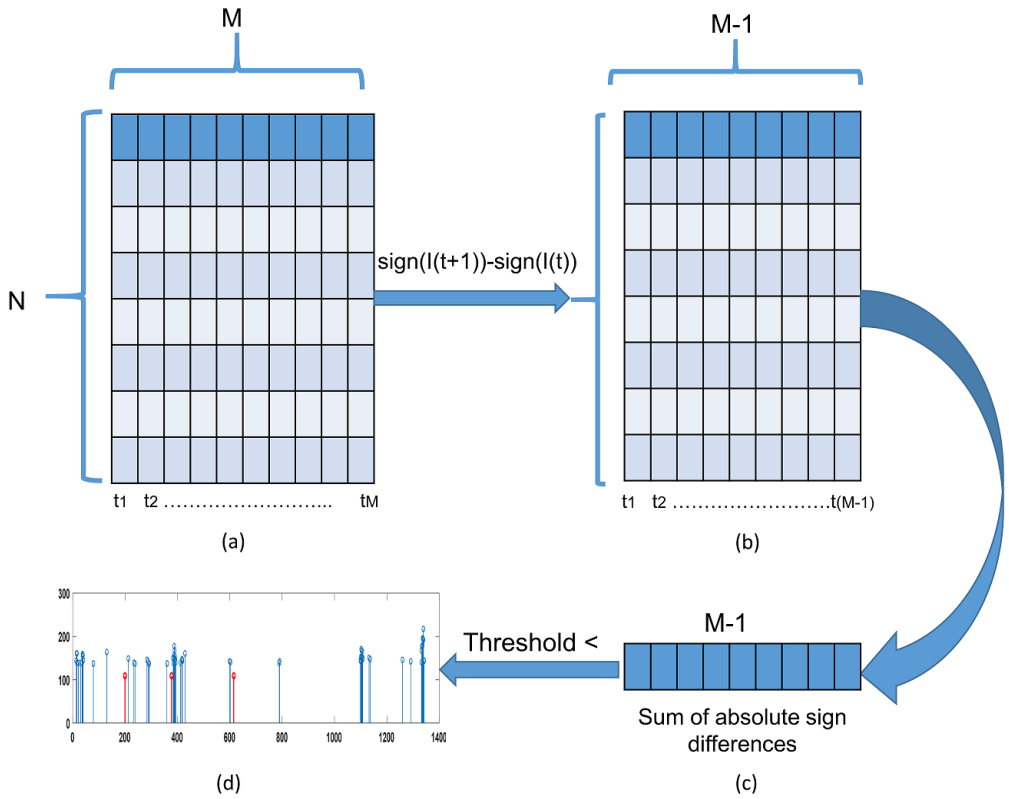

Figure 30: Block diagram of the adaptive change point detection algorithm. (a) Each column of the matrix is one normalized image scanned at that time point. N is total number of voxels in the images and M is the total number of images or time points. (b) Matrix containing the sign difference of two adjacent normalized images (column wise). (c) Absolute values of the sign differences are added. The larger the sum, the more is the difference between the images. (d) Largest sums above certain threshold.

As a result we formed a NxM matrix, in which N is the number of voxels in an image and M is the number of time points (scans or TRs). This would result in M images with N voxels each and the image vector at any time point t can be represented as $X_t = [x_{1t}, x_{2t}, x_{3t}, .., x_{Nt}]'$, $1 \leq t \leq M$. Then we normalized all the images to zero mean and unit variance by using the formula:

$$X'_t = \frac{(X_t - \mu_t)}{S_t}, \tag{39}$$

(μ_t and S_t are sample mean and sample standard deviation of the image at time t). Afterwards, we computed the difference of signs between any two adjacent images.

Similar to the SSC, the change in signs were the indication of the difference for our images. However, in our algorithm we computed the difference of signs (instead of the intensities) between two images at adjacent time points. This process is repeated for the entire scan length. As a result we obtained a Nx$(M-1)$ matrix, in which columns were the sign differences of the adjacent normalized images. Afterwards, we computed the sum of absolute differences of each column (based on the idea of SAD) at each time point. Extraction of a number of largest sums would provide the location of state change points. Once these change points are extracted, the network transitions can be observed by extraction of images around the change points. Our algorithm is very efficient since it uses just sums and differences and is computationally very inexpensive with computational complexity of O(n). Figure 30. shows the block diagram for the sequence of operations in our algorithm.

6.2.1 Pseudo Code

The pseudo code for the algorithm is given below. In this code N is number of images, M is number of time points, $Diff$ is sign difference, and $SumOfDiff$ is sum of absolute of sign differences.

Step 1:
for *t = 1 to M-1* **do**
  for *n = 1 to N* **do**
    Diff(n, t) = sign(x(n, t+1))-sign(x(n, t));
  end
end
Step 2:
for *t=1 to M-1* **do**
  SumOfDiff(:, t) = sum(abs(p(:,t);
end

Algorithm 1: Adaptive network change point detection algorithm

6.3 Results

6.3.1 Simulated Networks

We applied our algorithm on randomly changing simulated networks (SNs) (QPeriodicSN and RandSN from Section 4.2.4) to detect the state change points. The SWC failed to capture the state transitions and durations in these SNs successfully (Figures 20 and 21). Figure 31. shows the results of our change point detection algorithm on these SNs. QPeriodicSN had 14 state transition points and RandSN had 9 of them as shown in GT plots of Figure 31. We computed the sum of differences of images at all time points and plotted the vertical lines (red) at the locations of largest sums. It can be observed that these locations are exactly coinciding with the state transition points of the two SNs showing the success of our algorithm in detecting these transition points. It should be mentioned here that the red vertical bars are not the magnitudes of the actual sums but are plots of equal magnitudes at the location of largest sums. The values of largest sums themselves varied based upon the number of sign differences at the location of state changes, which was an expected result. Our SNs had sharp transitions that may have resulted in ideal state change point detection. So next we applied the algorithm to real fMRI data.

6.3.2 Real Networks (Task)

We applied the proposed algorithm on real data extracted from a vigilance task from an earlier study [91] that was specifically focused on understanding the behavioral performance of individual subjects emerging from interacting brain systems. The resting-state scans of same study was used in Section 3.3., to analyze the state transition of SWC results for different window sizes using t-SNE. The methods for scanning and preprocessing steps were same as mentioned in Section 3.3. We applied the algorithm on the task-based scans first. The reason for using task-based scans was the fact that we had the task onset times available so validation of the algorithm was

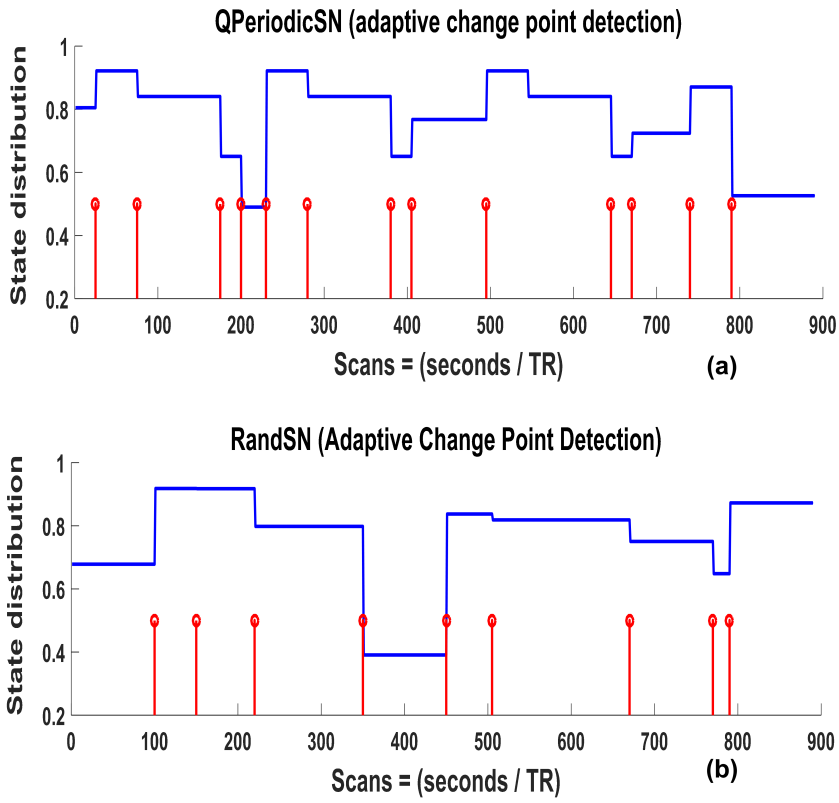

Figure 31: Adaptive change point detection of (a) QPerioidicSN and (b) RandSN. Red vertical lines are positions of the largest change points detected by our algorithm and they align perfectly with the change points of these SNs.

possible. We selected the scans from this specific study since it was a very subtle task (close to resting-state) and we hypothesized that if our algorithm could detect the change points reliably in this task, then it would perform well for resting-state scans too. Figure 32. shows the result of our algorithm on detecting the changes in gray matter area from one run of a subject, selected at random. The red lines show the reaction time (when the subject pressed the button in response to the color change) in response to the task onset.

In both figures the red vertical lines show the reaction time of the task and the blue lines are the largest (a) 5% and (b) 10% sums of absolute differences. We hypothesized that large sums should be present around reaction times. It can be observed that high sums are indeed present around these time points even for the case of 5% largest sums in (a). Another observation that can be made from these figures is the fact that most of the time the sums are present in the form of clusters (green arrows) at adjacent time points. This is again expected since the state transition is a gradual process and would take a few seconds to complete, resulting in large consecutive changes of signs. It can also be seen that these clusters are present even in the absence of any task onset which may be meaningful results (due to the resting-state network transitions at the time when no task is performed) or false positives.

Figure 33. shows the percentage of times the largest 5% sums were within 5 seconds or 8 seconds of the reaction time for eight subjects and twenty four runs. Red horizontal lines show the mean percentages. As expected the mean percentage is higher for detection within 8 seconds of the reaction time. It should be noted here that these plots are only from 5% (65 time points) of the largest sums. Increasing this sum is expected to improve the percentage detection.

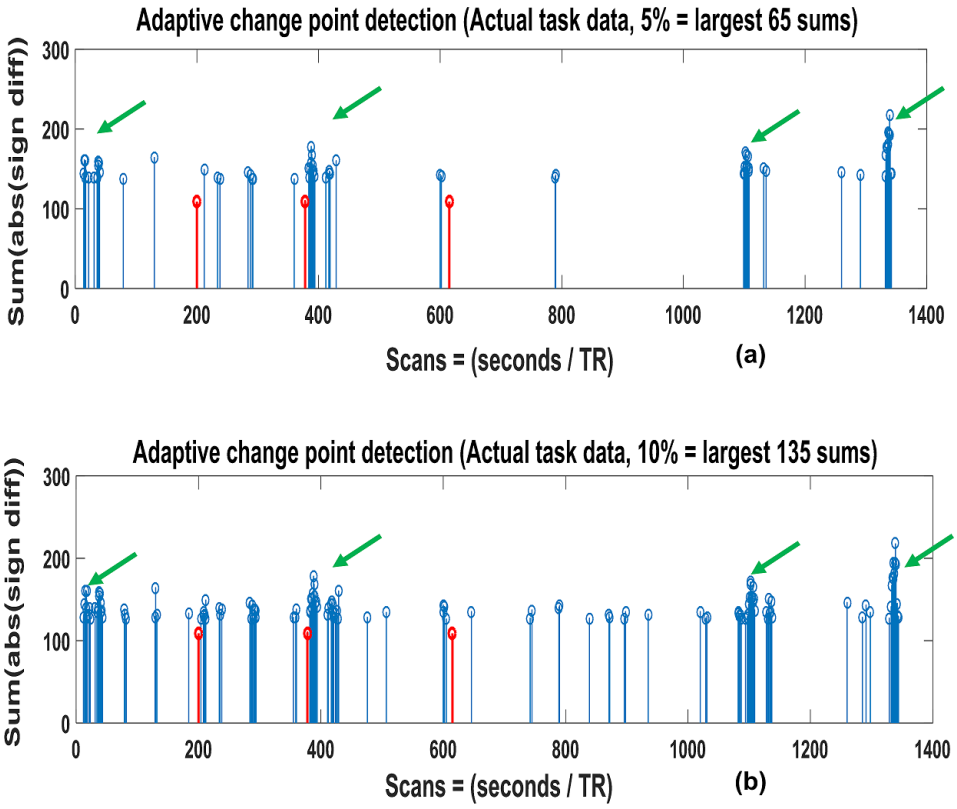

Figure 32: Adaptive change point detection of the vigilance task. Red vertical lines in both figures are the times when the subject reacted in response to the vigilance task. The plots are for (a) 5% largest sums and (b) 10% largest sums. The algorithm was reasonably successful in detecting these times (shown by blue vertical lines around red ones). It should be noted that the large sums occur in cluster (pointed to by green arrows) in which the large changes are taking place at adjacent time points. This is expected based upon the fact that the state changes in real networks are gradual and take few seconds to complete. These clusters are present at location other than the task which may either be due to transitions in resting-state networks or false positives.

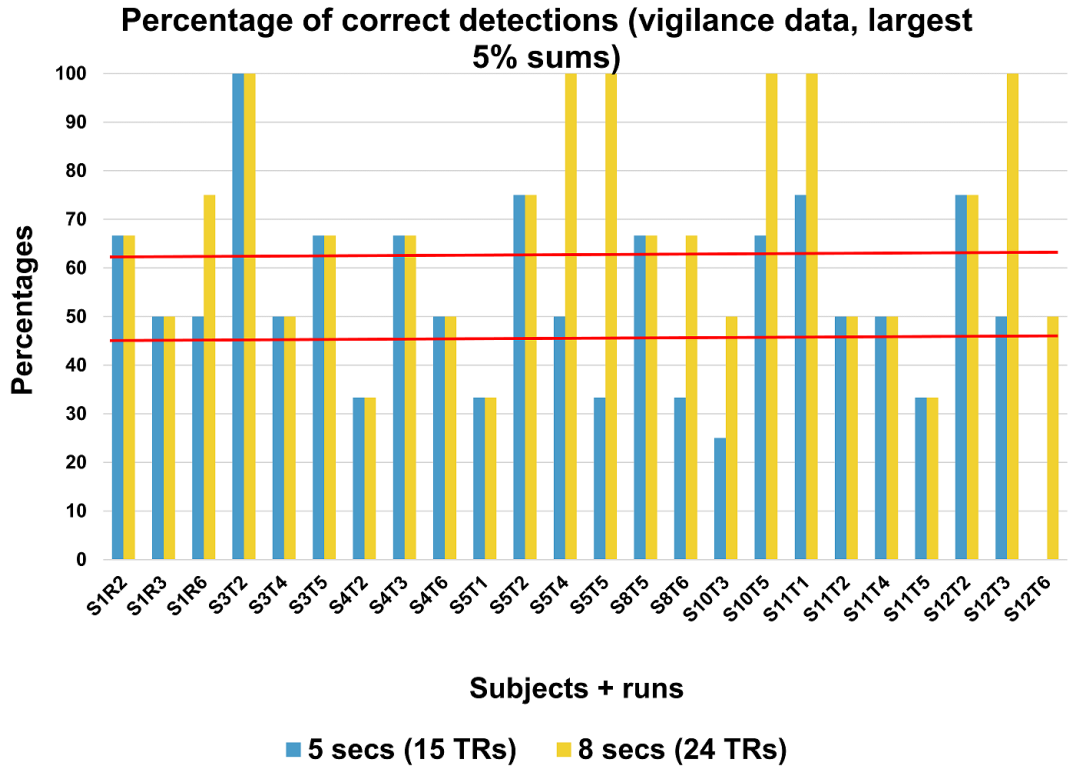

Figure 33: Percentages of correct change point detections in vigilance data. The plots are for the times within 5 and 8 seconds after the reaction in response to the task. The plots are for eight subjects and twenty four runs. The mean correct percentage for 5 seconds is 53% and for 8 seconds is 68% (shown by red horizontal lines). These low percentages maybe due to the fact that vigilance task is very subtle and some of the subjects may not have noticed and fully reacted to the task. It would result in less or no change of networks during next few seconds.

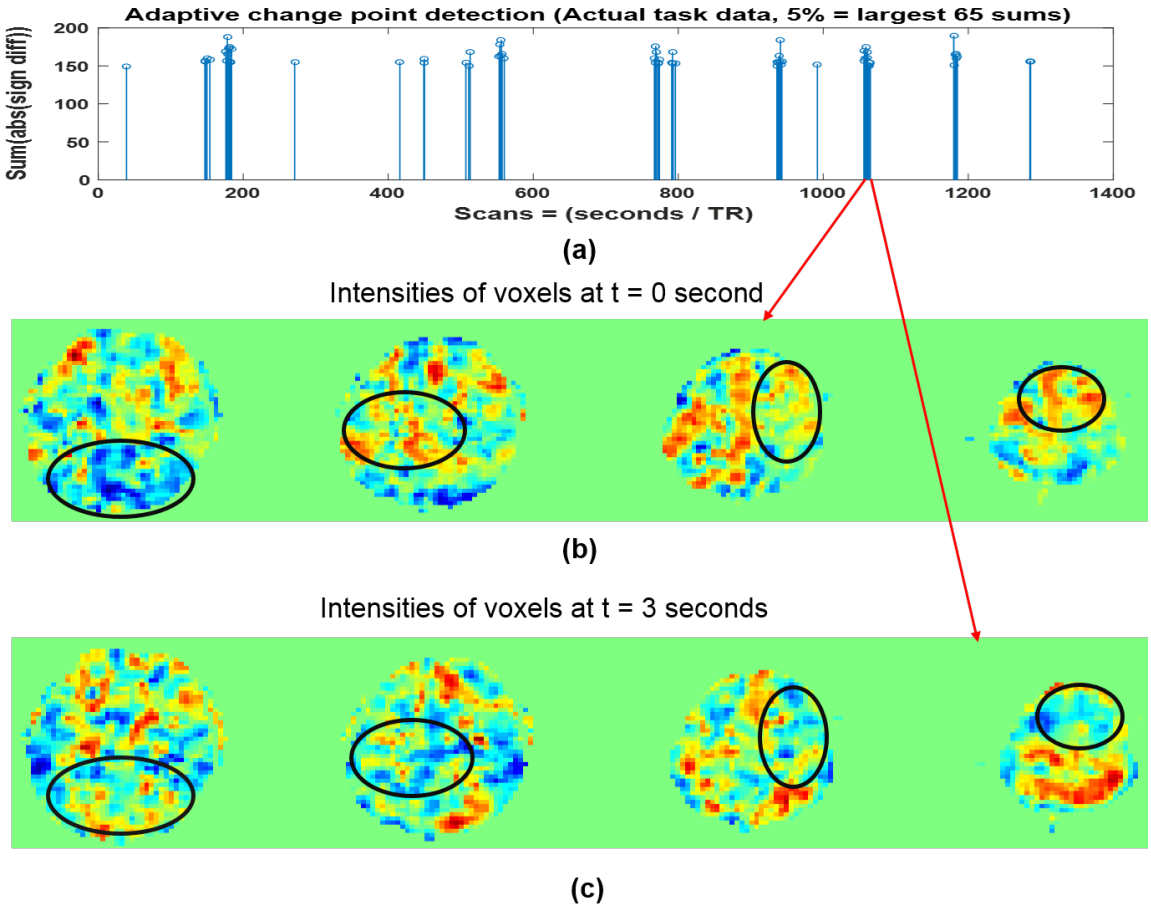

Figure 34: Adaptive change point detection of resting-state network from a randomly chosen subject and run. We picked a cluster of largest sums (shown in (a)), and plotted the four slices at the start and end of this cluster. Total number of scans in this cluster was 9, which was equivalent to 3 seconds. A significant change in the network can be observed during this time (black ovals).

6.3.3 Real Networks (Rest)

As seen from Figure 32. clusters of larges sums of absolute differences were obtained even in the absence of any task, which may be due to the network transitions in resting-brain or false positives. In order to observe if the network is significantly transitioning during these clusters we applied the algorithm on resting-state data from the same study and results for one randomly selected subject is given in Figure 34.

We plotted all four slices at the start and at the end of a cluster of large sums from

(a) in (b) and (c). The start and end of the cluster are pointed to by red lines. It can be observed that there is a significant amount of transition in the network between these two time points (shown by black ovals) that are only three seconds (9 scans) apart.

6.3.4 Limitations and Future Directions

Our adaptive change point detection algorithm is simple and efficient, however, it has a few limitations. It was able to detect the state changes in the subtle vigilance tasks quite reliably but not perfectly. For resting-state networks also these changes were observed, however, lack of ground truth makes it difficult to identify if these changes occurred due to network changes or were false positives. Furthermore, the changes take place in FC networks at all times so there would always be sign differences between any adjacent scanned images. Our algorithm is based on the hypothesis, that the largest sums would indicate the presence of state changes. However, in the absence of any information about the underlying network transitions, there is no way of knowing how many of these largest sums to analyze.

In future, a stronger and well-defined task may be used to observe the success of the algorithm for change point detection. If the algorithm performs better on stronger task that this fact may be used as the validation of the clusters (of sums) in the resting-state as the points of network transitions. In future, some appropriate statistical test may also be employed to test the significance of the results. Future studies can also modify the algorithm to set a threshold on the number of largest sums based on the maximum and minimum sums of absolute differences. Moreover, the algorithm may also be used to differentiate between the detection of change points in groups of healthy controls and patients instead of identification of these points in individual subjects.

6.3.5 Conclusion

Our adaptive change point detection algorithm perfectly detected the sharp state transitions of randomly changing SNs. It was efficient in detecting the change points of networks even when the task was very subtle, and it identified the change points that maybe due to changes in the resting-state networks. With development of appropriate statistical tests the significance of these detected changes can be explored further.

CHAPTER VII

CONCLUSION AND FUTURE WORK

In this study, two major issues of dynamic functional connectivity (dFC) analysis were addressed: (1) The performance evaluation of the sliding window correlation (SWC) and (2) Development of an adaptive change point detection algorithm. The study started with evaluation of SWC results (Chapter 3) and ended by developing a novel algorithm for adaptive change point detection of functional connectivity (FC) networks (Chapter 6). During the course of study concepts and algorithms from the field of signal processing, image processing, video processing, information theory, and machine learning were applied in entirely new ways. Novel applications of Kullback-Leibler (KL) divergence and t-Distributed Stochastic Neighbor Embedding (t-SNE) were introduced in Chapter 3. Chapters 4 and 5 performed extensive analysis of the SWC by processing the signals in time and frequency domains.

7.1 Variability of the FC networks

Spatial extent of the variability in FC networks was analyzed in rodents. A new application of KL divergence to identify the regions with discrete state of FC was introduced. The identification and subsequent extraction of these regions would reduce the unnecessary analysis of the regions that are always part of FC networks. State transitions of the default mode network (DMN) from human data was observed for different window sizes using dimensionality reduction technique, t-SNE, providing visual identification of the results. Both of these applications presented in Chapter 3 would benefit future studies of dFC.

7.2 Performance Evaluation of the SWC

Results form first part of the study motivated us to evaluate the performance of the glsswc method itself. In this part for the study we used the SNs, with controlled state change points that were derived from actual resting-state data. According to the knowledge of the author, it is the first time that the SNs were formed from real resting-state data for this purpose. An extensive analysis of the glsswc performance on these networks provided a comprehensive picture of the SWC as an inefficient dynamic analysis method. Frequency dependence of the window length in the SWC was also evaluated by using sum of sinusoids with multiple frequencies. Both of these studies in Chapter 4. and Chapter 5. reveal the challenges of using the SWC without any GTs, and would be milestones for future studies intending to use the SWC.

7.3 Adaptive Change Point Detection

We used the concepts from similarity measures of stochastic sign change (SSC) and sum of absolute differences (SAD) from image and video processing to develop a new adaptive change point detection algorithm in Chapter 6. This algorithm was perfectly successful in the cases in which the SWC failed for the SNs used in Chapter 4. It worked well for a very subtle vigilance task and identified locations in resting-state networks that may be the change points of these networks. This algorithm is computationally very inexpensive which is its major power. We believe this can be a beneficial addition to the field of neuro dynamics.

7.4 Thesis Contribution

Two major contributions of the study are comprehensive performance evaluation of the SWC (Chapters 4, 5) and development of a new algorithm to detect the change points of functional connectivity (FC) networks adaptively (Chapter 6.) by using the similarly measures from image and video processing. The results from these chapters

can be milestones for future dFC studies. Another important aspect of our study is application of concepts and algorithms from various domains for dFC analysis. These results would encourage future studies to move the focus from finding new ways of applying the same old methods, to linking the dFC analysis to entirely new methodologies from different domains.

7.5 Limitations and Future Work

This study covered dFC from many angles, but there were limitations on each aspect that can be handled in future studies. The first study used anesthetized rats for the study of dynamics, which may have resulted in small extent of variability in the networks. This might be the reason for very few bi- or multi-modal high KL divergence histograms. Future studies can circumvent this issue by using the rsfMRI scans from awake rats or humans. The human part of the study (using t-SNE) could capture the variability range of state transitions for different window length, but it couldn't identify if the transitions were to the same state again and again or to new ones. It also couldn't identify the number of states for any window length. The studies can use some clustering algorithm on raw resting-state networks to identify number of states and label each time point with its state assignment. The application of t-SNE afterwards would identify the pattern of state transitions.

The main limitation of the study using SNs from real resting-state networks was the sharp transitions in these networks. These transitions clearly showed the sensitivity of the SWC to even a single amplitude change but at the same time it may have resulted in perfect state identification of the states in raw data by k-means. Hence, these SNs would be good for performance analysis of the SWC, but may give false positive results as far as state assignment is concerned. In future the studies can form networks from real resting-state data, but with more smooth transitions closer to the actual FC networks' transitions. We used simple sinusoids for exploration

of frequency dependence in the SWC and future studies may explore the frequency dependencies of real resting-state networks.

The adaptive change point detection algorithm presented in this study is very basic but reasonably efficient to detect change points of a subtle vigilance task. It also identified these change points in resting-state networks but it was not evident if they were really network change points or false positives. In future, a stronger and well-defined task may be used to analyze the success of the algorithm. The statistical significance of the results can also be performed to explore if these points are actually the network change points or false positives in case of resting-state networks. Moreover, the algorithm may also be used to differentiate between the detection of change points in groups of healthy controls and patients instead of identification of these points in individual subjects. Future studies can also look into other visual aspects of the rsfMRI scans to develop more robust change point detection algorithms. Future studies can also combine change point detection with adaptive analysis techniques to capture the variabilities of the networks between any two adjacent change points.

Despite the limitations of this study, we believe that our SWC analysis (both using SNs and frequency dependence) would be an excellent guideline for future studies intending to use the SWC in the absence of GTs in any field (e.g. finance, medical, network analysis, and weather trends etc.). We also believe that application of t-Distributed Stochastic Neighbor Embedding (t-SNE) and development of novel adaptive change point detection algorithm would shift the focus to analyze the raw FC networks visually instead of focusing on the results of the SWC.

CHAPTER VIII

APPENDIX A

8.1 Solving for two frequencies

From equation 3, we have

$$c_{xy}[n] = I - II \tag{40}$$

In which,

$$\begin{aligned} I &= (\frac{TR}{w}) \sum_{i=n-\Delta}^{i=n+\Delta} x_i y_i \\ &= (\frac{TR}{w}) \sum_{i=n-\Delta}^{i=n+\Delta} (a+b+c+d) \end{aligned} \tag{41}$$

In which,

$$\begin{aligned} a &= A_1^2 \cos(2\pi f_1 iTR) \cos(2\pi f_2 iTR + \theta) \\ b &= A_2^2 \cos(2\pi f_1 iTR) \cos(2\pi f_2 iTR + \theta) \\ c &= A_1 A_2 \cos(2\pi f_1 iTR) \cos(2\pi f_2 iTR + \theta) \\ d &= A_1 A_2 \cos(2\pi f_2 iTR) \cos(2\pi f_1 iTR + \theta) \end{aligned} \tag{42}$$

and

$$II = \overline{y}_n \overline{x}_n \tag{43}$$

8.1.1 Solving for I

Approximating all the summations by integrations and solving for a, b, c, and d

$$(\frac{TR}{w}) \sum_{i=n-\Delta}^{i=n+\Delta} a = (\frac{A_1^2}{w}) \int_{(n-\Delta-\frac{1}{2})TR}^{(n+\Delta+\frac{1}{2})TR} \cos(2\pi f_1 t) \cos(2\pi f_2 t + \theta) dt \tag{44}$$

Using the trignometric sum and product formulas and integrating, it becomes

$$= (\frac{A_1^2}{2w})\Big[\frac{[\cos(4\pi f_1 nTR+\theta)\sin(2\pi f_1 w)}{4\pi f_1} \; + \; (\frac{A_1^2}{2})\cos(\theta)\Big], \quad since \; w=(2\Delta+1)TR \tag{45}$$

Based on the similar computations, we have

$$(\frac{TR}{w})\sum_{i=n-\Delta}^{i=n+\Delta} b = (\frac{A_2^2}{2w})\Big[\frac{[\cos(4\pi f_2 nTR+\theta)\sin(2\pi f_2 w)}{4\pi f_2} + \; (\frac{A_2^2}{2})\cos(\theta)\Big] \tag{46}$$

Also

$$(\frac{TR}{w})\sum_{i=n-\Delta}^{i=n+\Delta} c = (\frac{A_1A_2}{4\pi w})\Big[\frac{\cos(2\pi f_3 nTR+\theta)\sin(\pi f_3 w)}{f_3} + \frac{\cos(2\pi f_4 nTR+\theta)\sin(\pi f_4 w)}{f_4}\Big] \tag{47}$$

Similarly

$$(\frac{TR}{w})\sum_{i=n-\Delta}^{i=n+\Delta} d = (\frac{A_1A_2}{4\pi w})\Big[\frac{\cos(2\pi f_3 nTR+\theta)\sin(\pi f_3 w)}{f_3} + \frac{\cos(2\pi f_4 nTR-\theta)\sin(\pi f_4 w)}{f_4}\Big] \tag{48}$$

Putting the values of a,b,c, and d we have

$$\begin{aligned} I = {} & \frac{(A_1^2+A_2^2)}{2}\cos(\theta) + (\frac{1}{4\pi w}) \\ & \Big[\frac{A_1^2\cos(4\pi f_1 nTR+\theta)\sin(2\pi f_1 w)}{2f_1} \\ & + \frac{A_2^2\cos(4\pi f_2 nTR+\theta)\sin(2\pi f_2 w)}{2f_2} \\ & + \frac{(2A_1A_2)\cos(2\pi f_3 nTR+\theta)\sin(\pi f_3 w)}{f_3} \\ & + \frac{(A_1A_2)\cos(2\pi f_4 nTR+\theta)\sin(\pi f_4 w)}{f_4} \\ & + \underbrace{\frac{(A_1A_2)\cos(2\pi f_4 nTR-\theta)\sin(\pi f_4 w)}{f_4}}_{\mathrm{C}}\Big] \end{aligned} \tag{49}$$

8.1.2 Solving for II

$$\overline{x}_n = (\frac{TR}{w}) \sum_{i=n-\Delta}^{i=n+\Delta} x_i = (\frac{1}{2\pi w}) \Big[\frac{A_1 \cos(2\pi f_1 nTR) \sin(\pi f_1 w)}{f_1} + \frac{A_2 \cos(2\pi f_2 nTR) \sin(\pi f_2 w)}{f_2} \Big] \tag{50}$$

Similarly

$$\overline{y}_n = (\frac{TR}{w}) \sum_{i=n-\Delta}^{i=n+\Delta} y_i = (\frac{1}{2\pi w}) \Big[\frac{A_1 \cos(2\pi f_1 nTR + \theta) \sin(\pi f_1 w)}{f_1} + \frac{A_2 \cos(2\pi f_2 nTR + \theta) \sin(\pi f_2 w)}{f_2} \Big] \tag{51}$$

So

$$\begin{aligned} II = \overline{y}_n \overline{x}_n = (\frac{A_1 A_2}{4(\pi w)^2}) \Big[& \frac{A_1^2 \cos(2\pi f_1 nTR + \theta) \cos(2\pi f_1 nTR) \sin(\pi f_1 w)^2}{f_1^2} \\ & + \frac{A_2^2 \cos(2\pi f_2 nTR + \theta) \cos(2\pi f_2 nTR) \sin(\pi f_2 w)^2}{f_2^2} \\ & + \frac{A_1 A_2 \sin(\pi f_1 w) \sin(\pi f_2 w)}{f_1 f_2} \\ & [\cos(2\pi f_1 nTR) \cos(2\pi f_2 nTR + \theta) \\ & + \underbrace{\cos(2\pi f_2 nTR) \cos(2\pi f_2 nTR + \theta)]}_{\mathrm{D}} \Big] \end{aligned} \tag{52}$$

8.2 Solving for multiple frequencies

For sinusoids with m frequencies and amplitudes (18) we compute the covariance $c_{xy}[n]$ by solving for (I) and (II) from Equation (3):

8.2.1 Solving for I

$$I = (\frac{TR}{w}) \sum_{i=n-\Delta}^{i=n+\Delta} x_i y_i \tag{53}$$

In which

$$
\begin{aligned}
x_i y_i &= \left\{ \sum_{j=1}^{m} A_j \cos(2\pi f_j iTR) \right\} \left\{ \sum_{k=1}^{m} A_k \cos(2\pi f_k iTR + \theta) \right\} \\
&= \sum_{j=1}^{m} \sum_{k=1}^{m} A_j A_k \cos(2\pi f_j iTR) \cos(2\pi f_k iTR + \theta) \\
&= \sum_{j=1}^{m} \frac{A_j^2}{2} \cos(2\pi f_j iTR) \cos(2\pi f_j iTR + \theta) \\
&+ \sum_{k=1}^{m} A_k \cos(2\pi f_k iTR) \sum_{\substack{l=1 \\ l \neq k}}^{m} A_l \cos(2\pi f_l iTR + \theta)
\end{aligned} \tag{54}
$$

So we have:

$$
\begin{aligned}
I &= (\frac{TR}{w}) \sum_{i=n-\Delta}^{i=n+\Delta} \left\{ \sum_{j=1}^{m} \frac{A_j^2}{2} \cos(2\pi f_j iTR) \cos(2\pi f_j iTR + \theta) \right\} \\
&+ (\frac{TR}{w}) \sum_{i=n-\Delta}^{i=n+\Delta} \left\{ \sum_{k=1}^{m} A_k \cos(2\pi f_k iTR) \sum_{\substack{l=1 \\ l \neq k}}^{m} A_l \cos(2\pi f_l iTR + \theta) \right\} \\
&= \sum_{j=1}^{m} \frac{A_j^2}{2} \int_{(n-\Delta-\frac{1}{2})TR}^{(n+\Delta+\frac{1}{2})TR} \cos(2\pi f_j t) \cos(2\pi f_j t + \theta) dt \\
&+ \sum_{k=1}^{m} A_k \sum_{\substack{l=1 \\ l \neq k}}^{m} A_l \int_{(n-\Delta-\frac{1}{2})TR}^{(n+\Delta+\frac{1}{2})TR} \cos(2\pi f_k iTR) \cos(2\pi f_l iTR + \theta) dt
\end{aligned} \tag{55}
$$

After integrating, applying limits and using trigonometric identities (similar to two frequency case in Section (8.1) we have :

$$
\begin{aligned}
I = & \sum_{j=1}^{m} \frac{A_j^2}{2} \cos(\theta) \\
& + (\frac{1}{8\pi w}) \underbrace{\sum_{j=1}^{m} \frac{A_j^2}{f_j} \cos(4\pi f_j nTR + \theta) \sin(2\pi w f_j)}_{\text{E}} \\
& + (\frac{1}{2\pi w f_{k+l}}) \underbrace{\sum_{l=1}^{m-1} A_l \sum_{k=l+1}^{m} A_k \cos(2\pi f_{k+l} nTR + \theta) \sin(\pi w f_{k+l})}_{\text{F}} \\
& + (\frac{1}{4\pi w f_{k-l}}) \underbrace{\left\{ \sum_{l=1}^{m-1} A_l \sum_{k=l+1}^{m} A_k \left\{ \cos(\phi + \theta) - \cos(\phi - \theta) \right\} \sin(\pi w f_{k-l})^2 \right\}}_{\text{G}}
\end{aligned}
\tag{56}
$$

in which $f_{k+l} = f_k + f_l$, $f_{k-l} = f_k - f_l$ *and* $\phi = 2\pi f_{k-l} nTR$

For sanity check let us let m=2, then

$$
\begin{aligned}
I = & \sum_{j=1}^{2} \frac{A_j^2}{2} \cos(\theta) \\
& + (\frac{1}{8\pi w}) \underbrace{\sum_{j=1}^{2} \frac{A_j^2}{f_j} \cos(4\pi f_j nTR + \theta) \sin(2\pi w f_j)}_{\text{E}} \\
& + (\frac{1}{2\pi w f_{k+l}}) \underbrace{\sum_{l=1}^{1} A_l \sum_{k=l+1}^{2} A_k \cos(2\pi f_{k+l} nTR + \theta) \sin(\pi w f_{k+l})}_{\text{F}} \\
& + (\frac{1}{4\pi w f_{k-l}}) \underbrace{\left\{ \sum_{l=1}^{1} A_l \sum_{k=l+1}^{2} A_k \sin(\pi w f_{k-l} \left\{ \cos(\phi + \theta) - \cos(\phi - \theta) \right\}) \right\}}_{\text{G}}
\end{aligned}
\tag{57}
$$

in which $f_{k+l} = f_k + f_l$, $f_{k-l} = f_k - f_l$ *and* $\phi = 2\pi f_{k-l} nTR$

Further simplification of the above equation would give the same result as 49.

8.2.2 Solving for II

$$\begin{aligned}\overline{x}_n &= (\frac{TR}{w}) \sum_{i=n-\Delta}^{i=n+\Delta} x_i \\ &= (\frac{TR}{2\pi w}) \left\{ \sum_{j=1}^{m} \frac{A_j}{f_j} \cos(2\pi f_j nTR) \sin(\pi f_j w) \right\}\end{aligned} \tag{58}$$

Similarly

$$\begin{aligned}\overline{y}_n &= (\frac{TR}{w}) \sum_{i=n-\Delta}^{i=n+\Delta} y_i \\ &= (\frac{TR}{2\pi w}) \left\{ \sum_{j=1}^{m} \frac{A_j}{f_j} \cos(2\pi f_j nTR + \theta) \sin(\pi f_j w) \right\}\end{aligned} \tag{59}$$

So

$$\begin{aligned}II &= \overline{y}_n \overline{x}_n \\ &= (\frac{TR^2}{4\pi^2 w^2}) \\ &\underbrace{\left\{ \sum_{j=1}^{m} \frac{A_j}{f_j} \sum_{k=1}^{m} \frac{A_k}{f_k} \cos(2\pi f_j nTR) \cos(2\pi f_k nTR + \theta) \sin(\pi f_j w) \sin(\pi f_k w) \right\}}_{\text{H}}\end{aligned} \tag{60}$$

Glossary

AWGN additive white gaussian noise. xv, 63, 79, 80, 88

BOLD blood-oxygen-level-dependent. 5, 9, 13, 24, 40, 42, 47, 55, 82, 93, 112, 113

CP caudate putamen. 19, 23, 29, 32, 34, 41, 43

DCC dynamic conditional correlation. 15, 16

dFC dynamic functional connectivity. vi, 3–9, 12–15, 17–20, 24, 26, 30, 35, 36, 44–46, 54, 55, 124, 126

DI Dunn's Index. 28, 36

DMN default mode network. xiii, 10, 13, 16, 40, 48, 52, 56–59, 65, 112, 124

EPI echo planar imaging. 21, 47

FC functional connectivity. vi, ix, 1–10, 12–20, 23, 24, 26, 28–32, 34–38, 40–44, 53, 54, 59, 60, 63, 64, 74, 82, 84–86, 91, 93, 112, 113, 122, 124–127

fMRI functional MRI. 1

GT ground truth. 1, 2, 4, 5, 7–9, 14, 16, 17, 52, 55, 61, 64, 69, 92, 116, 125, 127

ICA independent component analysis. 10, 13, 15

KL Kullback-Leibler. xii, 6, 20, 23, 28, 29, 38, 39, 42–44, 49, 124, 126

LCP left caudate putamen. xi, xii, 22, 23, 30–32, 34–37, 40

LFF low frequency fluctuations. 9

LFP local field potential. 24

LS1 left somatosensory cortex. xi, xii, 22, 23, 30–32, 34–37, 39, 40

MAC multiplicative analytical coupling. 15, 16

PVT psychomotor vigilance task. 46

QPP quasi-periodic patterns. 4, 5, 13, 15, 16, 112

RCP right caudate putamen. 22, 30, 32, 36, 38, 40

ROI region of interest. vii, xiii, 10, 14, 19, 20, 22, 23, 28, 29, 46–48, 57–59, 61, 63, 65

RS1 right somatosensory cortex. xii, 22, 31, 32, 36, 37, 40

rsfMRI resting-state functional MRI. 2, 4, 5, 9, 10, 14, 55–57, 59, 63, 64, 84–86, 88–94, 96, 101, 107, 110, 112, 126, 127

RSN resting-state network. 9, 10

S1 primary somatosensory cortex. 19, 21, 23, 29, 32, 34, 41, 43

SAD sum of absolute differences. 7, 113, 115, 125

SN simulated network. x, xiii, xiv, xvi, 2, 6–8, 54, 55, 57, 59–65, 68, 69, 71, 72, 74, 75, 77–79, 82, 84–92, 116, 117, 123, 125–127

SNR signal-to-noise ration. viii, xv, 23, 63, 79, 80, 88

SSC stochastic sign change. 7, 113, 115, 125

SWC sliding window correlation. viii, ix, xiii–xv, 2–9, 15–20, 23, 24, 28, 29, 32, 38, 44, 45, 47, 48, 52–55, 57, 60, 61, 63–70, 72–74, 77, 79–94, 96, 101, 110–112, 116, 124–127

t-SNE t-Distributed Stochastic Neighbor Embedding. vii, 6, 44–46, 48–50, 52, 53, 116, 124, 126, 127

TPN task-positive network. xi, 10, 11, 14, 16, 112

TR repetition time. x–xv, 4, 19, 22, 24, 25, 44, 46–48, 50–52, 56, 59, 60, 62, 63, 65, 67, 68, 72–81, 83, 86, 88–90

REFERENCES

[1] Albert, N., Robertson, E., and Miall, R., "The resting human brain and motor learning," *Curr Biol*, vol. 19, no. 12, pp. 1023–7, 2009.

[2] Allen, A., Damaraju, E., Plis, S., and others, "Tracking whole-brain connectivity dynamics in the resting state," *Cerebral Cortex*, vol. 24, no. 3, pp. 663–76, 2014.

[3] Bajaj, S., Adhikari, B., and Dhamala, M., "Higher frequency network activity flow predicts lower frequency node activity in intrinsic low-frequency bold fluctuations," *PLoS ONE*, vol. 8, no. 5, 2013.

[4] Berman, G., Choi, D., Bialek, W., and Shaevitz, J., "Mapping the stereotyped behaviour of freely moving fruit flies," *J R Soc Interface.*, vol. 11, no. 99, 2014.

[5] Birn, R., "The role of physiological noise in resting-state functional connectivity," *Neuroimage*, vol. 62, p. 864870, 2012.

[6] Biswal, B., Yetkin, F., Haughton, V., and Hyde, J., "Functional connectivity in the motor cortex of resting human brain using echo-planar mri," *Magn Reson Med*, vol. 34, pp. 537–41, 1995.

[7] Biswal, B., Van, K., and Hyde, J., "Simultaneous assessment of flow and bold signals in resting-state functional connectivity maps," *NMR Biomed*, vol. 10, pp. 165–70, 1997.

[8] Bluhm, R., Miller, J., Lanius, R., and others, "Spontaneous low-frequency fluctuations in the bold signal in schizophrenic patients: Anomalies in the default network," *Schizophr Bull*, vol. 33, no. 4, pp. 1004–12, 2007.

[9] Bright, M. and Murphy, K., "Is fMRI "noise" really noise? Resting state nuisance regressors remove variance with network structure," *NeuroImage*, vol. 114, pp. 158–69, 2015.

[10] Buckner, R., Andrews, H., Jessica, R., and Schacter, D., "The brains default network," *Annals of the New York Academy of Sciences*, vol. 1124, no. 1, pp. 1–38, 2008.

[11] Buckner, R., Sepulcre, J., Talukdar, T., and others, "Cortical hubs revealed by intrinsic functional connectivity: mapping, assessment of stability, and relation to alzheimer's disease," *J Neurosci*, vol. 29, no. 6, pp. 1860–73, 2009.

[12] Calhoun, V., Adali, T., Hansen, L., and others, "Ica of functional mri data: An overview," in *Proceedings of the International Workshop on Independent Component Analysis and Blind Signal Separation*, 2003.

[13] Calhoun, V., Maciejewski, P., Pearlson, G., and Kiehl, K., "Temporal lobe and "default" hemodynamic brain modes discriminate between schizophrenia and bipolar disorder," *Hum Brain Mapp*, vol. 29, no. 11, pp. 1265–75, 2008.

[14] Chang, C. and Glover, G., "Time-frequency dynamics of resting-state brain connectivity measured with fmri," *NeuroImage*, vol. 50, no. 1, pp. 81–98, 2010.

[15] Chang, C., Liu, Z., Chen, M., and others, "Eeg correlates of time-varying bold functional connectivity," *NeuroImage*, vol. 15, no. 72, pp. 227–36, 2013.

[16] Chow, H., Horovitz, S., Carr, W., and others, "Rhythmic alternating patterns of brain activity distinguish rapid eye movement sleep from other states of consciousness," *Proc Natl Acad Sci U S A*, vol. 110, no. 25, pp. 10300–05, 2013.

[17] Cordes, D., Haughton, V., Arfanakis, K., and others, "Mapping functionally related regions of brain with functional connectivity mr imaging," *AJNR Am J Neuroradiol*, vol. 21, pp. 1636–44, 2000.

[18] Cordes, D., Haughton, V., Arfanakis, K., and others, "Frequencies contributing to functional connectivity in the cerebral cortex in "resting-state" data," *AJNR Am J Neuroradiol.*, vol. 22, no. 7, pp. 1326–33, 2001.

[19] Cribben, I., Haraldsdottir, R., Atlas, L., and others, "Dynamic connectivity regression: determining state-related changes in brain connectivity," *NeuroImage*, vol. 61, no. 4, pp. 907–20, 2012.

[20] Damaraju, E., Allen, E., Belgerc, A., and others, "Dynamic functional connectivity analysis reveals transient states of dysconnectivity in schizophrenia," *NeuroImage: Clinical*, vol. 5, pp. 298–308, 2014.

[21] Damoiseaux, J., Rombouts, S., Barkhof, F., and others, "Consistent resting-state networks across healthy subjects," *Proc Natl Acad Sci*, vol. 103, no. 37, pp. 3848–53, 2006.

[22] Esposito, F., Bertolino, A., Scarabino, T., and others, "Independent component model of the default-mode brain function: Assessing the impact of active thinking," *Brain Res Bull*, vol. 70, no. 4-6, pp. 263–9, 2006.

[23] Fox, M., Snyder, A., Vincent, J., and others, "The human brain is intrinsically organized into dynamic, anticorrelated functional networks," *Proc Natl Acad Sci*, vol. 102, no. 27, pp. 9673–8, 2005.

[24] Gonzalez-Castillo, J., Handwerker, D., Robinson, M., and others, "The spatial structure of resting state connectivity stability on the scale of minutes," *Front. Neurosci.*, vol. 8, no. 138, 2014.

[25] Goshtasby, A., *Image Registration: Principles, Tools and Methods*. Springer, 2011.

[26] Greicius, M., "Resting-state functional connectivity in neuropsychiatric disorders," *Curr Opin Neurol.*, vol. 21, no. 4, pp. 424–30, 2008.

[27] Greicius, M., Krasnow, B., Reiss, A., and Menon, V., "Functional connectivity in the resting brain: A network analysis of the default mode hypothesis," *Proc Natl Acad Sci U S A*, vol. 100, no. 1, pp. 1253–8, 2003.

[28] Greve, D., Brown, G., Bryon, A., and others, "A survey of the sources of noise in fmri," *Psychometrika*, vol. 78, no. 3, pp. 396–416, 2013.

[29] Grigg, O. and Grady, C., "Task-related effects on the temporal and spatial dynamics of resting-state functional connectivity in the default network," *PLoS One*, vol. 5, no. 10, 2010.

[30] Halkidi, M. and Batistakis, Yand Vazirgiannis, M., "Clustering validity checking methods: part ii," *ACM SIGMOD Record*, vol. 31, pp. 19–27, 2000.

[31] Halkidi, M., Batistakis, Y., and Vazirgiannis, M., "On clustering validation techniques," *Journal of Intelligent Information Systems*, vol. 17, pp. 107–145, 2001.

[32] Handwerker, D., Roopchansingh, V., Gonzalez-Castillo, J., and Bandettini, P., "Periodic changes in fmri connectivity," *NeuroImage*, vol. 63, no. 3, pp. 1712–9, 2012.

[33] Hindriks, R., Adhikari, M., Murayama, Y., and others, "Can sliding-window correlations reveal dynamic functional connectivity in resting-state fMRI?," *NeuroImage*, vol. 127, pp. 242–56, 2015.

[34] Honey, C., Sporns, O., Cammoun, L., and others, "Predicting human resting-state functional connectivity from structural connectivity," *Proc Natl Acad Sci U S A*, vol. 106, no. 6, pp. 2035–40, 2008.

[35] Horovitz, S., Fukunaga, M., de Zwart, J., and others, "Low frequency bold fluctuations during resting wakefulness and light sleep: A simultaneous eeg-fmri study," *Hum Brain Mapp*, vol. 29, no. 6, pp. 671–82, 2008.

[36] Hutchison, R., Womelsdorf, T., Allen, E., and others, "Dynamic functional connectivity: Promise, issues, and interpretations," *NeuroImage*, vol. 80, pp. 360–78, 2013.

[37] Hutchison, R., Womelsdorf, T., Gati, J., and others, "Resting-state networks show dynamic functional connectivity in awake humans and anesthetized macaques," *Hum Brain Mapp*, vol. 34, no. 9, pp. 2154–77, 2013.

[38] Jia, H., Hu, X., and Deshpande, G., "Behavioral relevance of the dynamics of the functional brain connectome," *Brain Connect*, vol. 4, no. 9, pp. 741–59, 2014.

[39] Johnston, J., Vaishnavi, S., Smyth, M., and others, "Loss of resting interhemispheric functional connectivity after complete section of the corpus callosum," *J Neurosci*, vol. 28, no. 25, pp. 6453–8, 2008.

[40] Jones, D., Vemuri, P., Murphy, M., and others, "Non-stationarity in the resting brains modular architecture," *PLoS One*, vol. 7, no. 6, 2012.

[41] Keilholz, S., "The neural basis of time-varying resting-state functional connectivity," *Brain Connect.*, vol. 4, no. 10, pp. 769–79, 2014.

[42] Keilholz, S., Magnuson, M., Pan, W.-J., and others, "Dynamic properties of functional connectivity in the rodent," *Brain Connectivity*, vol. 3, no. 1, pp. 31–40, 2013.

[43] Kiviniemi, V., Vire, T., Remes, J., and others, "A sliding time-window ica reveals spatial variability of the default mode network in time," *Brain Connectivity*, vol. 1, no. 4, pp. 339–47, 2011.

[44] Kruger, G. and Glover, G., "Physiological noise in oxygenation-sensitive magnetic resonance imaging," *Magn Reson Med*, vol. 46, pp. 631–37, 2001.

[45] Kucyi, A. and Davis, K., "Dynamic functional connectivity of the default mode network tracks daydreaming," *Neuorimage*, vol. 15, no. 100, pp. 471–80, 2014.

[46] Laufs, H., Krakow, K., Sterzer, P., and others, "Electroencephalographic signatures of attentional and cognitive default modes in spontaneous brain activity fluctuations at rest," *Proc Natl Acad Sci*, vol. 100, pp. 11053–58, 2003.

[47] Lee, J. and Verleysen, M., "On the role and impact of the metaparameters in t-distributed stochastic neighbor embedding," in *Proceedings of the 19th International Conference on Computational Statistics*, pp. 337–46, COMPSTAT, 2010.

[48] Lee, M., Hacker, C., Snyder, A., and others, "Clustering of resting state networks," *PLoS One*, vol. 7, 2012.

[49] Lee, M., Smyser, C., and Shimony, J., "Resting-state fmri: a review of methods and clinical applications," *AJNR Am J Neuroradiol*, vol. 34, no. 10, pp. 1866–72, 2013.

[50] Leonardi, N., Richiardi, J., and an De Ville, D., "Functional connectivity eigennetworks reveal different brain dynamics in multiple sclerosis patients," in *Proceedings of the International Symposium on Biomedical Imaging*, vol. 83, pp. 528–31, IEEE, 2013.

[51] Leonardi, N., Richiardi, J., Gschwind, M., and others, "Principal components of functional connectivity: A new approach to study dynamic brain connectivity during rest," *NeuroImage*, vol. 83, p. 937950, 2013.

[52] Leonardi, N., Shirer, W., Greicius, M., and Van De Ville, D., "Disentangling dynamic networks: Separated and joint expressions of functional connectivity patterns in time," *Hum Brain Mapp*, vol. 35, no. 12, pp. 5984–95, 2014.

[53] Leonardi, N. and Van De Ville, D., "On spurious and real fluctuations of dynamic functional connectivity during rest," *NeuroImage*, vol. 104, no. 1, pp. 430–6, 2015.

[54] Li, X., Zhu, D., Jiang, X., and others, "Dynamic functional connectomics signatures for characterization and differentiation of ptsd patients," *Hum Brain Mapp*, vol. 35, no. 4, pp. 1761–78, 2014.

[55] Lindquist, M., Xu, Y., Nebel, M., and Caffo, B., "Evaluating dynamic bivariate correlations in resting-state fmri: a comparison study and a new approach," *NeuroImage*, vol. 101, pp. 531–46, 2014.

[56] Liu, X., Chang, K., and Duyn, J., "Decomposition of spontaneous brain activity into distinct fmri co-activation patterns," *Front. Syst. Neurosci.*, 2013.

[57] Liu, X. and Duyn, J., "Time-varying functional network information extracted from brief instances of spontaneous brain activity," *Proc Natl Acad Sci*, vol. 110, no. 11, pp. 4392–7, 2013.

[58] MacQueen, J., "Some methods for classification and analysis of multivariate observations," in *Proceedings of the Fifth Berkeley Symposium on Mathematical Statistics and Probability*, pp. 281–97, Berkeley Symp. on Math. Statist. and Prob, 1967.

[59] Magnuson, M., Majeed, W., and Keilholz, S., "Functional connectivity in bold and cbv weighted resting state fmri in the rat brain," *J Magn Reson Imag*, vol. 32, no. 3, pp. 584–92, 2010.

[60] Magnuson, M., Thompson, G., Majeed, W., and others, "Time-dependent effects of isoflurane and dexmedetomidine on functional connectivity, spectral characteristics, and spatial distribution of spontaneous bold fluctuations," *NMR Biomed.*, vol. 27, no. 3, pp. 291–303, 2014.

[61] Majeed, W., Magnuson, M., Hasenkamp, W., and others, "Spatiotemporal dynamics of low frequency bold fluctuations in rats and humans," *NeuroImage*, vol. 54, no. 2, pp. 1140–50, 2011.

[62] Majeed, W., Magnuson, M., and Keilholz, S., "Spatiotemporal dynamics of low frequency bold fluctuations in rats," *J Magn Reson Imaging*, vol. 30, no. 2, pp. 384–393, 2009.

[63] Maldjian, J., Laurienti, P., Kraft, R., and others, "An automated method for neuroanatomic and cytoarchitectonic atlas-based interrogation of fmri data sets," *NeuroImage*, vol. 19, pp. 1233–39, 2003.

[64] Martuzzi, R., Ramani, R., Qiu, M., and others, "Functional connectivity and alterations in baseline brain state in humans," *NeuroImage*, vol. 49, no. 1, pp. 823–34, 2009.

[65] McKeown, M., Makeig, S., Brown, G., and others, "Analysis of fmri data by blind separation into independent spatial components," *Hum Brain Mapp*, vol. 6, pp. 160–88, 1998.

[66] Miller, K., Weaver, E., and Ojemann, J., "Direct electrophysiological measurement of human default network areas.," *Proc Natl Acad Sci*, vol. 106, no. 29, p. 12174177, 2009.

[67] Ogawa, S., Lee, T., Kay, A., and Tank, D., "Brain magnetic resonance imaging with contrast dependent on blood oxygenation," *Proc Natl Acad Sci*, vol. 87, pp. 9868–72, 1990.

[68] Pan, W., Thompson, G., Magnuson, M., and others, "Broadband local field potentials correlate with spontaneous fluctuations in functional magnetic resonance imaging signals in the rat somatosensory cortex under isoflurane anesthesia," *Brain Connect.*, vol. 1, no. 2, pp. 119–31, 2011.

[69] Pan, W., Thompson, G., Magnuson, M., and others, "Simultaneous fmri and electrophysiology in the rodent brain.," *J Vis Exp.*, vol. 19, no. 42, 2010.

[70] Pan, W., Thompson, G., Magnuson, M., and others, "Infraslow lfp correlates to resting-state fmri bold signals.," *NeuroImage*, vol. 74, pp. 288–97, 2013.

[71] Pawela, C., Biswal, B., Cho, Y., and others, "Resting-state functional connectivity of the rat brain," *Magn Reson Med*, vol. 59, no. 5, pp. 1021–9, 2008.

[72] Petridou, N., Gaudes, C., Dryden, I., and others, "Periods of rest in fmri contain individual spontaneous events which are related to slowly fluctuating spontaneous activity," *Human Brain Mapping*, vol. 34, no. 6, pp. 1319–1329, 2013.

[73] Raichle, M., MacLeod, A., Snyder, A., and others, "A default mode of brain function," *Proc Natl Acad Sci*, vol. 98, no. 2, pp. 676–82, 2001.

[74] Rombouts, S., Barkhof, F., Goekoop, R., and others, "Altered resting state networks in mild cognitive impairment and mild alzheimer's disease: an fmri study.," *Hum Brain Mapp.*, vol. 26, no. 4, pp. 231–9, 2005.

[75] Rousseeuw, P., "Silhouettes: A graphical aid to the interpretation and validation of cluster analysis," *Journal of Computational and Applied Mathematics*, vol. 20, pp. 53–65, 1987.

[76] Sadaghiani, S., Poline, J., Kleinschmidt, A., and D'Esposito, M., "Ongoing dynamics in large-scale functional connectivity predict perception.," *Proc Natl Acad Sci*, vol. 112, no. 27, pp. 8463–8, 2015.

[77] Sakolu, U., Pearlson, G., Kiehl, K., and others, "A method for evaluating dynamic functional network connectivity and task-modulation: application to schizophrenia," *MAGMA*, vol. 23, pp. 351–66, 2010.

[78] Schulz, D. and Huston, J., "The sliding window correlation procedure for detecting hidden correlations: existence of behavioral subgroups illustrated with aged rats," *J Neurosci Methods*, vol. 121, no. 2, pp. 129–37, 2002.

[79] Shakil, S., Keilholz, S., and Lee, C.-H., "On frequency dependencies of sliding window correlation," in *International Conference of Bioinformatics and Biomedicine*, IEEE, 2015.

[80] Shakil, S., Keilholz, S., and Lee, C.-H., "Evaluation of sliding window correlation performance for characterizing dynamic functional connectivity and brain states," *NeuroImage*, vol. 133, pp. 111–28, 2016.

[81] Shakil, S., Magnuson, M., Keilholz, S., and Lee, C.-H., "Cluster-based analysis for characterizing dynamic functional connectivity," in *Conf Proc IEEE Eng Med Biol Soc. 2014*, pp. 982–985, IEEE, 2014.

[82] Shields, K., Barber, D., and Sherriff, S., "Image registration for the investigation of atherosclerotic plaque movement," *Lecture Notes in Computer Science*, vol. 687, pp. 438–58, 1993.

[83] Shine, J., Oluwasanmi, K., Bell, P., and others, "Estimation of dynamic functional connectivity using multiplicative analytical coupling," *NeuroImage*, vol. 122, pp. 399–407, 2015.

[84] Shirer, W., Ryali, S., Rykhlevskaia, E., and others, "Decoding subject-driven cognitive states with whole-brain connectivity patterns," *Cereb Cortex.*, vol. 22, no. 1, pp. 158–65, 2012.

[85] Shmuel, A. and Leopold, D., "Neuronal correlates of spontaneous fluctuations in fmri signals in monkey visual cortex: implications for functional connectivity at rest," *Hum Brain Mapp*, vol. 29, pp. 751–61, 2008.

[86] Smith, S., Fox, P., Miller, K., and others, "Correspondence of the brain's functional architecture during activation and rest.," *Proc Natl Acad Sci*, vol. 106, no. 31, pp. 13040–5, 2009.

[87] Smith, S., Miller, K., Moeller, S., and others, "Temporally-independent functional modes of spontaneous brain activity," *Proc Natl Acad Sci*, vol. 109, no. 8, pp. 3131–36, 2012.

[88] Sorg, C., Riedl, V., Mhlau, M., and others, "Selective changes of resting-state networks in individuals at risk for alzheimer's disease," *Proc Natl Acad Sci*, vol. 104, no. 47, pp. 18760–5, 2007.

[89] Stein, T., Moritz, C., Quigley, M., and others, "Functional connectivity in the thalamus and hippocampus studied with functional mr imaging," *AJNR Am J Neuroradiol*, vol. 21, no. 8, pp. 1397–401, 2000.

[90] Tagliazucchi, E., von Wegner, F., Morzelewski, A., and others, "Dynamic BOLD functional connectivity in humans and its electrophysiological correlates," *Front Hum Neurosci*, vol. 6, p. 339, 2012.

[91] Thompson, G., Magnuson, M., Merritt, M., and others, "Short time windows of correlation between large scale functional brain networks predict vigilance intra-individually and inter-individually," *Hum Brain Mapping*, vol. 34, no. 12, pp. 3280–98, 2013.

[92] Thompson, G., Merritt, M., Pan, W.-J., and others, "Neural correlates of time-varying functional connectivity in the rat," *NeuroImage*, vol. 83, pp. 826–36, 2013.

[93] Thompson, G., Pan, W.-J., Billings, J., and others, "Phase-amplitude coupling and infraslow (¡1 hz) frequencies in the rat brain: relationship to resting state fmri.," *Front Integr Neurosci.*, vol. 8, no. 41, 2014.

[94] Thompson, G., Pan, W.-J., Magnuson, M., and others, "Quasi-periodic patterns (QPP): large-scale dynamics in resting state fMRI that correlate with local infraslow electrical activity," *NeuroImage*, vol. 84, pp. 1018–31, 2014.

[95] Tzourio-Mazoyer, N., Landeau, B., Papathanassiou, D., and others, "Automated anatomical labeling of activations in spm using a macroscopic anatomical parcellation of the mni mri single-subject brain," *Magn Reson Med*, vol. 15, no. 1, pp. 273–89, 2002.

[96] Uddin, L., Kelly, A., Biswal, B., and others, "Network homogeneity reveals decreased integrity of default-mode network in adhd," *J Neurosci Methods*, vol. 169, no. 1, pp. 249–54, 2008.

[97] van den Heuvel, M. and Hulshoff Pol, H., "Exploring the brain network: a review on resting-state fmri functional connectivity," *Image and Vision Computing*, vol. 20, no. 8, pp. 519–34, 2010.

[98] van der Maaten, L., "Visualizing data using t-sne," *Journal of Machine Learning Research*, vol. 9, pp. 2579–2605, 2008.

[99] van der Maaten, L., "Learning a parametric embedding by preserving local structure," in *Proceedings of the Twelfth International Conference on Artificial Intelligence and Statistics*, vol. 5, pp. 384–91, AISTATS, 2009.

[100] Vassiliadis, S., Hakkennes, E., Wong, J., and Pechanek, G., "The sum-absolute-difference motion estimation accelerator," in *Proceedings of Euromicro Conference*, IEEE, 1998.

[101] Watson, C. and Paxinos, G., *The rat brain*. Elsevier, 2006.

[102] Williams, K., Peltier, S., LaConte, S., and Keilholz, S., "Mri evidence of resting state connectivity in rodent brain," in *Proc. Intl. Soc. Mag. Reson. Med.*, vol. 14, 2006.

[103] Wilson, R., Mayhew, S., Rollings, D., and others, "Influence of epoch length on measurement of dynamic functional connectivity in wakefulness and behavioural validation in sleep," *NeuroImage*, vol. 112, pp. 169–79, 2015.

[104] Xia, W., Wang, S., Sun, Z., and others, "Altered baseline brain activity in type 2 diabetes: a resting-state fmri study," *Psychoneuroendocrinology.*, vol. 38, no. 11, pp. 2493–501, 2013.

[105] Yin, Y., Li, L., Jin, C., and others, "Abnormal baseline brain activity in posttraumatic stress disorder: a resting-state functional magnetic resonance imaging study," *Neurosci Lett*, vol. 498, no. 3, pp. 185–9, 2011.

[106] Zalesky, A., Fornito, A., Cocchi, L., and others, "Time-resolved resting-state brain networks," *Proc Natl Acad Sci*, vol. 111, no. 28, pp. 10341–46, 2014.

[107] Zang, Y., He, Y., Zhu, C., and others, "Altered baseline brain activity in children with adhd revealed by resting-state functional mri," *Brain Dev.*, vol. 29, no. 2, pp. 83–91, 2007.

[108] Zhao, F., Zhao, T., Zhou, L., and others., "Bold study of stimulation-induced neural activity and resting-state connectivity in medetomidine-sedated rat," *NeuroImage*, vol. 39, pp. 248–60, 2008.